Quantum metrology with squeezed and entangled light for the detection of gravitational waves

Von der Fakultät für Mathematik und Physik
der Gottfried Wilhelm Leibniz Universität Hannover
zur Erlangung des Grades

Doktor der Naturwissenschaften
– Dr. rer. nat. –

genehmigte Dissertation
von

Dipl.-Phys. Sebastian Steinlechner

geboren am 11.08.1983 in Marburg/Lahn

2013

Referent:	Prof. Dr. Roman Schnabel
Korreferenten:	Prof. Dr. Karsten Danzmann
	Dr. Stefan Hild
Tag der Promotion:	16. Juli 2013

Abstract

Quantum metrology utilizes squeezed and entangled states of light to enhance the sensitivity of measurement devices. In interferometric gravitational wave detectors (GWDs), quantum noise is one of the main noise sources that limit the detection sensitivity. Emerging from proof-of-principle experiments, the GWD GEO 600 has been operating with squeezed light input since 2010 and a sensitivity increase by about 3 dB in the shot-noise limited regime has been achieved.

In this thesis, it is experimentally shown that the Sagnac interferometer topology can be enhanced with squeezed light. In a table-top, zero-area configuration, a nonclassical noise suppression by more than 8 dB is measured. The Sagnac interferometer topology has been shown to be a quantum back-action evading device, making it inherently less affected by radiation pressure noise. A zero-area configuration has to be adopted to cancel rotational noise coupling from the earth's rotation.

Furthermore, this thesis introduces and demonstrates the concept of quantum-dense metrology (QDM). QDM uses the two modes of a bipartite entangled state to perform all measurements relative to a reference beam. In a proof-of-principle experiment, QDM is used to distinguish between the science signal and a parasitic interference signal by simultaneously detecting both output quadratures of a table-top interferometer with sub-shot-noise accuracy. For the first time, it is shown how entanglement can be applied to improve the sensitivity of large-scale GWDs by providing a nonclassical veto-channel against stray-light induced events.

Finally, this thesis presents simulations of an entangled-light enhanced readout for GWDs with detuned signal recycling. The two output quadratures of such a detector provide an optimal signal response for different frequency regimes. With entangled light, both output quadratures can be simultaneously read out. A coherent combination then results in a sensitivity which is shown to be better than what is possible with a squeezed-light enhanced readout, when no filter cavity is used.

Within this thesis, novel applications of quantum metrology for GWDs were developed. The field of QDM was introduced, providing a new tool for quantum-enhanced measurements.

Keywords: Gravitational Wave Detection, Squeezed Light, Entanglement, Sagnac Interferometer, Quantum-Dense Metrology, Signal Recycling

Kurzfassung

In der Quantenmetrologie werden gequetschte und verschränkte Zustände des Lichts verwendet, um die Empfindlichkeit von Messinstrumenten zu verbessern. Quantenrauschen zählt zu den bedeutendsten Rauschquellen in interferometrischen Gravitationswellendetektoren (GWD). Zur Anwendung kommt Quantenmetrologie beim Detektor GEO 600, der seit 2010 mit gequetschtem Licht betrieben wird. Hierdurch konnte eine Empfindlichkeitssteigerung um etwa 3 dB im schrotrauschlimitierten Bereich erzielt werden.

In dieser Arbeit wird experimentell gezeigt, dass ein Sagnac-Interferometer mit gequetschtem Licht betrieben werden kann. In einem Beispielexperiment wird eine nichtklassische Rauschunterdrückung eines solchen Interferometers um mehr als 8 dB erzielt. Bereits früher wurde gezeigt, dass die Sagnac-Topologie praktisch frei von Quantenrückwirkungsrauschen ist. Um durch die Erdrotation verursachtes Rotationsrauschen zu vermeiden, ist dabei eine Konfiguration mit verschwindendem Flächeninhalt nötig.

Desweiteren wird in dieser Arbeit quantendichte Metrologie (QDM) als neues Konzept eingeführt und demonstriert. QDM verwendet die beiden Moden eines bipartiten verschränkten Zustandes, um alle Messungen relativ zu einem Referenzstrahl durchzuführen. Ein Beispielexperiment zeigt wie QDM benutzt werden kann, um zwischen dem Nutzsignal und parasitären Interferenzen in einem Interferometer zu unterscheiden, indem beide Ausgangsquadraturen mit einer Empfindlichkeit unterhalb des Schrotrauschens detektiert werden. Damit wird zum ersten Mal gezeigt, wie Verschränkung benutzt werden kann, um die Empfindlichkeit von GWD zu verbessern, indem ein nichtklassischer Vetokanal gegen streulichtinduzierte Signale bereitgestellt wird.

Außerdem wird in dieser Arbeit ein Ausleseverfahrens mit verschränktem Licht für GWD mit verstimmtem Signalrecycling simultiert. Die beiden Ausgangsquadraturen eines solchen Detektors haben ihre optimale Signalantwort in unterschiedlichen Frequenzbereichen. Mit Hilfe von verschränktem Licht können beide Quadraturen simultan detektiert werden. Hier wird gezeigt, dass eine kohärente Kombination dieser Quadraturen eine bessere Empfindlichkeit liefert, als es mit gequetschtem Licht möglich wäre, solange keine Filterresonatoren eingesetzt werden.

Im Rahmen dieser Arbeit wurden neue Quantenmetrologie-Anwendungen für GWD entwickelt. Mit der Einführung von QDM steht ein neues Hilfmittel für Quantenmessprozesse zur Verfügung.

Schlüsselbegriffe: Gravitationswellendetektion, gequetschtes Licht, Verschränkung, Sagnac-Interferometer, quantendichte Metrologie, Signalrecycling

Contents

1 Introduction **1**

2 Gaussian quantum states of light **7**
  2.1 Quantization of the electric field 7
  2.2 Squeezed states 9
  2.3 Gaussian states and the Wigner function 10
  2.4 State detection 12
  2.5 Entanglement 12
    2.5.1 Einstein-Podolsky-Rosen entanglement 12
    2.5.2 The EPR-Reid criterion 13
    2.5.3 Two-mode squeezed states 14
    2.5.4 Continuous-variable EPR steering 16
    2.5.5 Inseparable states and the Duan criterion 17
  2.6 Optical loss 18
  2.7 Quantum noise in interferometric gravitational wave detectors . . . 19
    2.7.1 The standard quantum limit 20
    2.7.2 Squeezed-light enhancement 22

3 Experimental foundations **29**
  3.1 Squeezed-light generation by parametric down-conversion 29
    3.1.1 Interaction in a non-linear crystal 29
    3.1.2 Phase matching 31
  3.2 State-of-the-art preparation of one- and two-mode squeezed light . . 33
    3.2.1 Laser preparation 33
    3.2.2 Second Harmonic Generation 35
    3.2.3 Squeezed light source 36
    3.2.4 Balanced homodyne detection 37
    3.2.5 Preparation of Einstein-Podolsky-Rosen entanglement 40

4 Squeezed-light enhanced zero-area Sagnac interferometer 47
4.1 The Sagnac topology for gravitational wave detection 47
4.1.1 Motivation 47
4.1.2 The Sagnac interferometer as a QND device 49
4.2 Demonstration of a quantum-enhanced Sagnac interferometer 50
4.3 Conclusion 54

5 Quantum-dense metrology 59
5.1 Introduction 59
5.2 Theoretical background 60
5.2.1 Discussion by Arthurs and Kelly 61
5.2.2 Quantum-dense readout 63
5.3 Experimental demonstration of quantum-dense metrology 64
5.3.1 Source of quadrature-entangled light 64
5.3.2 Interferometer with stray-light signal generation 66
5.3.3 Simultaneous homodyne detection scheme 67
5.4 Results 68
5.5 Discussion 70
5.6 Conclusion 71

6 Entangled-light enhanced detuned signal recycling 75
6.1 Motivation 75
6.2 Theoretical description 77
6.3 Simulation results 79

7 Summary and conclusion 85

A Appendix 87
A.1 Matrix formalism for the reflectivity of cavities and multi-layer stacks 87
A.2 Practical impedance-matching 90
A.3 Electronics 95
A.3.1 Mephisto temperature lock 95
A.3.2 OPA-lock photo-detector 95
A.3.3 AD9959 four-channel digital function generator 96
A.3.4 Small monitoring photo-detector 96
A.3.5 Homodyne detector 97
A.3.6 Servo 97
A.4 Software 112
A.4.1 TkSim 112
A.4.2 AD9959 113
A.4.3 lab 113

A.4.4 Entangled readout simulation 113

List of Figures

2.1 3D plot of the Wigner function $W(x)$ for a vacuum state and a squeezed vacuum state . . . 11
2.2 Entanglement at a 50:50 beam splitter . . . 14
2.3 Graphical representation of the continuous-variable EPR-steering task 16
2.4 Optical loss modeled by a beam splitter operation . . . 18
2.5 Effect of optical loss on squeezed states of light . . . 19
2.6 Quantum noise of a Michelson interferometer at different input laser powers . . . 21
2.7 Quantum noise of a Michelson interferometer with squeezed light input . . . 22
2.8 Sub-SQL sensitivity of a Michelson interferometer with squeezed light input . . . 23

3.1 Quasi phase matching in periodically poled non-linear crystals . . . 32
3.2 Schematic of a state-of-the-art experimental setup for the creation of one- and two-mode squeezed states . . . 34
3.3 Schematic of a hemilithic OPA used for squeezed light generation . 36
3.4 Balanced homodyne detection . . . 37
3.5 Homodyne visibility adjustment with an auxiliary mode cleaner . . 40
3.6 Preparation of two-mode squeezed states at a beam splitter . . . 41
3.7 Example measurement of continuous-variable entanglement . . . 41

4.1 A zero-area Sagnac interferometer configuration . . . 48
4.2 Comparison of the frequency response for a Michelson and a Sagnac interferometer . . . 49
4.3 Schematic of the quantum-enhanced Sagnac interferometer . . . 51
4.4 Results of the quantum-enhanced Sagnac interferometer . . . 52
4.5 Simulation of a quantum-noise enhanced, zero-area Sagnac interferometer . . . 53

5.1 Schematic showing the underlying principle of quantum-dense metrology . . . 61
5.2 Simultaneous readout of two orthogonal quadratures in an Arthurs-Kelly type setup . . . 61
5.3 Simultaneous, quantum-dense readout of two orthogonal quadratures 63
5.4 Single-sideband control scheme for the entanglement phase lock . . 65
5.5 Michelson interferometer for the demonstration of quantum-dense metrology . . . 66
5.6 Intensity and phase of the light in reflection of a strongly under-coupled cavity . . . 67
5.7 Schematic of balanced homodyne interferometer readout 68
5.8 Experimental demonstration of quantum-dense metrology 69

6.1 Simulation of a GEO600-like interferometer with detuned signal-recycling and 10dB squeezed light readout . . . 76
6.2 Block diagram representing the entangled readout of a detuned signal-recycled interferometer . . . 78
6.3 Squeezed and entangled quantum noise reflected at a detuned cavity 80
6.4 Simulation of an entangled-light enhanced readout of two orthogonal quadratures in a GEO 600-like interferometer with detuned signal recycling . . . 81

A.1 Reflection at a boundary between two media with different refractive indices . . . 87
A.2 Simulation of the wavelength-dependent reflectivity of a dichroic HR mirror coating for a design wavelength of 1064 nm at an angle of incidence of 45°. . . . 89
A.3 Smith chart showing the connection between a polar representation of the reflection coefficient Γ and the load impedance 91
A.4 Example setup for the measurement of the reflection coefficient . . . 92
A.5 Definition of the input- and output fields for a two-port device . . . 92
A.6 Smith chart showing effect of adding passive components to the load 93
A.7 Schematic for an impedance matching circuit in a local oscillator input section . . . 93
A.8 *Mephisto* laser temperature actuator for the MSQZ control beam lock 95
A.9 SqzLockPD v1.2, used for locking the control beam and pump phase of the squeezed light resonators . . . 96
A.10 TinyPD, a small DC monitoring photo detector 96
A.11 Homo V1.4, the circuit board for the balanced homodyne detectors . 97
A.12 Servo 4.04/4.05 circuit board preview, top layer 99
A.13 *Mephisto* laser temperature actuator, circuit schematic 100

A.14 SqzLockPD v1.2 schematic: resonant photo detection 101
A.15 SqzLockPD v1.2 schematic: demodulation path 102
A.16 SqzLockPD v1.2 schematic: local oscillator path with 90° power splitter 103
A.17 AD9959 4-channel frequency generator: circuit schematic of the USB interface 104
A.18 TinyPD v2.1 monitoring photo-detector: circuit schematics 105
A.19 HomoV1.4 balanced homodyne detector: detection stage 106
A.20 HomoV1.4 balanced homodyne detector: demodulation stage 107
A.21 Servo 4.04/4.05 schematic: transfer function shaping elements 108
A.22 Servo 4.04/4.05 schematic: ramp generator section 109
A.23 Servo 4.04/4.05 schematic: offset voltage generation 110
A.24 Servo 4.04/4.05 schematic: low frequency stage 111

Symbols and Abbreviations

Abbreviations

AOM	acousto-optic modulator
AR	anti reflective
BHD	balanced homodyne detector
DBS	dichroic beam splitter
DUT	device under test
EOAM	electro-optical amplitude modulator
EOM	electro-optic modulator
EPR	Einstein-Podolsky-Rosen (entanglement type)
GW	gravitational wave
HR	highly reflective
HSQZ	hemilithic squeezed-light source
HUP	Heisenberg's uncertainty principle
LO	local oscillator
LSD	linear noise spectral density
MC	mode-cleaning ring-cavity
MSQZ	monolithic squeezed-light source
NPRO	non-planar ring oscillator
NTC	negative temperature coefficient thermistor
OPA	optical parametric amplifier
PBS	polarizing beam splitter
PDC	parametric down-conversion
PDH	Pound-Drever-Hall locking scheme
PPKTP	periodically-poled potassium titanyl phosphate
PZT	piezo-electric transducer
QDM	quantum-dense metrology
QND	quantum-nondemolition device/measurement
SQL	standard quantum limit
SR	signal recycling
SSB	single sideband

TEC	thermo-electric cooler

Symbols

$[\hat{A}, \hat{B}]$	commutator between operators $\hat{A}$ and $\hat{B}$
$\langle \hat{O} \rangle$	expectation value of operator $\hat{O}$
$\mathcal{A}$	effective beam cross-section
$\hat{a}$	annihilation operator
$\hat{a}^\dagger$	creation operator
$\hat{a}_\pm$	annihilation operator at sideband frequency $\pm\Omega$
$\mathbf{BS}$	beam splitter transformation matrix
$\chi^{(i)}$	i-th order dielectric susceptibility
$\mathrm{CoV}(\hat{A}, \hat{B})$	covariance of operators $\hat{A}$ and $\hat{B}$
c	speed of light, $c = 299792458\,\mathrm{m/s}$
$\hat{D}(\alpha)$	coherent displacement operator
ε_0	dielectric permittivity
η	fractional loss parameter
$\hat{E}$	electric field operator
f	frequency (hertz)
$F(\Omega)$	frequency response
γ	covariance matrix
$\hbar$	reduced Planck's constant, $\hbar = 1.056 \times 10^{-34}\,\mathrm{m^2 kg/s}$
$\hat{H}$	Hamiltonian
h	gravitational wave strain
$h(f)$	linear strain sensitivity
κ	cavity decay rate
$\boldsymbol{k}$	wave vector
λ	optical wavelength
L	interferometer armlength
μ	reduced mass
$\boldsymbol{\mu}$	vector of mean values
n	index of refraction
Ω	sideband frequency (radians per second)
ω_0	optical frequency of the carrier field (radians per second)
ϕ	relative phase
P	laser power
$\mathbf{R}$	rotation transformation matrix
r	squeezing parameter
$\mathbf{S}(r)$	squeezing transformation matrix
$\hat{S}(r)$	squeezing operator
S_x	single sided power spectral density of observable $\hat{x}$
$S_x(\Omega)$	power spectral density of x

t	time
TEM_{xy}	transversal electro-magnetic mode
$\hat{U}(t)$	unitary time evolution operator
$\mathrm{Var}\big(\hat{O}\big)$	variance of operator $\hat{O}$
$W(\boldsymbol{x})$	Wigner function
$\hat{\boldsymbol{x}}$	vector of quadrature operators
x	position
X_1	amplitude quadrature operator
X_2	phase quadrature operator
ζ	detection angle

List of components

The following schematic drawings of components are used throughout this thesis. They have been taken from the component**library** version three by alexander franzen 2k+6.

Optical components

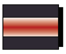	laser
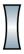	concave lens
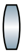	convex lens
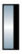	mirror
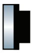	PZT-mounted mirror
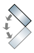	flip mirror
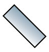	beam-splitter
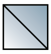	polarizing beam-splitter
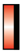	dichroic beam-splitter
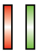	$\lambda/2$ wave-plates
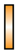	$\lambda/4$ wave-plate
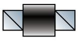	isolator
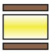	electro-optical modulator
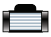	acousto-optical modulator
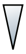	generic phase shifter
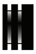	beam dump

Electronic components

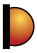	photo-detector, 1064 nm
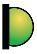	photo-detector, 532 nm
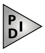	PID controller (servo)
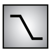	lowpass filter
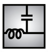	bias-tee
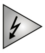	high-voltage amplifier
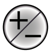	sum/difference junction
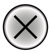	mixer
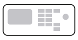	spectrum analyzer

▸ Chapter 1

Introduction

The first direct detection of gravitational waves will open up a new window to our universe. Predicted by Albert Einstein [Ein18] in the context of his General Theory of Relativity, these quadrupole waves distort the space-time itself. Gravitational radiation is emitted by any mass distribution which is accelerated in a non spheric-symmetrical way. However, it takes extremely massive objects to produce a measurable effect in the far field. The first evidence for such radiation was observed in the now-famous Hulse-Taylor binary pulsar [TW82]. As energy is transported off through gravitational waves, the system's orbital period decays in perfect agreement with General Relativity.

The nature of gravitational waves is quite different from that of electromagnetic waves as observed by optical and infrared telescopes, radio observatories and gamma-ray telescopes. This has often been likened to finally being able to *hear* the universe, when currently one can only *see* it [Hug03]. Gravitational radiation couples to matter quite differently than electromagnetic waves and thus will provide answers to a lot of open astronomical questions [ET] and might shed some light onto the mysterious subjects of dark energy and dark matter.

Gravitational waves exert tidal forces, stretching and squeezing the space-time as they travel through. Unfortunately, even the strongest astrophysical events create unbelievably small length changes $h = \delta L/L$ of less than 10^{-22} here on earth. Still, this effect can in principle be measured by very precisely monitoring the distance between free-falling test-masses with a laser interferometer [MW72].

A global network of interferometric gravitational wave detectors [LIGO; Virgo; GEO600] has been listening over the past years and is currently being upgraded to the second generation, increasing their sensitivity by about one order of magnitude [WAA+06; AVirgo; Har10; Som12]. This sensitivity increase goes along with a huge coordinated effort to identify, model and address the important noise sources of the detectors. Cutting edge research from many fields of physics comes together to improve seismic isolation suspensions, optical materials and their coatings, high-power ultra-stable lasers and to introduce new technologies such as signal-recycling and non-classical, squeezed light. It is complemented on the theory side by an always increasing understanding of the cosmic sources of gravitational waves. Sophisticated post-newtonian calculations and numerical simulations generate templates for the expected waveforms, which can then be extracted from the detector output stream with highly optimized data analysis techniques [SS09].

With the second generation coming online in 2014/15, the first direct detection of gravitational waves is within reach as soon as the design sensitivity has been achieved [Har10]. After that, the main focus will shift to gravitational wave astronomy, i.e. pushing the detectors' signal-to-noise ratio to a point where precise studies of the sources can be performed.

The light's quantum noise limits gravitational wave detectors over a wide frequency range. The investigation of quantum noise in high sensitivity, interferometric position measurements was actually triggered by gravitational wave detectors and the immense sensitivity requirements they need to achieve [BK96]. These investigations opened the field of quantum metrology and soon led to the discovery of the *standard quantum limit*, a direct result of the Heisenberg uncertainty relation and an effect of measurement back-action noise induced by the meter system. In a compelling argument [Cav80], C. Caves clarified the origin of radiation pressure noise in an interferometer. This led to the insight that squeezed states of light – which at that time had not been experimentally produced – can be injected into the dark port of gravitational wave detectors to reduce the quantum noise [Cav81]. The generation of squeezed light recently matured enough to be implemented in the gravitational wave detectors GEO 600 [AAA+11] and successfully tested in the LIGO H1 detector [LSC12]. In GEO 600, it has been shown that a stable operation with nonclassical light over many months is possible [GDD+13].

Instead of shaping the quantum-noise properties of the light itself, other approaches modify the interferometer topology or the detection process to evade quantum back-action noise [BV74; KLM+01]. The Sagnac interferometer topology, for example, has been shown to be a speed meter [Che03], i.e. instead of measuring the position of the test masses, it measures their speed. The speed of the test masses is a so-called quantum non-demolition (QND) observable, which means that measuring it has no influence on the measurement results at a later time. Because of this, the Sagnac interferometer is inherently less affected by back-action noise.

This thesis presents my work on several experiments at the frontier of quantum metrology for gravitational wave detection.

Outline of the thesis

First, the quantum-mechanical foundations of this thesis are reviewed. Beginning with the two-photon matrix formalism for the quantization of electro-magnetic fields, coherent and squeezed states of light are introduced. Entangled, two-mode squeezed states are constructed and a short introduction to entanglement criteria is given. The Chapter 2 closes with an overview of quantum noise in gravitational wave detectors.

Chapter 3 reviews the experimental techniques of state-of-the-art squeezing experiments, which form the basis for the experiments of this thesis. The main building blocks are described, such as second harmonic generation and squeezed light sources. In addition, an overview over current techniques for low-loss detection of squeezed and entangled states is given.

The zero-area Sagnac topology is a possible candidate for future gravitational wave detectors. In Chapter 4, such a topology is implemented in a small table-top experiment. The output from a monolithic squeezed light source is used to demonstrate a quantum-noise suppression by more than 8 dB in the shot-noise limited regime.

The new concept of *quantum-dense metrology* is introduced in Chapter 5. It uses entangled states to read out *two* orthogonal quadratures of an interferometer at the same time, with sub shot-noise sensitivity. In a proof-of-principle experiment, it is demonstrated how this readout scheme can be used to identify and possibly remove noise from scattered photons in gravitational wave detectors.

Chapter 6 applies entangled readout to gravitational wave detectors with detuned signal recycling. In a numerical simulation, it is shown how the combined readout of two orthogonal quadratures achieves a significantly better sensitivity than a signal-recycled interferometer with squeezed input.

Finally, the results and conclusions from my thesis are summarized in Chapter 7.

References

[AAA+11] J. Abadie, B. P. Abbott, R. Abbott, T. D. Abbott, M. Abernathy, C. Adams, R. Adhikari, C. Affeldt, B. Allen, G. S. Allen, et al. "A gravitational wave observatory operating beyond the quantum shot-noise limit". *Nature Physics* 7 (2011), 962–965. DOI: `10.1038/nphys2083`.

[AVirgo] The Virgo Collaboration. *Advanced Virgo Baseline Design*. Tech. rep. VIR-027A-09. 2009.

[BK96] V. B. Braginsky and F. Y. Khalili. "Quantum nondemolition measurements: the route from toys to tools". *Review of Modern Physics* 68 (1996), 1–11. DOI: `10.1103/RevModPhys.68.1`.

[BV74] V. Braginsky and Y. Vorontsov. "Quantum-mechanical restrictions in macroscopic measurements and modern experimental devices". *Uspekhi Fizicheskikh Nauk* 114 (1974), 41–53.

[Cav80] C. M. Caves. "Quantum-mechanical radiation-pressure fluctuations in an Interferometer". *Physical Review Letters* 45 (1980), 75–79. DOI: `10.1103/PhysRevLett.45.75`.

[Cav81] C. M. Caves. "Quantum-mechanical noise in an interferometer". *Physical Review D* 23 (1981), 1693. DOI: `10.1103/PhysRevD.23.1693`.

[Che03] Y. Chen. "Sagnac interferometer as a speed-meter-type, quantum-nondemolition gravitational-wave detector". *Physical Review D* 67 (2003), 122004. DOI: `10.1103/PhysRevD.67.122004`.

[Ein18] A. Einstein. "Über Gravitationswellen". *Sitzungsberichte der preußischen Akademie der Wissenschaften* (1918), 154–167.

[ET] ET Science Team. *Einstein gravitational wave Telescope conceptual design study*. Tech. rep. ET-0106C-10. 2011.

[GDD+13] H. Grote, K. Danzmann, K. L. Dooley, R. Schnabel, J. Slutsky, and H. Vahlbruch. "First Long-Term Application of Squeezed States of Light in a Gravitational-Wave Observatory". *Physical Review L* 110 (2013), 181101. DOI: `10.1103/PhysRevLett.110.181101`. arXiv: `1302.2188`.

[GEO600] *GEO600*. URL: `http://www.geo600.org/`.

[Har10] G. M. Harry. "Advanced LIGO: the next generation of gravitational wave detectors". *Classical and Quantum Gravity* 27 (2010), 084006. DOI: `10.1088/0264-9381/27/8/084006`.

[Hug03] S. A. Hughes. "Listening to the universe with gravitational-wave astronomy". *Annals of Physics* 303 (2003), 142–178. DOI: `10.1016/S0003-4916(02)00025-8`.

[KLM⁺01] H. J. Kimble, Y. Levin, A. B. Matsko, K. S. Thorne, and S. P. Vyatchanin. "Conversion of conventional gravitational-wave interferometers into quantum nondemolition interferometers by modifying their input and/or output optics". *Physical Review D* 65 (2001), 22002. DOI: `10.1103/PhysRevD.65.022002`.

[LIGO] *LIGO*. URL: `http://www.ligo.org`.

[LSC12] The LIGO Scientific Collaboration. "Enhancing the astrophysical reach of the LIGO gravitational wave detector by using squeezed states of light". LIGO-P1200041-v11. 2012.

[MW72] D. J. Muehlner and R. Weiss. "Gravitation Research". *RLE Progress Report* 105 (1972).

[Som12] K. Somiya. "Detector configuration of KAGRA – the Japanese cryogenic gravitational-wave detector". *Classical and Quantum Gravity* 29 (2012), 124007. DOI: `10.1088/0264-9381/29/12/124007`.

[SS09] B. Sathyaprakash and B. Schutz. "Physics, astrophysics and cosmology with gravitational waves". *Living Rev. Relativity* 12 (2009). DOI: `10.12942/lrr-2009-2`.

[TW82] J. H. Taylor and J. M. Weisberg. "A new test of general relativity - Gravitational radiation and the binary pulsar PSR 1913+16". *The Astrophysical Journal* 253 (1982), 908. DOI: `10.1086/159690`.

[Virgo] *VIRGO*. URL: `http://www.ego-gw.it`.

[WAA⁺06] B. Willke, P. Ajith, B. Allen, P. Aufmuth, C. Aulbert, S. Babak, R. Balasubramanian, B. W. Barr, S. Berukoff, A. Bunkowski, et al. "The GEO-HF project". *Classical and Quantum Gravity* 23 (2006), S207. DOI: `10.1088/0264-9381/23/8/S26`.

▸ Chapter 2

Gaussian quantum states of light

The main tool of continuous-variable quantum metrology are quantum states of light that can be described by Gaussian statistics. Prominent examples are the coherent states, which are produced by a laser resonator. In this chapter, the fundamental description of such states is reviewed, especially regarding their quantum-noise properties. Ultimately, the light fields will carry signals in the form of amplitude or phase modulations. C. Caves and B. Schumaker developed the quantum-optical theory of modulations [SC85; Cav85], whose main idea is summarized here. Afterwards, the concept of squeezing and entanglement is introduced, before a short overview on quantum noise in gravitational wave detectors is given.

▸ 2.1 *Quantization of the electric field*

Let us start with the field quantization of an electro-magnetic wave which is described by the operators $\hat{E}(\boldsymbol{r}, t)$ and $\hat{B}(\boldsymbol{r}, t)$. For our experiments, the magnetic field can be completely neglected and the focus lies on the properties of the electric field component. To save some notational burden, let us drop the explicit spatial dependence and restrict our treatment to a fixed point in space. Then, the electric field operator for a field with fundamental frequency ω_0 is given by [KLM+01]

$$\begin{aligned}\hat{E}(t) &= \hat{E}^{+}(t) + \hat{E}^{-}(t) \\ &= \sqrt{\frac{2\pi\hbar}{\mathcal{A}c}} \int_0^\infty \sqrt{\omega}\, \hat{a}_\omega\, \mathrm{e}^{-\mathrm{i}\omega t}\, \frac{\mathrm{d}\omega}{2\pi} + \text{h.c.}\,, \end{aligned} \tag{2.1}$$

where $\mathcal{A}$ is the effective cross sectional area of the beam, $\hat{a}_\omega$ is the annihilation operator, and h.c. indicates the hermitian conjugate. Following [KLM+01], all operators are given in the Heisenberg picture, i.e. evolving with time, but with the time dependence of the annihilation operator explicitly factored out as $\hat{a}\,\mathrm{e}^{-\mathrm{i}\omega t}$ like above. The annihilation operator obeys the commutation relations

$$[\hat{a}_\omega, \hat{a}_{\omega'}] = 0, \quad [\hat{a}_\omega, \hat{a}^\dagger_{\omega'}] = 2\pi\delta(\omega - \omega'), \tag{2.2}$$

where the superscript † indicates the hermitian conjugate and $\hat{a}^\dagger$ is also known as the creation operator.

As is well known, an amplitude or phase modulation can be conveniently described in the sideband picture. A modulation with frequency Ω, imprinted on a carrier field with frequency ω_0, is expressed by correlated excitations of the sideband fields at $\omega_0 \pm \Omega$ (and possibly higher integer multiples of Ω, depending on the modulation index). Let us thus introduce the operators

$$\hat{a}_+ = \hat{a}_{\omega_0+\Omega}\sqrt{\tfrac{\omega_0+\Omega}{\omega_0}}, \qquad \hat{a}_- = \hat{a}_{\omega_0-\Omega}\sqrt{\tfrac{\omega_0-\Omega}{\omega_0}} \tag{2.3}$$

which describe the annihilation of photons at the sideband frequencies $\pm\Omega$. The scaling factors are needed to adjust for the different energies of photons at the frequencies of ω_0 and $\omega_0 \pm \Omega$ [Cav85], however the values of these factors are usually close to unity, since $\omega_0 \approx 2\pi \times 10^{15}$ Hz, while Ω typically does not exceed the megahertz regime. Therefore, this factor is neglected in the following.

Let us now further introduce the two-photon operators [Cav85; SC85]

$$\hat{X}_1 = \hat{a}_+ + \hat{a}^\dagger_-, \qquad \hat{X}_2 = -\mathrm{i}(\hat{a}_+ - \hat{a}^\dagger_-), \tag{2.4}$$

which simultaneously create a photon at the lower sideband and annihilate a photon at the upper sideband. The only non-vanishing commutation relations for these operators read

$$[\hat{X}_1, \hat{X}^\dagger_{2'}] = [\hat{X}^\dagger_{1'}, \hat{X}_2] = 2\mathrm{i} \times 2\pi\delta(\Omega - \Omega'), \tag{2.5}$$

where the prime in the subscript is used to denote the frequency $\omega_0 \pm \Omega'$, as in $\hat{X}_{1'} \equiv \hat{a}_{\omega_0+\Omega'} + \hat{a}^\dagger_{\omega_0-\Omega'}$. With these new operators, the electric field (2.1) becomes

$$\hat{E}(t) = \hat{E}_1(t)\cos(\omega_0 t) + \hat{E}_2(t)\sin(\omega_0 t), \text{ where} \tag{2.6a}$$

$$\hat{E}_j(t) = \sqrt{\frac{2\pi\hbar\omega_0}{\mathcal{A}c}} \int_0^\infty \left(\hat{X}_j \mathrm{e}^{-\mathrm{i}\Omega t} + \hat{X}^\dagger_j \mathrm{e}^{+\mathrm{i}\Omega t}\right) \frac{\mathrm{d}\Omega}{2\pi}. \tag{2.6b}$$

$\hat{E}_1$ and $\hat{E}_2$ thus describe modulations of the light field in the two orthogonal quadratures sin and cos. They are therefore often called *quadrature phase operators*. The significance of this becomes more clear when we add a (classical) light field which serves as a phase reference, $E = E_{\mathrm{LO}}\cos(\omega_0 t)$. Such a field is also called a *local oscillator*. We then obtain

$$\hat{E}(t) = \big(E_{\mathrm{LO}} + \hat{E}_1(t)\big)\cos(\omega_0 t) + \hat{E}_2(t)\sin(\omega_0 t), \tag{2.7}$$

from which it becomes clear that $\hat{E}_1$ describes amplitude modulations, while $\hat{E}_2$ describes phase modulations. The fundamental operators creating these modulations are the Fourier components of $\hat{E}_j$, i.e. the two-photon operators $\hat{X}_1$ and $\hat{X}_2$ introduced above, which are thus known as the *quadrature operators*.

It is useful [SC85] to combine the quadrature operators into a vector,

$$\hat{\boldsymbol{x}} = \begin{pmatrix} \hat{X}_1 \\ \hat{X}_2 \end{pmatrix} . \tag{2.8}$$

Since most transformations needed to describe the inner workings of laser interferometers are linear or can at least be linearized, see e.g. [Har06], they are conveniently described as 2 × 2 matrices acting on the quadrature operator vectors. We will introduce two such transformations, squeezing and rotation, in the following section.

▸ 2.2 *Squeezed states*

The ground state of two-photon optics is the *vacuum state* defined by

$$\hat{a}_\pm |0\rangle = 0 . \tag{2.9}$$

Starting from this vacuum state, coherent excitations can be obtained by applying the *displacement operator* $\hat{D}_\pm(\alpha_\pm) = \exp(\alpha_\pm \hat{a}_\pm^\dagger - \alpha_\pm^* \hat{a}_\pm)$, $\alpha_\pm \in \mathbb{C}$. For $\Omega = 0$, we obtain a single-mode, single-frequency excitation at the carrier frequency ω_0,

$$|\alpha\rangle = \hat{D}(\alpha)|0\rangle . \tag{2.10}$$

Such a state is known as a coherent state [Gla63]. The coherent displacement α is closely connected to the expectation values of the quadrature phase operators,

$$\langle \hat{X}_1 \rangle\Big|_\alpha = 2\,\mathrm{Re}(\alpha) , \tag{2.11}$$

$$\langle \hat{X}_2 \rangle\Big|_\alpha = 2\,\mathrm{Im}(\alpha) , \tag{2.12}$$

or equivalently, $\alpha = \frac{1}{2}\big(\langle \hat{X}_1 \rangle + \mathrm{i}\langle \hat{X}_2 \rangle\big)$. Coherent excitations of sideband modulations can be obtained by a combination of displacement operators at frequencies ±Ω,

$$|\alpha_+, \alpha_-\rangle = \hat{D}_+(\alpha_+)\hat{D}_-(\alpha_-)|0\rangle . \tag{2.13}$$

The coherent states are eigenstates of the annihilation operators $\hat{a}_\pm$ with eigenvalues $\alpha_\pm$. They, as well as the vacuum state, have an equally distributed uncertainty in both quadratures,

$$\mathrm{Var}\big(\hat{X}_1\big)\Big|_0 = \mathrm{Var}\big(\hat{X}_2\big)\Big|_0 = 1 , \tag{2.14}$$

$$\mathrm{Var}\big(\hat{X}_1\big)\Big|_\alpha = \mathrm{Var}\big(\hat{X}_2\big)\Big|_\alpha = 1 . \tag{2.15}$$

Here, $\mathrm{Var}(\hat{O}) = \langle \hat{O}^2 \rangle - \langle \hat{O} \rangle^2$ is the variance. Both states exactly saturate the minimum uncertainty allowed by the commutation relation (2.5),

$$\mathrm{Var}(\hat{X}_1)\big|_{0,\alpha} = \mathrm{Var}(\hat{X}_2)\big|_{0,\alpha} \geq \frac{1}{2}|\langle[\hat{X}_1, \hat{X}_2]\rangle| = 1\,. \tag{2.16}$$

The coherent states (2.13) do not show nonclassical correlations between the modulation sidebands, since they are equal to two independent coherent excitations of the sidebands at $\omega_0 \pm \Omega$. Squeezed states of light however are produced through a simultaneous, correlated excitation process described by

$$\hat{S}(r) = \exp\big(r(\hat{a}_+\hat{a}_- - \hat{a}_+^\dagger \hat{a}_-^\dagger)\big)\,. \tag{2.17}$$

It can be shown [SC85] that this squeezing operator transforms a quadrature vector $\hat{\boldsymbol{x}}$ like

$$\hat{S}(r)\hat{\boldsymbol{x}}\hat{S}^\dagger(r) = \mathbf{S}(r)\hat{\boldsymbol{x}}\,, \tag{2.18}$$

where $\mathbf{S}(r)$ is given by

$$\mathbf{S}(r) = \begin{pmatrix} \mathrm{e}^{-r} & 0 \\ 0 & \mathrm{e}^{+r} \end{pmatrix}\,. \tag{2.19}$$

Thus, the squeezing operator *squeezes* the uncertainty in one quadrature, while the orthogonal quadrature is simultaneously enlarged, keeping the uncertainty relation constant. We will accompany this with a graphical representation in the next section.

By implementing a quadrature rotation $\mathbf{R}(\theta)$, the squeezing transformation can be applied to any linear combination of the amplitude and phase quadratures,

$$\mathbf{S}(r,\theta)\hat{\boldsymbol{x}} = \mathbf{R}(-\theta)\mathbf{S}(r)\,\mathbf{R}(\theta)\hat{\boldsymbol{x}}\,. \tag{2.20}$$

Here we used the obvious identity $\mathbf{R}^\dagger(\theta) = \mathbf{R}(-\theta)$ and

$$\mathbf{R}(\theta) = \begin{pmatrix} \cos\theta & \sin\theta \\ -\sin\theta & \cos\theta \end{pmatrix}\,. \tag{2.21}$$

▸ 2.3 *Gaussian states and the Wigner function*

An important class of quantum-optical states are the *Gaussian* states, whose phase-space distribution can be described by Gaussian statistics. Thus the first and second

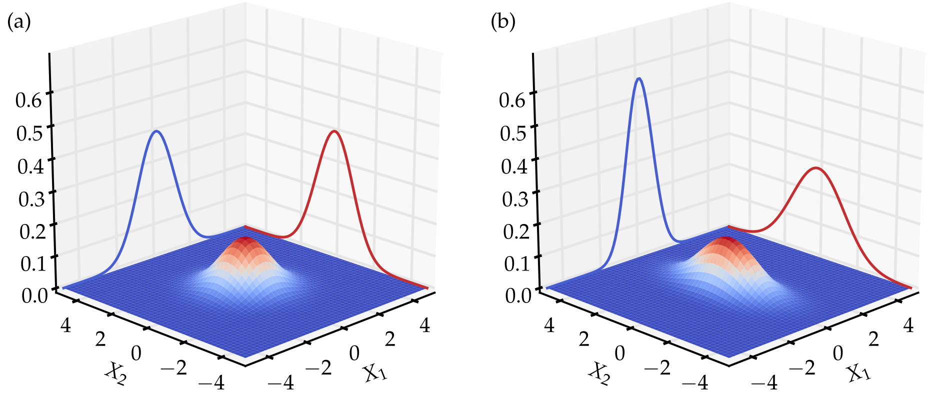

Figure 2.1: 3D plot of the Wigner function $W(x)$ for (a) a vacuum state and (b) a squeezed vacuum state with $r = 0.345$, corresponding to about 3 dB squeezing. Also shown are the marginal distributions for $\hat{X}_1$ (blue) and $\hat{X}_2$ (red).

order statistical moments, the mean value $\boldsymbol{\mu}$ and the covariance matrix γ, are sufficient to completely characterize such states. They are given by

$$\mu_i = \langle \hat{X}_i \rangle \,, \tag{2.22}$$

$$\gamma_{ij} = \mathrm{CoV}\big(\hat{X}_i, \hat{X}_j\big) \,, \tag{2.23}$$

where $\mathrm{CoV}\big(\hat{O}_1, \hat{O}_2\big) = \frac{1}{2}\langle \hat{O}_1\hat{O}_2 + \hat{O}_2\hat{O}_1\rangle - \langle \hat{O}_1\rangle\langle \hat{O}_2\rangle$ is the covariance, and, especially, $\mathrm{CoV}\big(\hat{O}, \hat{O}\big) = \mathrm{Var}\big(\hat{O}\big)$. These definitions also apply to the case of multiple field modes, where each mode is described by its own quadrature operators. Again combining them into a single quadrature operator vector $\hat{\boldsymbol{x}}$ results in a $2N$-dimensional phase space for the N modes.

An important representation of quantum states is the *Wigner function*, which for the case of Gaussian states is given by [GK05; DiG10]

$$W(\boldsymbol{x}) = \frac{1}{(2\pi)^{N/2}\sqrt{\det\gamma}} \exp\big(-\tfrac{1}{2}(\boldsymbol{x} - \boldsymbol{\mu})^T \gamma^{-1} (\boldsymbol{x} - \boldsymbol{\mu})\big) \,. \tag{2.24}$$

Its marginal distributions directly correspond to the probability distributions for the respective quadrature. Despite this, the Wigner function itself is only a quasi-probability distribution, since it can assume negative values for certain kinds of strongly non-classical states, e.g. photon-number (Fock) states.

Coherent states belong to the class of Gaussian states, as do squeezed states and of course the vacuum state. In Fig. 2.1, a 3D plot of the Wigner function for the vacuum state and a squeezed vacuum state is depicted, clearly showing why a squeezed state actually goes by that name.

▸ 2.4 *State detection*

In a typical quantum-optics experiment, one subjects an input state to a combination of various transformations and then detects the resulting quantum fluctuations of the output state with a photo detector. The balanced homodyne detector is ubiquitous in continuous-variable experiments such as in this thesis. It can detect an arbitrary combination of the two quadrature phases of a single mode of light. The output is a photo current $\hat{\imath}_\theta$ which scales linearly with the detected quadrature,

$$\hat{\imath}_\theta \propto \hat{X}_\theta = \hat{X}_1 \cos\theta + \hat{X}_2 \sin\theta \,. \tag{2.25}$$

In our experiments, the current gets converted into a voltage and its variance is displayed with a spectrum analyzer.

The quantum-optical modulation formalism reviewed above allows for a very nice short-hand for calculating the variance of any detected output quadrature, as long as the transformation matrix $\mathbf{C}$ operating on the initial vacuum state $\hat{v}$ is known. In that case [HCC⁺03],

$$\mathrm{Var}\big(\hat{\imath}\big) \propto \langle \cos(\theta), \sin(\theta) | \mathbf{C}\mathbf{C}^T | \cos(\theta), \sin(\theta) \rangle \,. \tag{2.26}$$

For complex transformation matrices, the product $\mathbf{C}\mathbf{C}^T$ has to be replaced by its symmetrized version $\frac{1}{2}\big(\mathbf{C}\mathbf{C}^\dagger + \mathbf{C}^*\mathbf{C}^T\big)$. This product is actually identical to the covariance matrix γ defined in (2.23). Since there are no quantum-mechanical operators involved in this way of calculating the output variance, it allows for a convenient use in computer programs, e.g. MATLAB code.

▸ 2.5 *Entanglement*

▸ 2.5.1 *Einstein-Podolsky-Rosen entanglement*

Entanglement is probably *the* main peculiarity of quantum mechanics. Famously, the 1935 article by A. Einstein, B. Podolsky and N. Rosen (EPR) [EPR35] describes how entanglement leads to a seemingly paradox situation connected to the Heisenberg uncertainty relation. Since position and momentum are non-commuting operators, EPR concluded that only one of these operators can correspond to a physical reality at any time. However, it turns out that by a measurement on a second particle – which is entangled with the first – one can predict either the position or the momentum of the first particle, without any way of interacting with it. Thus it seems that both operators must have had a physical reality, contradicting the initial assumption. While EPR concluded that quantum mechanics does not deliver a complete description of physical reality, they actually gave a hint at the modern interpretation of the paradox: their requirement of physical reality was too strong, since "two or more physical quantities can be regarded as simultaneous elements of reality *only when they can be simultaneously measured or predicted*" [EPR35].

▸ 2.5.2 *The EPR-Reid criterion*

In 1989, M. Reid rephrased the EPR paradox in the following way [Rei89]. Let us imagine two particles A and B. Since $[\hat{q}_A, \hat{p}_A] = [\hat{q}_B, \hat{p}_B] \neq 0$, these particles cannot simultaneously have a well defined position and momentum. Especially, we have $\mathrm{Var}(\hat{q}_A) \times \mathrm{Var}(\hat{p}_A) \geq 1$ – and correspondingly for $\hat{q}_B$ and $\hat{p}_B$ – for suitably selected scaling of the operators. However, by measuring the distance between the two particles, we can make an *estimate* of $\hat{q}_A$, which we call $\tilde{q}_A$, from a measurement of $\hat{q}_B$,

$$\tilde{q}_A = g_q \hat{q}_B\,. \tag{2.27}$$

The real-valued scaling parameter g_q is introduced here to allow for an optimization of the estimate. Now we can calculate the *inferred* variance, a measure of the quality of the estimation, by looking at the deviation between the estimated value and the true value,

$$\begin{aligned}\mathrm{Var}_{\mathrm{inf}}(\hat{q}_A) &= \langle (\hat{q}_A - \tilde{q}_A)^2 \rangle \\ &= \langle (\hat{q}_A - g_q \hat{q}_B)^2 \rangle\,. \end{aligned} \tag{2.28}$$

The same estimate can be done for $\hat{p}_A$ by a measurement of the sum of the particle momenta. This leads us to the final inequality that manifests the EPR paradox. Since our estimates of $\hat{q}_A$ and $\hat{p}_A$ should never be better than the original values, their uncertainty relation should still hold,

$$\mathrm{Var}_{\mathrm{inf}}(\hat{q}_A) \times \mathrm{Var}_{\mathrm{inf}}(\hat{p}_A) = \mathrm{Var}(\hat{q}_A - g_q \hat{q}_B) \times \mathrm{Var}(\hat{p}_A - g_p \hat{p}_B) \geq 1\,. \tag{2.29}$$

As we will see below, this so-called EPR-Reid inequality can be violated. Of course, since $[\hat{q}_A - \hat{q}_B, \hat{p}_A + \hat{p}_B] = 0$ this should not come as a surprise; the EPR paradox simply corresponds to the fact that in quantum mechanics, one can measure distances between two particles even when the individual positions and momenta of these particles are not defined.

The optimization parameters g_q and g_p need to be determined from measurement data. Fortunately, for bipartite Gaussian states, one can find an explicit formula for the optimal scaling factors by taking the partial derivative and setting it equal to zero [BL05],

$$0 \overset{!}{=} \frac{\partial}{\partial g_q} \mathrm{Var}_{\mathrm{inf}}(\hat{q}) \tag{2.30}$$

$$= -2\,\mathrm{CoV}(\hat{q}_A, \hat{q}_B) + 2 g_q\, \mathrm{Var}(\hat{q}_B)\,. \tag{2.31}$$

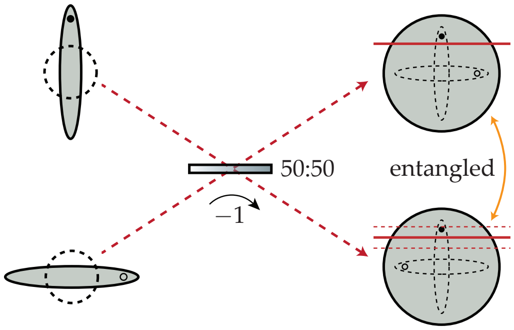

Figure 2.2: Phase-space uncertainties of two orthogonally squeezed beams which are overlapped at a 50:50 beam splitter. While the resulting modes individually resemble a noisy thermal state, the correlations between the two modes are given by the minor axes of the original squeezing ellipses and thus beat the vacuum uncertainty.

After a corresponding calculation for g_p, one obtains the optimum values

$$g_q = \frac{\mathrm{CoV}(\hat{q}_A, \hat{q}_B)}{\mathrm{Var}(\hat{q}_B)}, \qquad g_p = \frac{\mathrm{CoV}(\hat{p}_A, \hat{p}_B)}{\mathrm{Var}(\hat{p}_B)}. \tag{2.32}$$

Reinserting these values into the EPR-Reid inequality leads to

$$\left(\mathrm{Var}(\hat{q}_A) - \frac{\mathrm{CoV}(\hat{q}_A, \hat{q}_B)^2}{\mathrm{Var}(\hat{q}_B)}\right) \times \left(\mathrm{Var}(\hat{p}_A) - \frac{\mathrm{CoV}(\hat{p}_A, \hat{p}_B)^2}{\mathrm{Var}(\hat{p}_B)}\right) \geq 1. \tag{2.33}$$

This equation now only depends on entries of the 4×4 covariance matrix γ, defined in Eq. (2.23), which completely characterizes the bipartite Gaussian state.

▸ 2.5.3 *Two-mode squeezed states*

As was first experimentally shown by Z. Ou *et al.* in 1992 [OPK+92], the amplitude and phase quadratures of two light beams can be used to recreate the EPR paradox. To see this, let us start with two initially independent beams, described by the combined quadrature vector $\hat{x} = (\hat{X}_1^A, \hat{X}_2^A, \hat{X}_1^B, \hat{X}_2^B)$. The beams are then squeezed in orthogonal directions with squeezing parameters r and q, respectively, such that we end up with one amplitude and one phase quadrature squeezed beam. Overlapping these beams on a 50 : 50 beam splitter (cf. Fig. 2.2) creates entanglement between the two output modes [FSB+98]: a measurement result at the first mode allows to predict the outcome for a measurement of the same quadrature at the second mode. The uncertainty in this prediction is given by the squeezed variance of the original squeezed beams. Therefore, the prediction is not limited by the vacuum uncertainty, thus indicating non-classical, entangled correlations.

The interaction at the beam splitter is described by the transformation

$$\mathbf{BS} = \frac{1}{\sqrt{2}} \begin{pmatrix} 1 & 0 & 1 & 0 \\ 0 & 1 & 0 & 1 \\ 1 & 0 & -1 & 0 \\ 0 & 1 & 0 & -1 \end{pmatrix}, \tag{2.34}$$

which results in the output state

$$\begin{aligned} \hat{\boldsymbol{y}} &= \mathbf{BS}\big(\mathbf{S}(+r) \oplus \mathbf{S}(-q)\big)\hat{\boldsymbol{x}} \\ &= \mathbf{T}\hat{\boldsymbol{x}}\,. \end{aligned} \tag{2.35}$$

The complete transformation matrix $\mathbf{T}$ is then given by

$$\mathbf{T} = \frac{1}{\sqrt{2}} \begin{pmatrix} \mathrm{e}^{+r} & 0 & \mathrm{e}^{-q} & 0 \\ 0 & \mathrm{e}^{-r} & 0 & \mathrm{e}^{+q} \\ \mathrm{e}^{+r} & 0 & -\mathrm{e}^{-q} & 0 \\ 0 & \mathrm{e}^{-r} & 0 & -\mathrm{e}^{+q} \end{pmatrix}. \tag{2.36}$$

Looked at individually, each of the two output modes $\hat{\boldsymbol{y}}^A$, $\hat{\boldsymbol{y}}^B$ is now in a large, noisy thermal state, e.g.

$$\mathrm{Var}\big(\hat{Y}_1^A\big) = \langle 1,0,0,0|\mathbf{T}\mathbf{T}^T|1,0,0,0\rangle = \frac{\mathrm{e}^{-2q} + \mathrm{e}^{+2r}}{2} \tag{2.37}$$

$$\mathrm{Var}\big(\hat{Y}_2^A\big) = \langle 0,1,0,0|\mathbf{T}\mathbf{T}^T|0,1,0,0\rangle = \frac{\mathrm{e}^{+2q} + \mathrm{e}^{-2r}}{2}, \tag{2.38}$$

and similarly for $\hat{\boldsymbol{y}}^B$. However, the difference $\hat{Y}_1^- = \hat{Y}_1^A - \hat{Y}_1^B$ of the amplitude quadratures and the sum $\hat{Y}_2^+ = \hat{Y}_2^A + \hat{Y}_2^B$ of the phase quadratures show the original squeezing variances (cf. Fig. 2.2),

$$\mathrm{Var}\big(\hat{Y}_1^-\big) = \frac{1}{\sqrt{2}}\langle 1,0,-1,0|\mathbf{T}\mathbf{T}^T|1,0,-1,0\rangle = \mathrm{e}^{-2q} \tag{2.39}$$

$$\mathrm{Var}\big(\hat{Y}_2^+\big) = \frac{1}{\sqrt{2}}\langle 0,1,0,1|\mathbf{T}\mathbf{T}^T|0,1,0,1\rangle = \mathrm{e}^{-2r}\,. \tag{2.40}$$

Thus we have, for this system, the inequality (setting $g_q = g_p = 1$)

$$\mathrm{Var}_{\mathrm{inf}}\big(\hat{Y}_1\big) \times \mathrm{Var}_{\mathrm{inf}}\big(\hat{Y}_2\big) = \mathrm{Var}\big(\hat{Y}_1^-\big) \times \mathrm{Var}\big(\hat{Y}_2^+\big) = \mathrm{e}^{-2r}\mathrm{e}^{-2q} < 1\,, \tag{2.41}$$

which clearly violates the EPR-Reid inequality (2.29) for positive squeezing parameters r and q.

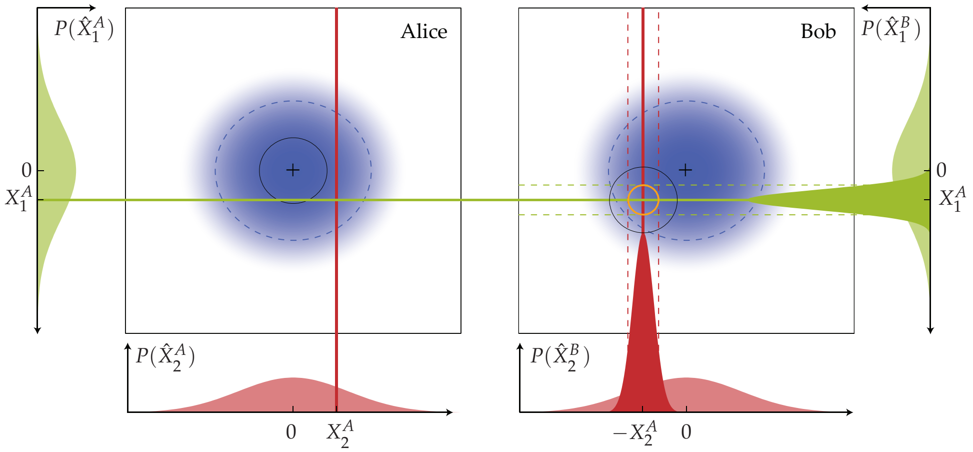

Figure 2.3: Graphical representation of the continuous-variable EPR-steering task. Locally, Alice and Bob each see a noisy thermal state, indicated by the violet disks and the broad projections onto the $\hat{X}_1$ and $\hat{X}_2$ axes (light blue and light red). For each measurement result X_1^A at Alice's state, the corresponding result at Bob's side lies within X_1^A with an uncertainty as given by the narrow blue distribution. For a measurement of $\hat{X}_2$, the narrow red distribution results. Put together, Alice can pinpoint Bob's measurement results with a precision as given by the orange circle. This circle is much smaller than the vacuum uncertainty, solid black circle, being the limit in the EPR-Reid criterion. (Figure adapted from [SBE⁺13].)

▸ 2.5.4 *Continuous-variable EPR steering*

The term *steering* has been coined by E. Schrödinger in his reply [Sch35] to the EPR thought experiment. In a modern formulation, it describes the following quantum-informational task [WJD07]. A bipartite state is shared between two parties. As it is common in quantum information science, we assign the archetypal characters *Alice* and *Bob* to the two parties, abbreviated to A and B in the indices of observables and measurement outcomes. Bob doubts that their state is entangled, but Alice claims that she can prove it to him. She can do this in the following way. Alice and Bob perform a series of simultaneous measurements on their local state, without revealing the measurement results. Then, Bob announces which of the two quadratures he measured for each of his results. For those measurements where Alice by chance measured the same quadrature, she then predicts his results from her data. Bob will be convinced that they indeed shared an entangled state when her predictions are more accurate than what would have been possible with any minimum uncertainty state. He gets the impression that Alice somehow *steered* his mode in the phase-space, such that her predictions always came out better than expected for an isolated, local state. Of course, other than the term *steering* might suggest, no actual information is exchanged during the measurement; only when Alice and Bob compare their results via a classical channel, the discrepancy with a local description becomes clear.

As it turns out [CJW⁺09], the demonstration of the EPR steering task is exactly equal to a manifestation of the EPR paradox as given by the EPR-Reid inequality (2.29). This insight has given new attention to the scaling parameters g_q and g_p, since they make the problem directional: For the case where Alice steers Bob, Alice scales her measurement results such that they most closely resemble Bob's results, while Bob scales his results when he tries to steer Alice. Asymmetry between the two states can lead to the interesting situation where Alice is able to steer Bob, but not vice versa. This was first experimentally demonstrated in our group by introducing asymmetric optical loss in the two entangled modes [HES⁺12].

Fig. 2.3 gives a graphical representation of the EPR-Reid inequality and the associated steering task. Alice and Bob share a bipartite state with local probability distributions given by $P(\hat{X}_1^{A,B})$ and $P(\hat{X}_2^{A,B})$. From a measurement outcome X_1^A at Alice's state, she can make a prediction about the outcome on Bob's side with an uncertainty as indicated by the narrow blue distribution and the dashed horizontal lines. Similarly, she can predict Bob's outcome for a measurement of X_2^A (in this case, the probability distribution for Bob's result will be centered around $-X_2^A$, due to the sign change at the beam splitter). Alice's prediction uncertainties, when combined together, lead to the orange circle, which depicts her ability to pinpoint a measurement result in Bob's phase space. When this uncertainty circle has an area that is less than the limit of the Heisenberg uncertainty (2.16), the EPR-Reid inequality (2.29) is violated and, equivalently, Bob will be convinced that they indeed shared an entangled state.

It should be noted that the class of steering states is only a subclass of entangled states, i.e. it is indeed possible for Alice and Bob to share an entangled state, where neither Alice nor Bob can convince the respective other of that situation.

▸ 2.5.5 *Inseparable states and the Duan criterion*

For completeness, let us introduce the most general class of entangled states, the inseparable states. A bipartite state $|\Psi\rangle$ is called inseparable when it cannot be written as a product state,

$$|\Psi\rangle \neq |\Psi^A\rangle \otimes |\Psi^B\rangle\,, \tag{2.42}$$

for any physical states $|\Psi^A\rangle$ and $|\Psi^B\rangle$. The Duan criterion [DGC⁺00] can be very conveniently applied to check a bipartite, continuous-variable state for inseparability.

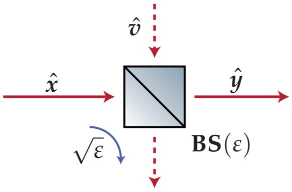

$$\hat{y} = \begin{pmatrix} \sqrt{1-\varepsilon} & 0 & \sqrt{\varepsilon} & 0 \\ 0 & \sqrt{1-\varepsilon} & 0 & \sqrt{\varepsilon} \\ \sqrt{1-\varepsilon} & 0 & -\sqrt{\varepsilon} & 0 \\ 0 & \sqrt{1-\varepsilon} & 0 & -\sqrt{\varepsilon} \end{pmatrix} (\hat{x} \otimes \hat{v})$$

Figure 2.4: Optical loss ε modeled by a beam splitter operation between the (non-classical) state $\hat{x}$ and an introduced vacuum mode $\hat{v}$.

It assumes the form of the following inequality,

$$\mathrm{Var}\big(\hat{X}_1^A - \hat{X}_1^B\big) + \mathrm{Var}\big(\hat{X}_2^A + \hat{X}_2^B\big) \geq 4\,. \tag{2.43}$$

Any state which violates this inequality is inseparable. Especially, it is easy to see that any state violating the EPR-Reid inequality (2.29) also violates the Duan inequality (setting $g_q = 1$, $g_p = -1$). Thus, every steerable state is necessarily also inseparable, while the converse is generally not true. As another example, a bipartite vacuum state can of course be written as a product of two single-mode vacuum states, and indeed (2.43) then simply decomposes into the individual variances, delivering $\big(\mathrm{Var}(\hat{X}_1^A) + \mathrm{Var}(\hat{X}_1^B)\big) + \big(\mathrm{Var}(\hat{X}_2^A) + \mathrm{Var}(\hat{X}_2^B)\big) = (1+1) + (1+1) = 4$.

▸ 2.6 *Optical loss*

As can be seen from both the Duan criterion (2.43) and the EPR-Reid criterion (2.29), the non-classical properties of entanglement (and squeezing, since it is essentially a form of sideband-sideband entanglement) vanish when the state approaches a vacuum state. Thus, non-classical states have to be protected from the deteriorating effects of additional vacuum state noise contributions. Such vacuum noise couples in due to imperfect overlap between two modes, e.g. for a non-optimal fringe contrast at a beam splitter, or due to an imperfect detection efficiency at the photo detectors. Optical loss can be modeled as a beam splitter operation as in Fig. 2.4, throwing away the fraction $\sqrt{\varepsilon}$ of a state and replacing it by a vacuum state which enters through the other input port.

For a squeezed input state, the resulting output noise variance is shown in Fig. 2.5 as a function of additional optical loss. The anti-squeezed quadrature, shown in blue, is much less affected by the loss than the squeezed quadrature, red, since its variance is so much larger than the vacuum uncertainty. For the detection of a 10 dB squeezed state of light, less than 10% total loss can be tolerated, independent of the initial squeezing value (shaded gray area). This underlines that low-loss experimental techniques are crucial to obtain high squeezing values and the reduction of optical

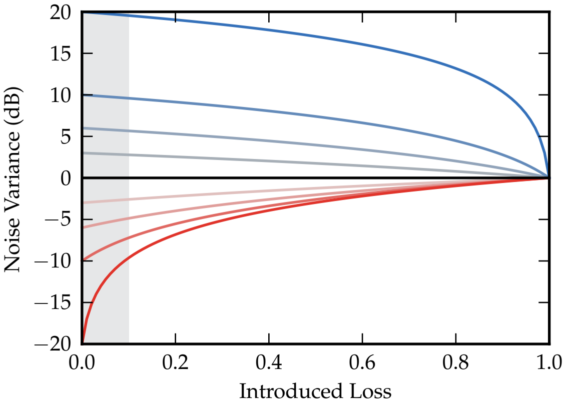

Figure 2.5: Effect of optical loss on squeezed states of light with an initial squeezed variance of 3 dB, 6 dB, 10 dB and 20 dB. The resulting noise variance of the squeezed quadrature is shown in reds, while the anti-squeezed quadrature is shown in blues. Less than 10% loss (shaded gray area) are needed to detect a 10 dB non-classical noise reduction. The anti-squeezed quadrature is much less affected.

loss is a key design element of any device which is to employ non-classical states of light. The ratio of the squeezed variance to anti-squeezed variance is usually used to determine the optical loss in a given setup, due to its characteristic dependency on introduced vacuum noise.

▸ 2.7 *Quantum noise in interferometric gravitational wave detectors*

The high sensitivity of interferometric gravitational wave detectors invariably means that the detection process is limited by quantum-mechanical noise sources. In a simple Michelson interferometer, i.e. just the beam splitter and two end mirrors, the quantum noise can be attributed to two different processes: a contribution from *photon shot noise*, which is white in frequency space, and a contribution from *radiation pressure noise*, which quickly falls off towards higher frequencies. C. Caves showed that both noise processes can be attributed to the two quadratures of the vacuum field which enters the interferometer dark (output) port [Cav80]. Since the quantum noise of the two quadratures is uncorrelated, shot noise and radiation pressure noise can be treated separately.

Fluctuations of the detected output power produce a signal which is indistinguishable from a differential arm length change. Thus, the laser shot noise can be translated into an equivalent displacement noise of the test masses. It is given by the (single sided) power spectral density [Sch10]

$$S_x^{\mathrm{SN}} = \frac{c^2\hbar}{2\omega_0 P}. \tag{2.44}$$

The radiation pressure force exerted on the interferometer end mirrors by the reflected light field is given by $F = 2P_{\mathrm{arm}}/c$, where $P_{\mathrm{arm}} = P/2$ is the light power inside one interferometer arm. The power fluctuations of a coherent light field are given by $S_P = 2\hbar\omega_0 P$. Thus, the spectral density of the fluctuating forces reads [Sch10]

$$S_F = 2\frac{\hbar\omega_0 P}{c^2}\,. \tag{2.45}$$

To obtain an equivalent displacement noise of the test masses, it has to be multiplied by the transfer function which translates a periodic force acting on the test mass into an actual microscopic displacement. Far above the suspension resonance frequency, the interferometer end mirrors act as free falling test masses. In this case, the transfer function is given by $(\mu\Omega^2)^{-1}$, where μ is the reduced mass and Ω is the excitation frequency. Thus we obtain the radiation pressure noise [Sch10]

$$S_x^{\mathrm{RPN}}(\Omega) = \frac{1}{\mu^2\Omega^4} S_F = \frac{8\hbar\omega_0 P}{c^2 m^2 \Omega^4}\,. \tag{2.46}$$

In the last step, $\mu = m/2$ was used since the radiation pressure noise acts on the combined system of two interferometer end mirrors with mass m each.

Often, the equivalent noise for a measurement of a gravitational wave strain $h = \Delta x/L$ is given, where L is the length of the interferometer arms. In this normalization, the quantum noise contributions read

$$h^{\mathrm{SN}}(\Omega) = \frac{1}{L}\sqrt{S_x^{\mathrm{SN}}} = \frac{c}{L}\sqrt{\frac{\hbar}{2\omega_0 P}}\,, \tag{2.47}$$

$$h^{\mathrm{RPN}}(\Omega) = \frac{1}{L}\sqrt{S_x^{\mathrm{RPN}}} = \frac{1}{mcL\Omega^2}\sqrt{8\hbar\omega_0 P}\,. \tag{2.48}$$

▸ 2.7.1 *The standard quantum limit*

The standard quantum limit (SQL) comes from a balance between two fundamental quantum noise sources, shot noise and radiation pressure noise. While the output signal is proportional to the available laser power P, its shot noise scales with the square-root of the power P. Thus, an increase of the laser power leads to an increase in the relative sensitivity by $\sqrt{P}$ in the shot-noise limited region. At the same time, the photons in the interferometer exert increasing random radiation pressure forces onto the test-masses. This radiation pressure noise leads to a decrease of the relative sensitivity by a factor of $1/\sqrt{P}$. Radiation pressure noise is a form of so-called *quantum back-action noise*, since it arises from the measurement interaction of the light with the test mass.

While shot noise is white in frequency, radiation pressure noise has a f^{-2} shape due to the inertia of the test-masses. At each frequency in the detection band,

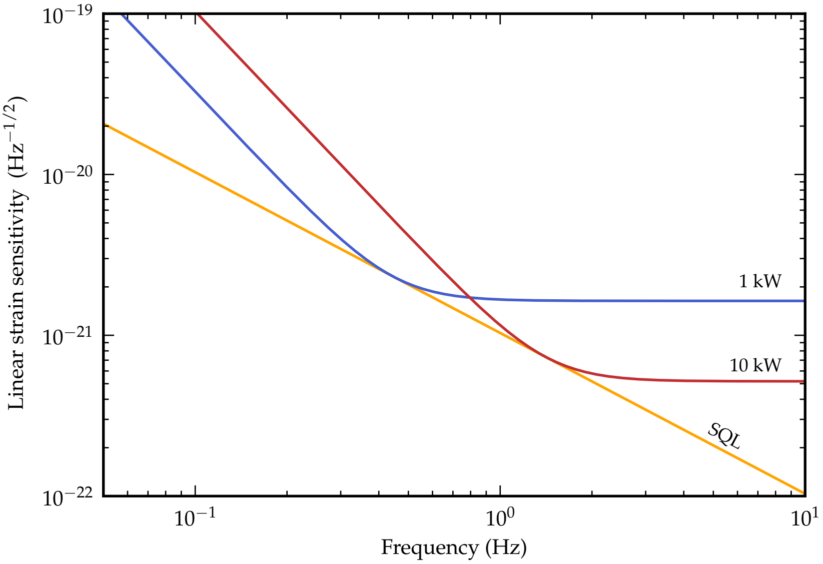

Figure 2.6: Quantum noise of a Michelson interferometer at different input laser powers. An increase by a factor of 10 in laser power yields a reduction of the shot noise by $\sqrt{10}$, while at the same time the radiation pressure noise increases by that factor. For each laser power, there is a frequency where the sensitivity reaches the SQL. An armlength of 1 km, 10 kg end mirrors and a wavelength of 1064 nm were assumed for the simulation.

there is thus an optimum laser power which gives the best trade-off between shot noise and radiation pressure noise. Connecting all optimum points, one obtains the standard quantum limit [Sch10; KLM+01]

$$h^{\mathrm{SQL}} = \sqrt{\frac{4\hbar}{m\Omega^2 L^2}}\,. \tag{2.49}$$

The SQL is also a direct consequence of Heisenberg's uncertainty principle for the position measurement of a free falling test mass with an interferometer. For uncorrelated radiation pressure noise and shot noise, one finds that $S^x S^F \geq \hbar^2$ [BC01]. Thus, the total quantum noise in an interferometer must obey [BGK+03]

$$S^{\mathrm{SQL}} = S_x + \frac{S_F}{\mu^2\Omega^4} \geq \frac{2}{\mu\Omega^2}\sqrt{S_x S_F} = \frac{4\hbar}{m\Omega^2}\,, \tag{2.50}$$

where the Cauchy-Schwarz inequality was used in the second step. Converted into a linear strain spectral density, this result is the same as Eq. (2.49).

Fig. 2.6 shows the SQL for an interferometer with an armlength of 1km and a mirror mass of 10 kg, operating at a wavelength of 1064 nm. In addition, the combined quantum noise is shown for input laser powers of 1 kW and 10 kW.

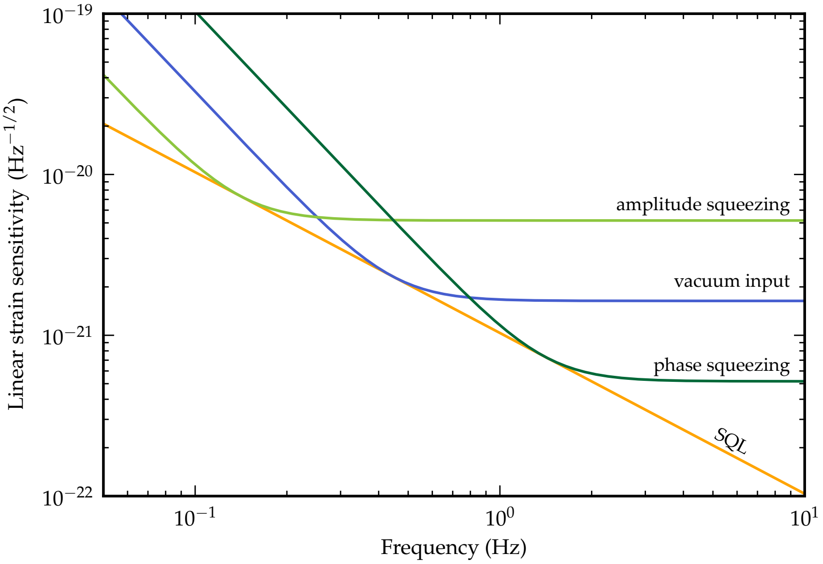

Figure 2.7: Quantum noise of a Michelson interferometer with squeezed light input. A 10 dB phase squeezed state reduces the shot noise by $\sqrt{10}$, while it increases the radiation pressure noise by the same amount. For an amplitude squeezed state, the radiation pressure noise is decreased instead. The simulation parameters are the same as for Fig. 2.6, with an input power of 1 kW.

▸ 2.7.2 *Squeezed-light enhancement*

By shaping the state which enters into the interferometer dark port, the quantum noise of the whole interferometer can be influenced. In 1981, C. Caves proposed to use squeezed vacuum states [Cav81] and he showed that it is then possible to reduce the photon shot noise at the expense of an increased radiation pressure noise, or vice versa. At that time, the low output power of available laser sources was a huge limitation and the possibility of reducing the shot noise without increasing the laser power was intriguing – although squeezed states of light were not demonstrated until 1985 [SHY85]. Today, the motivation for using squeezed states of light is slightly different: a huge circulating laser power can in principle be achieved with high power lasers and power recycling techniques. However, as this imposes a significant thermal load onto the interferometer optics, squeezed light helps in reducing associated problems such as thermal lensing. The resulting quantum noise for the interferometer from Fig. 2.6 with 10 dB squeezed light injection is shown in Fig. 2.7. Depending on the orientation of the squeezing ellipse, either the shot noise (phase quadrature squeezing) or the radiation pressure noise (amplitude quadrature squeezing) is reduced. Already in 1987, squeezed light was used to

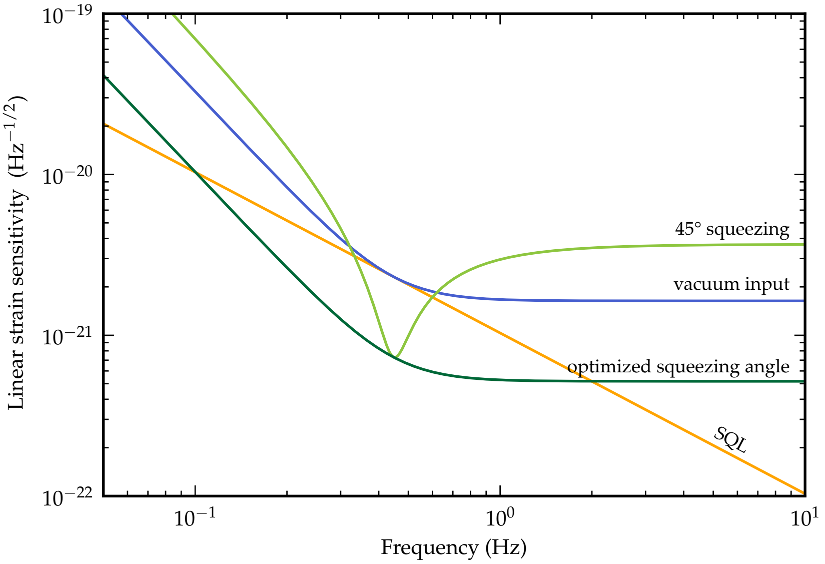

Figure 2.8: Sub-SQL sensitivity of a Michelson interferometer with squeezed light input. A squeezed state rotated by 45° introduces noise correlations which allow a sensitivity beyond the SQL. Optimizing the squeezing angle at each detection frequency achieves a broad-band noise reduction, here by 10 dB (a factor of $\sqrt{10}$). The simulation parameters are the same as for Fig. 2.6, with an input power of 1 kW.

enhance the sensitivity of a table-top interferometer [GSY+87]. Over the past decade, the technique matured enough [MSM+02; VCH+05; VCH+06; GMM+08; VMC+08] such that the gravitational wave detector GEO 600 is now routinely operated with squeezed light input [AAA+11; GDD+13].

In addition, a vacuum state which is squeezed at e.g. an angle of 45° introduces correlations between the shot noise and the radiation pressure noise. Therefore, the SQL is no longer valid [JR90], as it assumes uncorrelated noise sources (arising from the two originally uncorrelated quadratures of the dark port vacuum state). As is shown in Fig. 2.8, by introducing such correlations one can actually beat the SQL in a small frequency regime. The best performance would be achieved for a squeezing ellipse which is optimally rotated for each detection frequency. In this case, the quantum-noise limited sensitivity is enhanced by the squeezing factor over the complete detection band.

References

[AAA+11] J. Abadie, B. P. Abbott, R. Abbott, T. D. Abbott, M. Abernathy, C. Adams, R. Adhikari, C. Affeldt, B. Allen, G. S. Allen, et al. "A gravitational wave observatory operating beyond the quantum shot-noise limit". *Nature Physics* 7 (2011), 962–965. DOI: `10.1038/nphys2083`.

[BC01] A. Buonanno and Y. Chen. "Quantum noise in second generation, signal-recycled laser interferometric gravitational-wave detectors". *Physical Review D* 64 (2001), 042006. DOI: `10.1103/PhysRevD.64.042006`.

[BGK+03] V. Braginsky, M. Gorodetsky, F. Khalili, A. Matsko, K. Thorne, and S. Vyatchanin. "Noise in gravitational-wave detectors and other classical-force measurements is not influenced by test-mass quantization". *Physical Review D* 67 (2003), 082001. DOI: `10.1103/PhysRevD.67.082001`.

[BL05] S. L. Braunstein and P. van Loock. "Quantum information with continuous variables". *Reviews of Modern Physics* 77 (2005), 513–577. DOI: `10.1103/RevModPhys.77.513`.

[Cav80] C. M. Caves. "Quantum-mechanical radiation-pressure fluctuations in an Interferometer". *Physical Review Letters* 45 (1980), 75–79. DOI: `10.1103/PhysRevLett.45.75`.

[Cav81] C. M. Caves. "Quantum-mechanical noise in an interferometer". *Physical Review D* 23 (1981), 1693. DOI: `10.1103/PhysRevD.23.1693`.

[Cav85] C. M. Caves. "New formalism for two-photon quantum optics. I. Quadrature phases and squeezed states". *Physical Review A* 31 (1985), 3068–3092. DOI: `10.1103/PhysRevA.31.3068`.

[CJW+09] E. Cavalcanti, S. Jones, H. Wiseman, and M. Reid. "Experimental criteria for steering and the Einstein-Podolsky-Rosen paradox". *Physical Review A* 80 (2009), 1–16. DOI: `10.1103/PhysRevA.80.032112`.

[DGC+00] L. Duan, G. Giedke, J. Cirac, and P. Zoller. "Inseparability criterion for continuous variable systems". *Physical Review Letters* 84 (2000), 2722–2725. DOI: `10.1103/PhysRevLett.84.2722`.

[DiG10] J. DiGuglielmo. "On the Experimental Generation and Characterization of Entangled States of Light". PhD thesis. Leibniz Universität Hannover, 2010. URN: `urn:nbn:de:gbv:089-6319516797`.

[EPR35] A. Einstein, B. Podolsky, and N. Rosen. "Can quantum-mechanical description of physical reality be considered complete?" *Physical Review* 47 (1935), 777. DOI: `10.1103/PhysRev.47.777`.

[FSB+98] A. Furusawa, J. L. Sørensen, S. L. Braunstein, C. A. Fuchs, H. J. Kimble, and E. S. Polzik. "Unconditional Quantum Teleportation". *Science* 282 (1998), 706–709.

[GDD+13] H. Grote, K. Danzmann, K. L. Dooley, R. Schnabel, J. Slutsky, and H. Vahlbruch. "First Long-Term Application of Squeezed States of Light in a Gravitational-Wave Observatory". *Physical Review L* 110 (2013), 181101. DOI: `10.1103/PhysRevLett.110.181101`. arXiv: `1302.2188`.

[GK05] C. Gerry and P. Knight. *Introductory Quantum Optics*. Cambridge University Press, 2005.

[Gla63] R. J. Glauber. "Coherent and Incoherent States of the Radiation Field". *Physical Review* 131 (6 1963), 2766–2788. DOI: `10.1103/PhysRev.131.2766`.

[GMM+08] K. Goda, O. Miyakawa, E. E. Mikhailov, S. Saraf, R. Adhikari, K. McKenzie, R. Ward, S. Vass, A. J. Weinstein, and N. Mavalvala. "A quantum-enhanced prototype gravitational-wave detector". *Nat. Phys.* 4 (2008), 472–476. DOI: `10.1038/nphys920`.

[GSY+87] P. Grangier, R. Slusher, B. Yurke, and A. LaPorta. "Squeezed-light-enhanced polarization interferometer". *Physical Review Letters* 59 (1987), 2153–2156. DOI: `10.1103/PhysRevLett.59.2153`.

[Har06] J. Harms. "The Detection of Gravitational Waves – Data Analysis and Interferometry". PhD thesis. Leibniz Universität Hannover, 2006.

[HCC+03] J. Harms, Y. Chen, S. Chelkowski, A. Franzen, H. Vahlbruch, K. Danzmann, and R. Schnabel. "Squeezed-input, optical-spring, signal-recycled gravitational-wave detectors". *Physical Review D* 68 (2003), 42001. DOI: `10.1103/PhysRevD.68.042001`.

[HES+12] V. Händchen, T. Eberle, S. Steinlechner, A. Samblowski, T. Franz, R. F. Werner, and R. Schnabel. "Observation of one-way Einstein-Podolsky-Rosen steering". *Nature Photonics* 6 (2012), 598–601. DOI: `10.1038/nphoton.2012.202`.

[JR90] M. T. Jaekel and S. Reynaud. "Quantum Limits in Interferometric Measurements". *Europhysics Letters* 13 (1990), 301. DOI: `10.1209/0295-5075/13/4/003`.

[KLM+01] H. J. Kimble, Y. Levin, A. B. Matsko, K. S. Thorne, and S. P. Vyatchanin. "Conversion of conventional gravitational-wave interferometers into quantum nondemolition interferometers by modifying their input and/or output optics". *Physical Review D* 65 (2001), 22002. DOI: `10.1103/PhysRevD.65.022002`.

[MSM+02] K. McKenzie, D. A. Shaddock, D. E. McClelland, B. C. Buchler, and P. K. Lam. “Experimental demonstration of a squeezing-enhanced power-recycled Michelson interferometer for gravitational wave detection”. *Physical Review Letters* 88 (2002), 231102. DOI: `10.1103/PhysRevLett.88.231102`.

[OPK+92] Z. Y. Ou, S. F. Pereira, H. J. Kimble, and K. C. Peng. “Realization of the Einstein-Podolsky-Rosen Paradox for Continuous Variables”. *Physical Review Letters* 68 (1992), 3663–3666. DOI: `10.1103/PhysRevLett.68.3663`.

[Rei89] M. D. Reid. “Demonstration of the Einstein-Podolsky-Rosen paradox using nondegenerate parametric amplification”. *Physical Review A* 40 (1989), 913–923. DOI: `10.1103/PhysRevA.40.913`.

[SBE+13] S. Steinlechner, J. Bauchrowitz, T. Eberle, and R. Schnabel. “Strong Einstein-Podolsky-Rosen steering with unconditional entangled states”. *Physical Review A* 87 (2013), 022104. DOI: `10.1103/PhysRevA.87.022104`.

[SC85] B. L. Schumaker and C. M. Caves. “New formalism for two-photon quantum optics. II. Mathematical foundation and compact notation”. *Physical Review A* 31 (1985), 3093–3111. DOI: `10.1103/PhysRevA.31.3093`.

[Sch10] R. Schnabel. *Lecture notes: Nonclassical interferometry*. Leibniz Universität Hannover. 2010.

[Sch35] E. Schrödinger. “Discussion of probability relations between separated systems”. *Mathematical Proceedings of the Cambridge Philosophical Society* 47 (1935), 555–563. DOI: `10.1017/S0305004100013554`.

[SHY85] R. Slusher, L. Hollberg, and B. Yurke. “Observation of squeezed states generated by four-wave mixing in an optical cavity”. *Physical Review Letters* 55 (1985), 2409–2412. DOI: `10.1103/PhysRevLett.55.2409`.

[VCH+05] H. Vahlbruch, S. Chelkowski, B. Hage, A. Franzen, K. Danzmann, and R. Schnabel. “Demonstration of a squeezed-light-enhanced power- and signal-recycled Michelson interferometer”. *Physical Review Letters* 95 (2005), 1–4. DOI: `10.1103/PhysRevLett.95.211102`.

[VCH+06] H. Vahlbruch, S. Chelkowski, B. Hage, A. Franzen, K. Danzmann, and R. Schnabel. “Coherent control of vacuum squeezing in the gravitational-wave detection band”. *Physical Review Letters* 97 (2006), 11101. DOI: `10.1103/PhysRevLett.97.011101`.

[VMC+08] H. Vahlbruch, M. Mehmet, S. Chelkowski, B. Hage, A. Franzen, N. Lastzka, S. Goßler, K. Danzmann, and R. Schnabel. “Observation of squeezed light with 10-dB quantum-noise reduction”. *Physical Review Letters* 100 (2008), 33602. DOI: `10.1103/PhysRevLett.100.033602`.

[WJD07] H. M. Wiseman, S. J. Jones, and A. C. Doherty. “Steering, entanglement, nonlocality, and the Einstein-Podolsky-Rosen paradox”. *Physical Review Letters* 98 (2007), 140402. DOI: `10.1103/PhysRevLett.98.140402`.

▸ Chapter 3

Experimental foundations

The quantum-optics experiments in this thesis are built upon a common foundation of tools, techniques and prior results, which are summarized in this chapter.

▸ 3.1 *Squeezed-light generation by parametric down-conversion*

To generate continuous-wave squeezed states of light, one needs to implement a system which provides a two-photon correlated annihilation and creation operator, such that the squeezing operator shown in Eq. (2.17) is formed. In our group, this interaction is generated by parametric down-conversion (PDC) in optical parametric amplifiers (OPAs), where correlated photon pairs at the fundamental wavelength are created from photons at the second harmonic wavelength inside a non-linear crystal. The theory of parametric amplification was mostly developed in the early 1980s (see, e.g., [WM08] for a review). In 1984, B. Yurke realized that strong squeezing can be generated from a single-ended cavity, i.e. a cavity where only the in-coupling mirror has a non-negligible transmission [Yur84]. Soon after, the first generation and detection of squeezed light was reported [SHY85; WKH⁺86].

▸ 3.1.1 *Interaction in a non-linear crystal*

A non-linear crystal is characterized by a significant non-linear response of its polarization field $P(E)$ to an oscillating electric field E, for example when the crystal is placed inside the light field of a cavity. The polarization field can be expanded into a series, $P(E) = \varepsilon_0\big(\chi^{(1)}E + \chi^{(2)}E^2 + \chi^{(3)}E^3 + \cdots\big)$, where $\chi^{(i)}$ is the i-th order dielectric susceptibility and ε_0 is the dielectric permittivity of vacuum. Generally, the susceptibilities are described by tensors, i.e. the polarization response inside an optical material depends on the oscillation direction of the electric field with respect to the crystal axes. The first order susceptibility is responsible for the index of refraction inside a medium, $n = \sqrt{1 + \chi^{(1)}}$, which can strongly depend on the crystals orientation in birefringent media such as calcite. Indeed, as we well see below, birefringence is a necessary property for many applications of non-linear crystals. The second order susceptibility is many orders of magnitude smaller than the first order, such that it only becomes relevant for high intensities of the incident light. Non-linear crystals have $\chi^{(2)}$ values in the order of $10^{-12}\,\frac{\mathrm{m}}{\mathrm{V}}$, putting second-order non-linear effects within reach of the obtainable continuous-wave light intensities inside resonators. $\chi^{(3)}$ effects are generally inaccessible in the continuous-wave regime, but are in fact used to generate squeezed states of light inside optical fibers using the so-called Kerr effect [SLW+01].

Squeezed-light generation inside OPAs makes use of the second-order, $\chi^{(2)}$ non-linear susceptibility. It is easy to see that this effect couples a fundamental electric field $E = E_0 \cos(\omega_0 t)$ oscillating at a frequency ω_0, with a polarization field at twice the frequency:

$$P^{(2)} = \varepsilon_0 \chi^{(2)} E^2(t) = \varepsilon_0 \chi^{(2)} \big(1 + \cos(2\omega_0 t)\big) . \tag{3.1}$$

This polarization field itself gives rise to an emitted electric field at the harmonic frequency. The process can be generalized to a three-photon interaction process, where two photons at frequencies $\omega_+ = \omega_0 + \Omega$ and $\omega_- = \omega_0 - \Omega$ interact with a photon at the sum frequency $2\omega_0$. For the degenerate case $\Omega = 0$, we again have the situation from above. Often, the modes involved are assigned the names *signal*, *idler* and *pump* for historical reasons and we will occasionally use these names when we need to refer to the individual beams. In the quantum mechanical description, the three-photon interaction process is expressed by the Hamiltonian [GK05; WM08]

$$\hat{H} = \underbrace{\hbar\omega_+ \hat{a}_+^\dagger \hat{a}_+ + \hbar\omega_- \hat{a}_-^\dagger \hat{a}_- + 2\hbar\omega_0 \hat{b}^\dagger \hat{b}}_{=\hat{H}_0} + \underbrace{\mathrm{i}\hbar\chi\big(\hat{a}_+\hat{a}_-\hat{b}^\dagger - \hat{a}_+^\dagger \hat{a}_-^\dagger \hat{b}\big)}_{=\hat{H}_1} . \tag{3.2}$$

Here we have introduced the annihilation operators $\hat{a}_+$ and $\hat{a}_-$ for the signal and idler modes as in Chapter 2, as well as $\hat{b}$ for the pump mode at $2\omega_0$. χ is a dimensionless number proportional to the non-linear susceptibility $\chi^{(2)}$. For the generation of squeezed light, little power is converted out of the pump field. Thus we can adopt the *parametric approximation*, wherein the pump mode $\hat{b}$ is assumed to be in a classical state $|\beta\rangle$ and does not loose energy. This allows us to replace the operator $\hat{b}$ by $\beta \mathrm{e}^{-2i\omega_0 t}$ and drop the associated, constant term from $\hat{H}_0$. Without loss of generality we assume β to be real, thus using the pump mode as a phase reference. We then switch to the Dirac interaction picture, defined by

$$\hat{H}_{1,\mathrm{IP}} = \exp\big(\tfrac{\mathrm{i}}{\hbar}\hat{H}_0 t\big)\hat{H}_1 \exp\big(-\tfrac{\mathrm{i}}{\hbar}\hat{H}_0 t\big) , \tag{3.3}$$

and obtain

$$\hat{H}_{1,\mathrm{IP}} = \mathrm{i}\hbar\chi\big(\beta\hat{a}_+\hat{a}_-\,\mathrm{e}^{\mathrm{i}(2\omega_0-\omega_+-\omega_-)t} - \beta\hat{a}_+^\dagger\hat{a}_-^\dagger \mathrm{e}^{-i(2\omega_0-\omega_+-\omega_-)t}\big) . \tag{3.4}$$

As the frequencies in the exponentials cancel, the explicit time dependency vanishes. Finally, the unitary evolution operator reads

$$\hat{U}_1(t) = \exp\big(-\tfrac{\mathrm{i}}{\hbar}\hat{H}_{1,\mathrm{IP}} t\big) = \exp\big(r(\hat{a}_+\hat{a}_- - \hat{a}_+^\dagger\hat{a}_-^\dagger)\big) , \tag{3.5}$$

where $r = \beta\chi t$ has been introduced. This is of the same form as the squeezing operator (2.17), showing that the $\chi^{(2)}$ non-linear interaction can be used to create squeezed states of light.

The variance of the squeezed output spectrum of an OPA can be described by the following formula [WXK87; TYY⁺07]:

$$\mathrm{Var}\big(\hat{X}^{\pm}(\Omega)\big) = 1 \pm \eta \frac{4\sqrt{P/P_{\mathrm{th}}}}{\big(1 \mp \sqrt{P/P_{\mathrm{th}}}\big)^2 + 4\big(\Omega/\kappa\big)^2} \,. \tag{3.6}$$

Here, $\hat{X}^{\pm}$ represents the squeezed $(-)$ and anti-squeezed $(+)$ quadrature, P is the harmonic pump power, P_{th} the harmonic power needed to reach the threshold where the OPA starts to oscillate, κ is the cavity decay rate and η summarizes losses. These parameters will become more meaningful below, in connection with the experimental results.

▸ 3.1.2 *Phase matching*

For an optimum exploitation of the $\chi^{(2)}$ non-linear interaction, the fundamental and harmonic light field have to be co-propagating inside the crystal with a fixed phase relation. For plane waves, this condition means that both wavefronts have to propagate at exactly the same velocity, i.e. the difference in the wave vectors $\boldsymbol{k}_+$, $\boldsymbol{k}_-$ at the fundamental wavelength and $\boldsymbol{k}_{2\omega_0}$ at the harmonic wavelength vanishes,

$$|\boldsymbol{k}_+ + \boldsymbol{k}_- - \boldsymbol{k}_{2\omega_0}| = 0\,. \tag{3.7}$$

This condition can be satisfied by choosing identical indices of refraction at both wavelengths, requiring one of a few common methods. All methods to achieve this so-called *phase matching* rely on birefringence in the crystal and a combination of different polarizations for the signal, idler and pump fields. In uni-axial crystals, the index of refraction is the same along two crystal directions, $n_x = n_y \neq n_z$. The refractive indices are then usually called the *ordinary* index of refraction, $n_o = n_x = n_y$, and the *extraordinary* index of refraction, $n_e = n_z$.

Critical phase matching makes use of the ellipsoidal shape of the dielectric susceptibility. By tuning the angle of the crystal with regard to the incoming signal and idler modes, one can find a propagation axis which satisfies the phase matching condition (3.7). Unfortunately, this type of phase matching leads to a walk-off between the fundamental and harmonic field, which limits the possible propagation length and makes this type unsuitable for use in power-enhancing cavities.

Non-critical phase matching uses light fields which are polarized along the crystal axes and then relies on the difference of the temperature dependence of the refractive index in the ordinary and extraordinary axes to provide the phase matching condition. Two sub-types are commonly used: *type I* phase matching polarizes

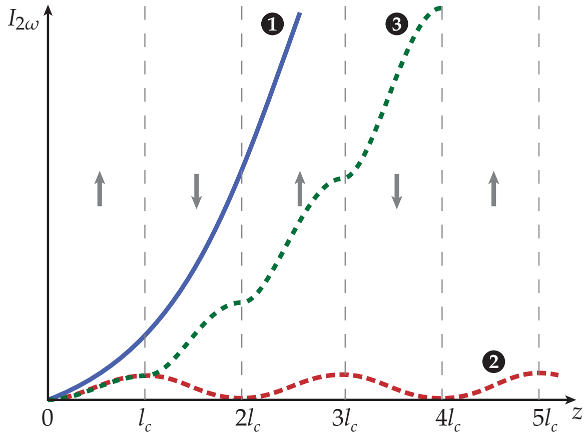

Figure 3.1: Quasi phase matching in periodically poled non-linear crystals. ❶ optimal non-linear response for perfect phase matching, ❷ result of phase-mismatch due to uncompensated phase drift between the fundamental and the harmonic field, ❸ quasi phase matching achieved by periodic poling reversal after each coherence length l_c, as indicated by the gray arrows. (Adapted from [FMJ+92], © 1992 IEEE.)

both signal and idler along the ordinary crystal axis, while the harmonic light is in the orthogonal polarization, along the extraordinary axis. *Type II* phase matching, on the other hand, uses orthogonally polarized signal and idler beams and an extraordinarily polarized harmonic beam. In both cases, a temperature stabilization of the non-linear crystal is needed to obtain the phase matching condition.

The two techniques have different advantages and applications. For example, second harmonic generation is most easily performed with type I phase matching, since signal and idler can simply be replaced by a single, linearly polarized fundamental beam. In addition, squeezed states can be conveniently produced in type I OPAs, since the down-converted photons must have the same polarization. Type II parametric down-conversion is often used as a source for continuous-variable entangled states, requiring only a single OPA. Because the down-conversion process already creates entanglement between signal and idler, a simple polarizing beam splitter is all that is needed to obtain two spatially separated, but entangled modes.

The non-linear coefficient $\chi^{(2)}$ is usually strongest along the crystal's z-direction. Using birefringence as a means to achieve phase matching requires to propagate the light in the x-y-plane, such that the two orthogonal polarizations see the different refractive indices n_o and n_e. Therefore, the maximum non-linear coefficient is out of reach.

Quasi phase matching is another important technique and partly solves this problem. Instead of enforcing well-matched wave vectors, the wave fronts are allowed to drift apart for some propagation distance. After this distance, the so-called *coherence length* l_c, the sign of the susceptibility is changed, letting the difference in wave vectors become smaller again. This process keeps repeating over the length of the crystal, allowing for an almost ideal phase relationship between signal, idler and pump beam. The required periodic poling can be achieved in ferro-electric crystals by applying an external electric field of several kVs after the crystal growth process [CR94; Mil98]. Figure 3.1 shows a schematic drawing of the quasi phase matching effect for the case of second harmonic generation. Curve ❶ represents the intensity build-up along the crystal's optical axis for the harmonic frequency in the case of perfect phase matching. Without phase matching, as represented by curve ❷, the power is converted back and forth between the fundamental and the harmonic with a periodicity of twice the coherence length. Quasi phase matching, curve ❸, reverses the sign of the susceptibility just as the back-conversion sets in, thus increasing again the power in the harmonic mode. Since an ideal phase matching is not achieved, the resulting *effective* non-linearity is a factor of $2/\pi$ lower than the maximum non-linearity of the unpoled material [FMJ+92]. However, the effective non-linearity can still be larger than any of the other non-linear coefficients obtainable by other phase matching methods. In addition, the temperature stability requirements are greatly reduced, since only the period length has to be controlled via thermal expansion. The optimal temperature range for this spans several Kelvin, instead of a very precise, milli-Kelvin control of the refractive indices via $\mathrm{d}n/\mathrm{d}T$.

The phase matching problem is further complicated because the laser beams are strongly focussed into the crystal to obtain the necessary field densities. Thus, the laser beams' *Guoy phases*, an additional phase shift that Gaussian laser beams acquire when going trough their waist, becomes important. The effect of the Gouy phase is strongly dependent on wavelength and waist size, and can significantly alter the required phase-relationship of the waves when entering the crystal. As counter-measures, specially designed cavity mirrors can be used which show an optimized phase difference between the fundamental and harmonic wavelength upon reflection. A detailed treatment of this effect can be found in [LS07].

▸ 3.2 *State-of-the-art preparation of one- and two-mode squeezed light*

State-of-the-art squeezing experiments in our group are able to produce squeezed states of light with a non-classical noise suppression exceeding 12 dB [ESB+10; MAE+11]. To give an overview of such squeezed light generating setups, let us start with a presentation of the main layout and its components, Fig. 3.2.

▸ 3.2.1 *Laser preparation*

The setup starts with a laser preparation stage containing the main laser light source. For the experiments in this thesis, this was a non-planar ring oscillator (NPRO) *Mephisto*, manufactured by INNOLIGHT, emitting about 2 W at 1064 nm. A $\lambda/4$ waveplate followed by a $\lambda/2$ waveplate eliminates any elliptical polarization and matches the resulting linear polarization to the input polarizing beam splitter

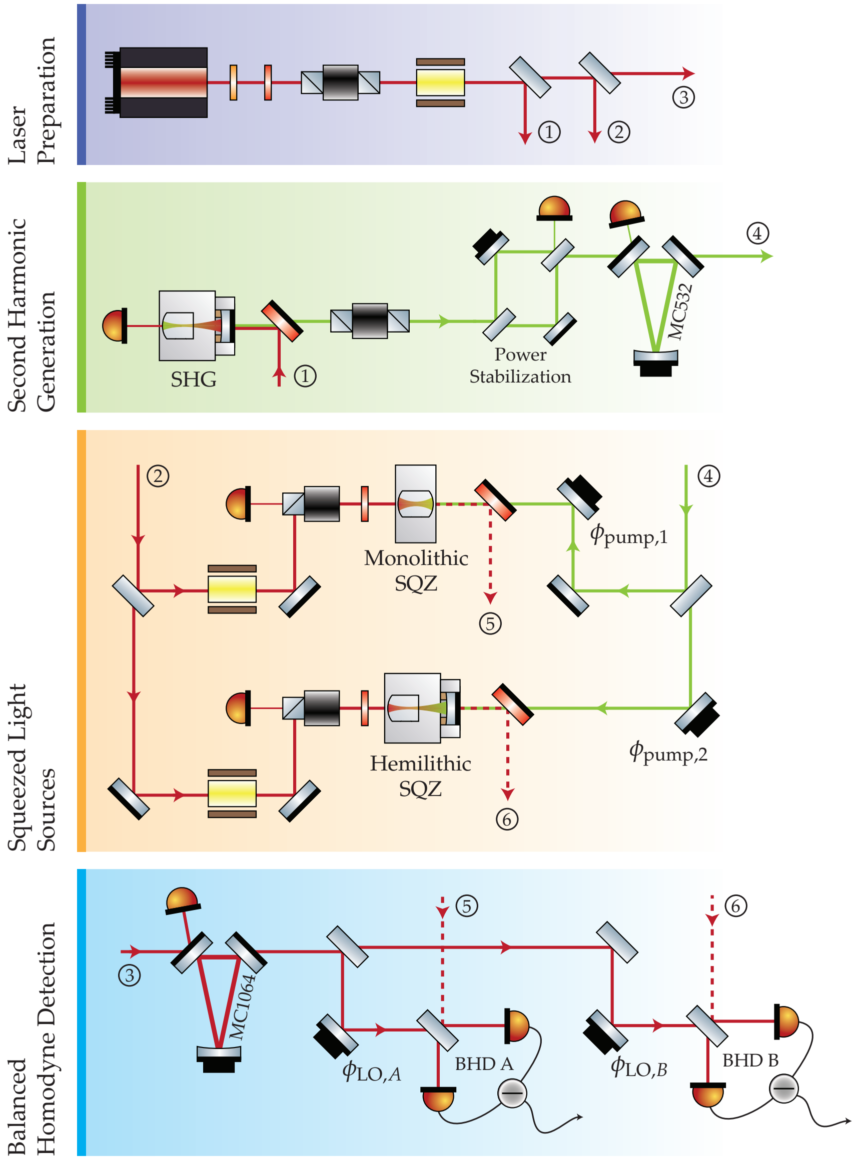
Laser Preparation
①
②
③
Second Harmonic Generation
SHG
①
Power Stabilization
MC532
④
Squeezed Light Sources
②
Monolithic SQZ
⑤
④
$\phi_{\text{pump},1}$
Hemilithic SQZ
⑥
$\phi_{\text{pump},2}$
Balanced Homodyne Detection
③
MC1064
⑤
⑥
$\phi_{\text{LO},A}$
BHD A
$\phi_{\text{LO},B}$
BHD B

Figure 3.2: Schematic of a state-of-the-art experimental setup for the creation of one- and two-mode squeezed states. It consists of four different sections, starting with the preparation and distribution of the main laser light. Second harmonic generation provides the pump light for two squeezed light sources. The squeezed output fields are detected at the balanced homodyne detectors BHD A and BHD B. A key to the diagram can be found in the List of Components on page xix.

(PBS) of a Faraday isolator. It protects the laser from back-reflected light, which would otherwise cause spurious oscillations and frequency instabilities (*mode hopping*). After the isolator, the laser field is phase-modulated with an electro-optic modulator (EOM). This phase modulation is used downstream for electro-optical phase stabilization. The laser light is then distributed to the next stages.

▸ 3.2.2 *Second Harmonic Generation*

Most of the light is converted into the green 532 nm pump field via second harmonic generation (SHG). The non-linear crystal material is 7% magnesium-oxide doped lithium niobate ($MgO{:}LiNbO_3$), temperature phase-matched in a type I configuration. The upconverted light is sent through a Faraday isolator to allow an undisturbed operation of the SHG. The reason for using $LiNbO_3$ instead of PPKTP is the strong green light field inside the resonator: PPKTP shows signs of photochromatic damage, creating color centers inside the crystal structure which lead to increased absorption [BRF⁺99; WPL04]. This effect, also known as gray-tracking, significantly limits the application of PPKTP at lower wavelengths. Indeed, the GEO600 squeezed light source in its early assembly phase used a PPKTP SHG, which strongly deteriorated after a few weeks and was replaced by a $LiNbO_3$ SHG [Kha11]. In my diploma thesis [Ste08], and thereafter in several other experiments in our group [ANS⁺11; MAE⁺11; EHD⁺11], SHG from 1550 nm to 775 nm was performed in PPKTP without any signs of damage to the crystals, underlining that the effect only occurs with the higher photon energies of green light.

A fluctuation in the second harmonic pump field leads to fluctuations in the generated output squeezing, not only in strength, but also in squeezing ellipse rotation due to expansion of the cavity from the varying thermal load. This last point has been extensively investigated by A. Khalaidovski [Kha11], albeit for a different locking scheme where the fluctuation led to a drift in the frequency spacing between s- and p-polarized locking beams. Another problem with pump power fluctuations is connected with the classical gain inside an OPA: it deamplifies the sub-mW OPA control-field by a factor that strongly depends on the pump power, while the phase modulations on the control-field are amplified. This control-field, however, is usually employed for further down-stream locks in co-propagation with the squeezed field. Consequently, a fluctuation of the carrier as well as the modulation sidebands would lead to drifting locking points and generally unstable error signals. State-of-the-art squeezing experiments in our group therefore implement a stabilization of the pump power, e.g. with the help of a small Mach-Zehnder-type interferometer or an electro-optical amplitude modulator (EOAM).

A second, passive stabilization is provided by a mode-cleaning cavity (MC). It is constructed as a three-mirror ring resonator, following the initial LIGO design [WUG⁺98]. The MC acts as a stable reference for the lateral beam position and

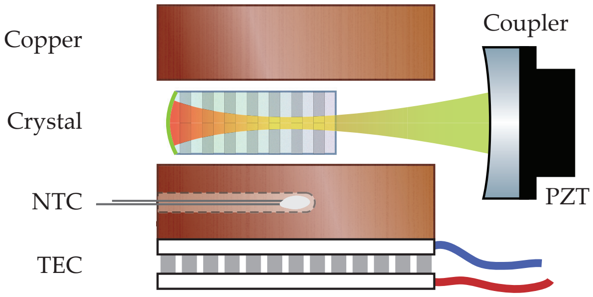

Figure 3.3: Schematic of a hemilithic OPA used for squeezed light generation. The cavity is formed between an out-coupling mirror and the HR coated end-face of the non-linear crystal. Two copper plates enclose the crystal. The assembly is controlled to phase-matching temperature with a TEC.

provides an output which is in a well-defined TEM_{00} mode. In addition, amplitude and phase fluctuations above the resonance linewidth are suppressed by the cavity's transfer function.

The filtered light is split into two paths, providing pump light for the squeezed light sources.

▸ 3.2.3 *Squeezed light source*

In our group, entangled states are produced by overlapping two squeezed beams of light at a beam splitter [FSB+98], creating so-called *s-class* entanglement [DHF+07]. Thus, two OPAs are needed to generate the individual squeezed beams.

The schematic of such an OPA is shown in Fig. 3.3. One side of the PPKTP crystal is highly reflective (HR) coated, while the other side has an anti-reflective (AR) coating. Together with an external out-coupling mirror having a reflectivity of about 90% for the fundamental field, the OPA cavity is formed. The length of this cavity can be fine-tuned by applying a high voltage to a piezo-electric transducer (PZT), which slightly moves the out-coupling mirror. A copper block surrounds the crystal and is thermally contacted to a thermo-electric cooler (TEC). Together with an NTC thermistor and a temperature controller, this serves to hold the crystal at its phase-matching temperature. The second harmonic pump light enters the OPA cavity through the out-coupling mirror.

In addition to this hemilithic squeezer configuration, *HSQZ*, we also use a monolithic configuration, *MSQZ*. In this case, the dielectric out-coupling coating is directly applied to the second crystal end-face. Thus, the crystal itself forms the OPA cavity, keeping the optical loss to a minimum. Both configurations are shown in the setup schematic Fig. 3.2.

A sub-milliwatt control beam is used for stabilizing the cavity lengths of the two OPAs via a Pound-Drever-Hall scheme (PDH) [DHK+83]. For this purpose, the control beam is phase-modulated and then matched into the OPAs through their highly reflective side. To be able to detect the reflected beams, they are separated

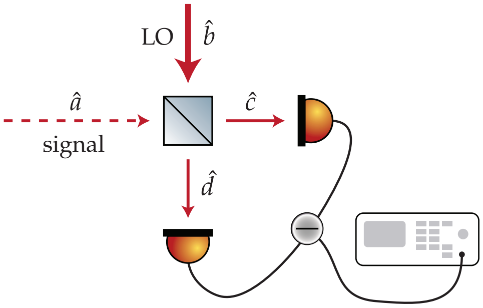

Figure 3.4: Balanced homodyne detection. The signal mode $\hat{a}$ is overlapped with a strong local oscillator (LO) $\hat{b}$ on a 50:50 beam splitter. Both outputs are detected and the photo currents are subtracted from each other. A spectrum analyzer displays the measured noise variance after amplification.

from the incoming beam via a PBS and Faraday rotator combination. Demodulating the detected light at the modulation frequency results in an error signal for the cavity length. The modulation frequency is chosen such that it is within the cavity linewidth. Thus, the phase modulation also undergoes amplification and deamplification depending on the phase of the pump light. This leads to an error signal for the pump phase, again obtained by demodulating the reflected control beam, but now with orthogonal demodulation phase.

In the case of a monolithic cavity, a PZT for cavity length adjustment is missing. Another option would be to adjust the cavity length via thermal expansion. While this has been done by another group [YNF10], it quickly leads to a suboptimal phase matching condition inside the crystal and thus to reduced squeezing output. Alternatively, the frequency of the main laser can be locked to the monolithic cavity, which however allows only one monolithic squeezed light source per experiment.

The produced squeezed light field leaves the OPA cavity through the out-coupling mirror and is separated from the pump field by a dichroic beam splitter (DBS). To investigate its quadrature noise variances, as given by Eq. (3.6), the squeezed light output field is analyzed with a balanced homodyne detector.

▸ 3.2.4 *Balanced homodyne detection*

We use *balanced homodyne detection* (BHD) to analyze the noise properties of the generated squeezed light fields. For this technique, the squeezed signal beam is overlapped on a 50:50 beam splitter with a strong light field, the so-called *local oscillator* (LO), see Fig. 3.4. Both output ports are simultaneously detected with a photo detector. The difference in the photo current is then proportional to a quadrature measurement of the signal field. Mathematically, a homodyne detector is best described in the linearization picture, where the annihilation operator $\hat{a}$ of a field of light is divided into a classical, coherent amplitude $\alpha = \langle \hat{a} \rangle$ and the quantum fluctuations $\delta\hat{a}$. We denote the signal field by $\hat{a} = \alpha + \delta\hat{a}$ and the local oscillator by $\hat{b} = \beta + \delta\hat{b}$. In addition, we choose the coherent amplitudes α and β to be real by extracting the relative phase δ between the two fields as an explicit factor $e^{i\delta}$ assigned to the mode $\hat{a}$. Then, the output modes $\hat{c}$ and $\hat{d}$ of the 50:50 beam splitter are given by

$$\hat{c} = \frac{1}{\sqrt{2}}\left(\hat{a}e^{i\delta} + \hat{b}\right), \tag{3.8}$$

$$\hat{d} = \frac{1}{\sqrt{2}}\left(\hat{a}e^{i\delta} - \hat{b}\right). \tag{3.9}$$

By detecting these light fields, we obtain the photo currents $\hat{\imath}_c$ and $\hat{\imath}_d$, which are proportional to the respective photon numbers,

$$\begin{aligned}\hat{\imath}_c \propto \hat{c}^\dagger\hat{c} &= \frac{1}{2}\left(\hat{a}e^{i\theta} + \hat{b}\right)\left(\hat{a}^\dagger e^{-i\theta} + \hat{b}^\dagger\right)\\ &= \frac{1}{2}\left[\alpha^2 + \beta^2 + 2\alpha\beta\cos\theta + \alpha\left(\delta\hat{X}_1^a + \delta\hat{X}_{-\theta}^b\right) + \beta\left(\delta\hat{X}_1^b + \delta\hat{X}_\theta^a\right)\right], \qquad (3.10)\\ \hat{\imath}_d \propto \hat{d}^\dagger\hat{d} &= \frac{1}{2}\left(\hat{a}e^{i\theta} - \hat{b}\right)\left(\hat{a}^\dagger e^{-i\theta} - \hat{b}^\dagger\right)\\ &= \frac{1}{2}\left[\alpha^2 + \beta^2 - 2\alpha\beta\cos\theta + \alpha\left(\delta\hat{X}_1^a - \delta\hat{X}_{-\theta}^b\right) + \beta\left(\delta\hat{X}_1^b - \delta\hat{X}_\theta^a\right)\right]. \qquad (3.11)\end{aligned}$$

Here we have, as part of the linearization, neglected quadratic fluctuation terms such as $\delta\hat{a}\delta\hat{b}$. In addition we used the definition of the (degenerate) amplitude quadrature operator as in (2.4), as well as the rotated quadrature operator $\hat{X}_\theta = \hat{X}_1\cos\theta + \hat{X}_2\sin\theta = \hat{a}e^{i\theta} + \hat{a}^\dagger e^{-i\theta}$.

Subtracting these two photo currents, we obtain

$$\hat{\imath}_- \propto \hat{c}^\dagger\hat{c} - \hat{d}^\dagger\hat{d} = 2\alpha\beta\cos\theta + \alpha\delta\hat{X}_{-\theta}^b + \beta\delta\hat{X}_\theta^a, \tag{3.12}$$

with a variance of

$$\mathrm{Var}\left(\hat{\imath}_-\right) \propto \alpha^2\,\mathrm{Var}\left(\delta\hat{X}_{-\theta}^b\right) + \beta^2\,\mathrm{Var}\left(\delta\hat{X}_\theta^a\right). \tag{3.13}$$

For a local oscillator much stronger than the signal field, $\beta^2 \gg \alpha^2$, the second term dominates and it is indeed possible to measure any given quadrature $\hat{X}_\theta$ of the signal field with a balanced homodyne detector. For a pure squeezed vacuum state $\alpha = 0$, and the condition of a dominating LO is fulfilled. However, in our setups we usually have a weak control beam co-propagating with the squeezed field, such that the first term of (3.13) can become important again. Let us assume that the local oscillator is shot-noise limited at the measurement frequency, $\mathrm{Var}\left(\hat{X}_{1,2}^b\right) = 1$, and that the signal beam is in a squeezed state with 10 dB noise suppression in the amplitude quadrature, $\mathrm{Var}\left(\hat{X}_1^a\right) = 0.1$. In this case, the LO would have to be a factor of 100 stronger than the signal field such that the noise contribution of the LO would be less than 10%. For typical LO and control beam powers in our squeezing setups of 10 mW and 10 µW, respectively, the contribution is even smaller.

This limitation should however be kept in mind for homodyne detection of an interferometer output, which might not be sufficiently dark due to limited contrast.

A near-perfect 50:50 splitting ratio is necessary for a high common-mode rejection ratio, i.e. good cancelling of the unwanted noise terms in the subtraction process. We therefore fine-tuned the beam splitter ratio by slightly turning it around its vertical axis, thus changing the angle of incidence and thereby the transmission value. Once properly adjusted, the common-mode rejection of our homodyne detectors exceeds 80 dB; the subtracted DC output of the homodyne detector stays within millivolts of its dark-noise value, even for 20 mW local oscillator impinging on the photo diodes.

This treatment assumed a perfect mode overlap between the signal and the local oscillator, as well as perfect photo detection with a quantum efficiency of unity, i.e. one electron is generated for each impinging photon. In practice, both assumptions cannot be perfectly fulfilled and thus lead to a lossy detection. The loss in turn corresponds to an in-coupling of a fraction of the vacuum mode, compare Sec. 2.6, which limits the amount of detectable squeezing. We thus use custom-made photo diodes which have a specified detection efficiency of $> 99\%$. The mode overlap between the two modes on the photo detectors is given by [WXK87]

$$\eta = \left| \int_{\mathcal{A}} U(\boldsymbol{r}) V^*(\boldsymbol{r}) \, \mathrm{d}\boldsymbol{r} \right| , \tag{3.14}$$

where $U(\boldsymbol{r})$ and $V(\boldsymbol{r})$ are the transversal mode profiles of the signal and LO beams, respectively, and $\mathcal{A}$ is the surface of the detector (which is assumed to be large enough to accommodate the whole beam, otherwise the effective quantum efficiency would again become worse). An experimentally accessible measure of the mode overlap is the fringe visibility $\mathcal{V} = 1 - \eta$ at the beam splitter. For equal power in both input ports, it is given by

$$\mathcal{V} = \frac{I_{\max} - I_{\min}}{I_{\max} + I_{\min}} , \tag{3.15}$$

where $I_{\max}$ and $I_{\min}$ are the maximum and minimum intensities obtained in one output of the beam splitter by scanning the phase δ between the two beams.

To obtain a high mode overlap at the homodyne detectors, we first of all make sure that our local oscillator is contained in a well-defined TEM$_{00}$ mode by filtering it with a mode-cleaning ring-cavity. This cavity, similar in parameters to the one used for the green pump beam, furthermore reduces beam pointing fluctuations and suppresses amplitude and phase fluctuations at frequencies above the cavity linewidth.

An auxiliary mode cleaner, as shown in Fig. 3.5, is used as a reference to improve the mode overlap at the homodyne beam splitter [Vah08; Ste08]. First, the signal field is matched to this mode cleaner, establishing a spatial mode reference for the light fields impinging on the homodyne detector's beam splitter. In the next step,

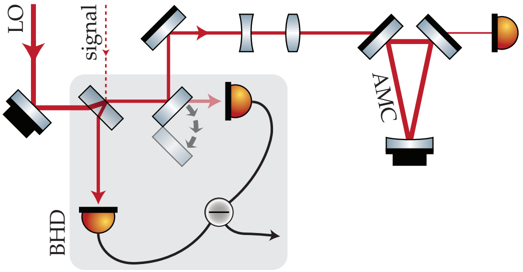

Figure 3.5: Homodyne visibility adjustment with the help of an auxiliary mode cleaner (AMC). A flip mirror in one arm of the balanced homodyne detector (BHD) diverts the light to the auxiliary mode cleaner, which serves as a stable mode reference for the signal beam and local oscillator (LO).

the local oscillator is also matched to this mode cleaner. This ensures that the signal and local oscillator beams propagate in perfect unison, achieving mode overlaps of $> 99.5\%$.

For a correct measurement it is crucial that the homodyne detector electronics perform linearly over a wide range of output powers. This can be easily checked by a measurement series with a vacuum state as signal input. The local oscillator power is doubled in each step, and the resulting output noise variance at the measurement frequency is observed. Plotting the obtained data points in a double logarithmic plot should result in a straight line with a slope of 3 dB per doubling of LO power. This is due to the fact that the noise variance at the measurement frequency comes from the beat signal between the local oscillator intensity at DC and the shot-noise limited noise of the signal vacuum state (and possibly also the local oscillator) at the measurement sideband frequency. While the former doubles for doubled LO power, the latter does not, resulting in a noise variance increase by a factor of 2 (3 dB). Should there be technical noise at the measurement sideband frequency, this noise would increase as well for a doubled LO power, leading to an increase by 6 dB instead – or at least some value larger than 3 dB, depending on the noise source and potential nonlinearity.

▸ 3.2.5 *Preparation of Einstein-Podolsky-Rosen entanglement*

As described in Sec. 2.5.3, entangled fields of light can be created by overlapping two squeezed fields on a beam splitter. Such a setup is shown in Fig. 3.6. The two output modes then form a bipartite entangled system, which for this specific setup is also called a two-mode squeezed state. Locally, the two modes resemble large (i.e. highly excited) thermal states. Comparing simultaneous measurement results of the two output states, however, reveals strong correlations which can surpass the limit set by the EPR-Reid criterion (2.29),

$$\mathcal{E}^2 = \mathrm{Var}\big(\hat{X}_1^A - g_1\hat{X}_1^B\big) \times \mathrm{Var}\big(\hat{X}_2^A - g_2\hat{X}_2^B\big) < 1\,. \tag{3.16}$$

When this conditional variance product falls below unity (for any value of the optimization parameters g_1 and g_2), Einstein-Podolsky-Rosen entanglement is

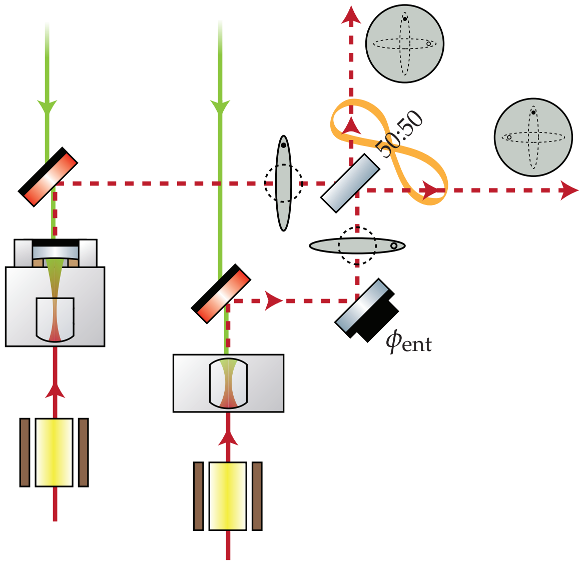

Figure 3.6: Preparation of two-mode squeezed states at a beam splitter. Two squeezed beams are individually produced inside two OPAs. They are overlapped at a 50:50 beam splitter with a relative phase of $\phi_{\text{ent}} = \pi/2$. Each output resembles a local thermal state, which however shows strong correlations with the other output.

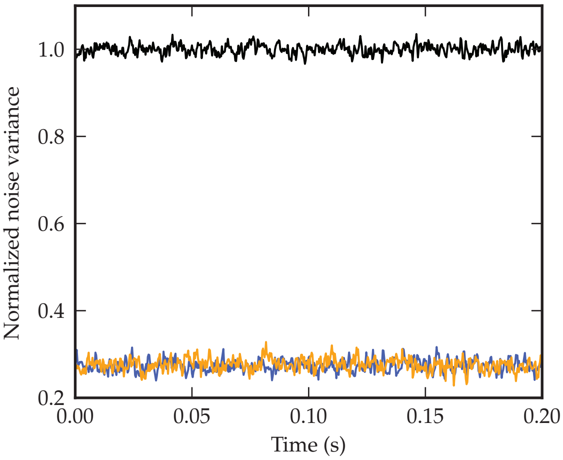

Figure 3.7: Example measurement of continuous-variable entanglement. All noise curves are normalized to the vacuum variance (black curve). The amplitude quadrature difference, $\mathrm{Var}\big(\hat{X}_1^A - X_1^B\big)$ (blue trace), and the sum in the phase quadratures, $\mathrm{Var}\big(\hat{X}_2^A + X_2^B\big)$ (orange trace), clearly fall below the vacuum uncertainty.

verified. By how much the limit of unity is beaten is immediately a measure of the entanglement strength. An example of such a correlation measurement is shown in Fig. 3.7.

References

[ANS+11] S. Ast, R. M. Nia, A. Schönbeck, N. Lastzka, J. Steinlechner, T. Eberle, M. Mehmet, S. Steinlechner, and R. Schnabel. "High-efficiency frequency doubling of continuous-wave laser light". *Optics Letters* 36 (2011), 3467. DOI: `10.1364/OL.36.003467`.

[BRF+99] B. Boulanger, I. Rousseau, J. Feve, M. Maglione, B. Menaert, and G. Marnier. "Optical studies of laser-induced gray-tracking in KTP". *IEEE Journal of Quantum Electronics* 35 (1999), 281–286. DOI: `10.1109/3.748831`.

[CR94] Q. Chen and W. P. Risk. "Periodic poling of $KTiOPO_4$ using an applied electric field". *Electronics Letters* 30 (1994), 18. DOI: `10.1049/el:19941019`.

[DHF+07] J. DiGuglielmo, B. Hage, A. Franzen, J. Fiurášek, and R. Schnabel. "Experimental characterization of Gaussian quantum-communication channels". *Physical Review A* 76 (2007), 12323. DOI: `10.1103/PhysRevA.76.012323`.

[DHK+83] R. Drever, J. Hall, F. Kowalski, J. Hough, G. Ford, A. Munley, and H. Ward. "Laser phase and frequency stabilization using an optical resonator". *Applied Physics B* 31 (1983), 97–105. DOI: `10.1007/BF00702605`.

[EHD+11] T. Eberle, V. Händchen, J. Duhme, T. Franz, R. Werner, and R. Schnabel. "Strong Einstein-Podolsky-Rosen entanglement from a single squeezed light source". *Physical Review A* 83 (2011), 6–9.

[ESB+10] T. Eberle, S. Steinlechner, J. Bauchrowitz, V. Händchen, H. Vahlbruch, M. Mehmet, H. Müller-Ebhardt, and R. Schnabel. "Quantum enhancement of the zero-area sagnac interferometer topology for gravitational wave detection". *Physical Review Letters* 104 (2010), 251102. DOI: `10.1103/PhysRevLett.104.251102`.

[FMJ+92] M. Fejer, G. Magel, D. Jundt, and R. Byer. "Quasi-phase-matched second harmonic generation - Tuning and tolerances". *IEEE Journal of Quantum Electronics* 28 (1992), 2631–2654. DOI: `10.1109/3.161322`.

[FSB+98] A. Furusawa, J. L. Sørensen, S. L. Braunstein, C. A. Fuchs, H. J. Kimble, and E. S. Polzik. "Unconditional Quantum Teleportation". *Science* 282 (1998), 706–709.

[GK05] C. Gerry and P. Knight. *Introductory Quantum Optics*. Cambridge University Press, 2005.

[Kha11] A. Khalaidovski. “Beyond the Quantum Limit – A Squeezed-Light Laser in GEO 600”. PhD thesis. Leibniz Universität Hannover, 2011. URN: `urn:nbn:de:gbv:089-6842290488`.

[LS07] N. Lastzka and R. Schnabel. “The Gouy phase shift in nonlinear interactions of waves”. *Optics Express* 15 (2007), 7211–7217. DOI: `10.1364/OE.15.007211`.

[MAE+11] M. Mehmet, S. Ast, T. Eberle, S. Steinlechner, H. Vahlbruch, and R. Schnabel. “Squeezed light at 1550 nm with a quantum noise reduction of 12.3 dB”. *Optics Express* 19 (2011), 25763. DOI: `10.1364/OE.19.025763`.

[Mil98] G. D. Miller. “Periodically poled lithium niobate: Modeling, fabrication, and nonlinear-optical performance”. PhD thesis. Stanford University, 1998.

[SHY85] R. Slusher, L. Hollberg, and B. Yurke. “Observation of squeezed states generated by four-wave mixing in an optical cavity”. *Physical Review Letters* 55 (1985), 2409–2412. DOI: `10.1103/PhysRevLett.55.2409`.

[SLW+01] C. Silberhorn, P. Lam, O. Weiss, F. König, N. Korolkova, and G. Leuchs. “Generation of continuous variable Einstein-Podolsky-Rosen entanglement via the Kerr nonlinearity in an optical fiber”. *Physical Review Letters* 86 (2001), 4267–4270. DOI: `10.1103/PhysRevLett.86.4267`.

[Ste08] S. Steinlechner. “Gequetschtes Licht bei 1550nm”. Diploma thesis. Leibniz Universität Hannover, 2008.

[TYY+07] Y. Takeno, M. Yukawa, H. Yonezawa, and A. Furusawa. “Observation of -9 dB quadrature squeezing with improvement of phase stability in homodyne measurement”. *Optics Express* 15 (2007), 4321–4327. DOI: `OE.15.004321`.

[Vah08] H. Vahlbruch. “Squeezed Light for Gravitational Wave Astronomy”. PhD thesis. Leibniz Universität Hannover, 2008. URN: `urn:nbn:de:gbv:089-59192949X2`.

[WKH+86] L.-A. Wu, H. J. Kimble, J. L. Hall, and H. Wu. “Generation of Squeezed States by Parametric Down Conversion”. *Phys. Rev. Lett.* 57 (20 1986), 2520–2523. DOI: `10.1103/PhysRevLett.57.2520`.

[WM08] D. F. Walls and G. J. Milburn. *Quantum Optics*. 2nd edition. Springer, 2008.

[WPL04] S. Wang, V. Pasiskevicius, and F. Laurell. “Dynamics of green light-induced infrared absorption in $KTiOPO_4$ and periodically poled $KTiOPO_4$”. *Journal of Applied Physics* 96 (2004), 2023. DOI: `10.1063/1.1738528`.

[WUG+98] B. Willke, N. Uehara, E. K. Gustafson, R. L. Byer, P. J. King, S. U. Seel, and R. L. Savage. “Spatial and temporal filtering of a 10-W Nd:YAG laser with a Fabry-Perot ring-cavity premode cleaner”. *Optics Letters* 23 (1998), 1704. DOI: `10.1364/OL.23.001704`.

[WXK87] L.-A. Wu, M. Xiao, and H. J. Kimble. “Squeezed states of light from an optical parametric oscillator”. *Journal of the Optical Society of America B* 4 (1987), 1465. DOI: `10.1364/JOSAB.4.001465`.

[YNF10] H. Yonezawa, K. Nagashima, and A. Furusawa. “Generation of squeezed light with monolithic optical parametric oscillator: Simultaneous achievement of phase matching and cavity resonance by temperature control”. *Optics Express* 18 (2010), 20143–20150. DOI: `10.1364/OE.18.020143`.

[Yur84] B. Yurke. “Use of cavities in squeezed-state generation”. *Physical Review A* 29 (1984), 408–410. DOI: `10.1103/PhysRevA.29.408`.

▸ Chapter 4

Squeezed-light enhanced zero-area Sagnac interferometer

The results presented in this chapter are published in Physical Review Letters ***104****, 251102 (2010) [ESB+10].*

A decade ago, it was realized that the zero-area Sagnac interferometer topology is able to perform quantum-nondemolition measurements of position changes of a mechanical oscillator [Che03]. Here, it is experimentally shown that such an interferometer can also be efficiently enhanced by squeezed light. A nonclassical sensitivity improvement of up to 8.2 dB is achieved, limited by optical loss inside our interferometer. It is shown that the sensitivity of a squeezed-light enhanced Sagnac interferometer can surpass the standard quantum limit for a broad spectrum of signal frequencies without the need for filter cavities as required for Michelson interferometers. The Sagnac topology is therefore a powerful option for future gravitational wave detectors, such as the Einstein Telescope [ET].

▸ 4.1 *The Sagnac topology for gravitational wave detection*

▸ 4.1.1 *Motivation*

The Sagnac interferometry topology was originally invented by Georges Sagnac in 1913 to measure the effect of angular velocity on a light field's phase [Sag13]. A laser beam is split into two beams at a beam splitter and both beams propagate in opposite directions through the whole interferometer. Upon arriving at the beam splitter again, both beams interfere such that all light goes back to the input, while the output port remains dark. The Sagnac interferometer is sensitive to rotations, leading to a phase shift of

$$\Delta\phi = 8\pi\frac{\boldsymbol{A\omega}}{c\lambda}\,. \tag{4.1}$$

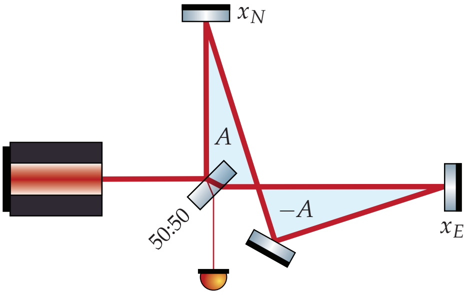

Figure 4.1: A zero-area Sagnac interferometer configuration. The equal, but opposite areas A and $-A$ cancel rotational coupling.

Here, $\boldsymbol{A}$ is the surface normal vector of the area enclosed by the light beam, whose length is given by the size of that area. $\boldsymbol{\omega}$ is the angular velocity describing the rotation of the interferometer. For example, Sagnac interferometers are used to very precisely measure the rotation of the earth [SVR+04], for which $|\omega| \approx 7.3 \times 10^{-5}$ rad/s. For gravitational wave detectors on earth, this rotational sensitivity is a disadvantage, but can be largely suppressed by making the enclosed area zero. This can for example be done by propagating the beam around two equally sized areas, but in opposite directions, see Fig. 4.1. As the two beams inside the interferometer travel along an identical common path, any common-mode noise is effectively suppressed. In addition, the interferometer is insensitive to motions which are sensed by the two counter-propagating beams at the same time. Especially, motions of the near turning mirror do not produce an output signal, as the length difference ΔL between clockwise and counter-clockwise paths is zero. Periodic motions with a period much longer than the round-trip time of the light field are thus also suppressed. The frequency response of a Sagnac interferometer is given by [MRS+97]

$$F_{\mathrm{Sag}}(\Omega) \approx \frac{\omega_0}{\Omega} \sin^2(\Omega L/c)\,, \tag{4.2}$$

whose absolute value is plotted in Fig. 4.2. L is the optical length of one arm, such that the total round-trip length in a Sagnac interferometer is $2L$. As motivated above, F_{Sag} goes to zero towards low frequencies. This leads to a stable passive locking of the interferometer against very slow drifts, such as those caused by the earth's changing gravitational field. In principle, the control effort is reduced to frequencies inside the detection band [Bey01]. In contrast to this, the response of a Michelson interferometer is given by

$$F_{\mathrm{MI}}(\Omega) \approx \frac{\omega_0}{2\Omega} \sin(\Omega L/c)\,, \tag{4.3}$$

which is proportional to a sinc function, $\mathrm{sinc}(x) = \sin(x)/x$, and approaches a constant for low frequencies.

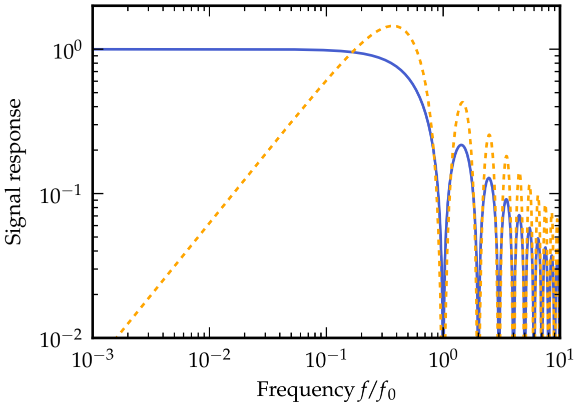

Figure 4.2: Comparison of the frequency response for an interferometer in a Sagnac and a Michelson topology, normalized to the Michelson interferometer's response at DC. The frequency axis is scaled by the normalized frequency $f_0 = c/L$, the inverse storage time of one arm.

Just like for conventional Michelson-type gravitational wave detectors, the sensitivity of Sagnac interferometers can be improved by techniques such as arm cavities and signal recycling. The topology can be arranged in such a way that it closely matches the L-shaped geometry of Michelson interferometers, staying compatible with existing infrastructure.

In the 1990s, several theoretical and experimental studies towards the feasibility of a Sagnac gravitational wave detector were carried out (see, e.g., [SGM98; Bey01; BBF02]). However, no significant advantage over the then more mature Michelson interferometers was found. Thus, the Sagnac topology was no longer pursued for future detector designs. In 2003 however, Yanbei Chen realized that the Sagnac interferometer is a speed meter, i.e. it measures the speed of the test masses instead of their position [Che03]. This makes the Sagnac interferometer a quantum-nondemolition (QND) measurement device (see below), which is fundamentally less affected by radiation pressure noise than a position meter such as the Michelson interferometer. Since the upcoming generation of gravitational wave detectors will already be limited by this noise source at low frequencies, this is a huge benefit of the Sagnac topology and makes it well worth to reconsider for future detector designs.

▸ 4.1.2 *The Sagnac interferometer as a QND device*

Braginsky showed that it is possible to beat the standard quantum limit (SQL, see Sec. 2.7.1) with QND measurement schemes [BV74]. The idea is to find a *QND observable* $\hat{q}$ whose operator commutes at different times,

$$[\hat{q}(t), \hat{q}(t')] = 0\,. \tag{4.4}$$

A measurement at time t therefore does not influence the outcome of the measurement at time t'; there is no back-action of the measurement onto the observable. An example of a QND observable, which is important for the Sagnac interferometer, is the momentum $\hat{p}$ of a free test mass. It is an integral of motion, meaning that it commutes with the unitary time-evolution operator of the system, $[\hat{p},\hat{\mathcal{U}}] = 0$. Thus, measuring $\hat{p}$ will project the system into an eigenstate of $\hat{p}$, which will then be the result of all successive measurements. The QND measurement does not add any uncertainty; the only variation comes from variations of the system itself. For a detailed treatment of QND measurements, see the excellent review articles [BK96; DK12].

Let us now look at why the Sagnac interferometer measures a QND observable, namely the speed of the test masses, which is proportional to their momenta. The two laser beams measure the positions of the two test masses at different times, separated by the time it takes for the light to travel between the two mirrors, $\tau = L/c$. After one round-trip, the clockwise and counter-clockwise propagating beams have obtained a phase shift

$$\Delta\phi_c \propto x_N(t) + x_E(t+\tau)\,, \tag{4.5}$$

$$\Delta\phi_{cc} \propto x_E(t) + x_N(t+\tau)\,, \tag{4.6}$$

where $x_{N,E}(t)$ are the positions of the north and east test mass. The interference fringe at the output depends on the phase difference,

$$\begin{aligned}\Delta\phi &= \Delta\phi_c - \Delta\phi_{cc} &(4.7)\\ &= x_N(t) - x_N(t+\tau) - \big[x_E(t) - x_E(t+\tau)\big]\,. &(4.8)\end{aligned}$$

At frequencies much lower than the inverse round-trip time, we can expand this equation in terms of τ, to obtain

$$\begin{aligned}\Delta\phi &\approx x_N(t) - \big(x_N(t) + \tau\dot{x}_N(t)\big) - \big[x_E(t) - \big(x_E(t) + \tau\dot{x}_E(t)\big)\big] &(4.9)\\ &= \tau\big(\dot{x}_E(t) - \dot{x}_N(t)\big)\,, &(4.10)\end{aligned}$$

where the dot indicates the time derivative. At low frequencies, a Sagnac interferometer thus measures the difference in test mass speed, from which the actual displacement is obtained by integration. Most importantly, the Sagnac interferometer as a speed-meter is significantly less limited by measurement back-action noise than conventional Michelson interferometers, which are position-meters. It can achieve broadband sub-SQL performance without the need for filter cavities [Che03].

▸ 4.2 *Demonstration of a quantum-enhanced Sagnac interferometer*

We demonstrated the quantum enhancement of a zero-area Sagnac interferometer. A schematic of our experiment is given in Fig. 4.3. The squeezed light generation

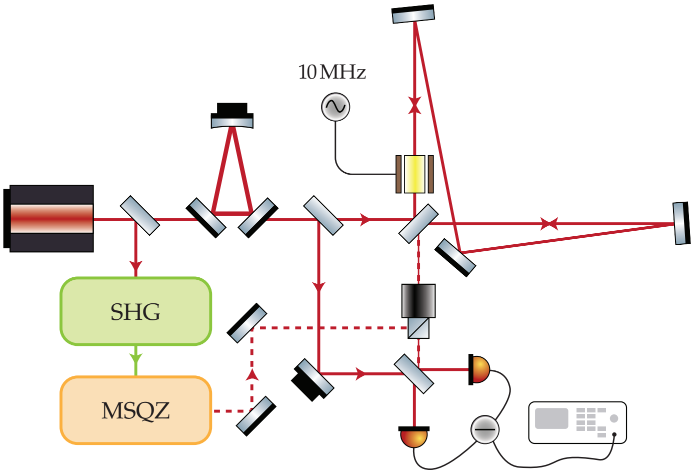

Figure 4.3: Schematic of the quantum-enhanced Sagnac interferometer. The squeezed light from the MSQZ squeezed light source was injected into the interferometer via a PBS and Faraday rotator. Inside the interferometer, a phase modulation was generated with an EOM. A balanced homodyne detector read out the signal.

followed the steps outlined in Sec. 3 and is described in detail in [Bau13]. At its heart was a monolithic squeezed light source (MSQZ), which provided 12.7 dB of squeezing at a second-harmonic pump power of 80 mW. The crystal material was periodically-poled potassium titanyl phosphate (PPKTP), cut to dimensions of $1{\times}2{\times}8.9\,\mathrm{mm}^3$. Both end surfaces were polished with a radius of curvature of 12 mm. One end face was highly reflective coated ($R \approx 99.98\%$) at the wavelengths of 1064 nm and 532 nm, while the other end face had $R = 90\%$ for 1064 nm and $R = 20\%$ for 532 nm. These parameters led to a cavity with a free spectral range of ≈ 9 GHz and waist sizes of 32.8 µm at the fundamental wavelength and 22.8 µm at the harmonic wavelength. The temperature of the crystal was monitored via an NTC thermistor. A feedback loop actuated on the temperature with a thermo-electric cooler (TEC). We determined an optimal phase matching temperature of 37.9 °C, which slightly decreased with increasing pump power due to additional heating from absorption within the crystal.

The Sagnac interferometer had a round-trip length of $2L = 50$ cm, arranged in a folded zero-area configuration. It was operated with a spatially filtered, continuous-wave laser beam at a wavelength of 1064 nm. Close to the beam splitter, we placed an EOM inside one arm to generate a phase modulation which mimicked a gravitational wave signal. We mode-matched the squeezed light into the dark output port of the Sagnac. The interferometer signal was separated via a PBS and Faraday rotator combination. A balanced homodyne detector detected the output

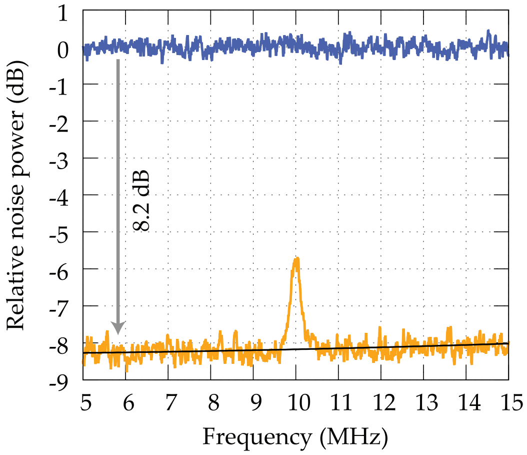

Figure 4.4: Results of the quantum-enhanced Sagnac interferometer. The blue trace shows the 10 MHz phase modulation measured without squeezed light input: no signal is visible. With squeezed light, orange trace, the noise was reduced by about 8.2 dB, revealing the signal. All traces were recorded with a radio bandwidth of 300 kHz, a video bandwidth of 300 Hz and averaged twice. The homodyne detector's dark noise was $22 - 25$ dB below the vacuum noise and was subtracted from the data to give a flat spectrum. The solid line shows a model for the squeezing strength fitted to the data.

field. It was equipped with a pair of high efficiency InGaAs photo diodes. A local oscillator power of 20 mW was used for the homodyne detection. The interferometer itself was operated with 570 µW circulating laser power. We applied a 10 MHz sine wave to the EOM, generating a phase modulation signal at that frequency. The contrast of the interferometer was measured to $\mathcal{C} = 99.7\%$, and the visibility at the homodyne detectors' beam splitter was 99.7%.

Fig. 4.4 shows the obtained spectra of the output signal. The blue trace corresponds to the vacuum fluctuations entering the interferometer through its signal port when the squeezed light was blocked. This trace served as the noise reference and was normalized to unity. The orange trace shows the noise floor when squeezed light was injected into the interferometer's signal port. A non-classical noise reduction of 8.2 dB was observed. In the upper trace, the phase modulation at 10 MHz buried below the vacuum noise. It is however clearly visible in the lower trace. We deduced a total optical loss of 14%, corresponding to an additional loss of 10% introduced by the Sagnac interferometer. This value was in good agreement with independent loss measurements. First of all, the squeezed light was passed twice through a Faraday rotator (Fig. 4.3) which introduced optical loss of about 4%. About 1% of the light was transmitted through the Sagnac interferometer because its central beam splitter deviated from its optimum 50:50 splitting ratio. About 1.5% loss was due to the transmission through the EOM crystal and the imperfect anti-reflection coating of the second beam splitter. And finally each of the three interferometer mirrors transmitted about 1% because their high-reflection coatings were not optimized for the angles of incidence applied.

Figure 4.5 presents the calculated quantum noise spectral densities of a 10 km

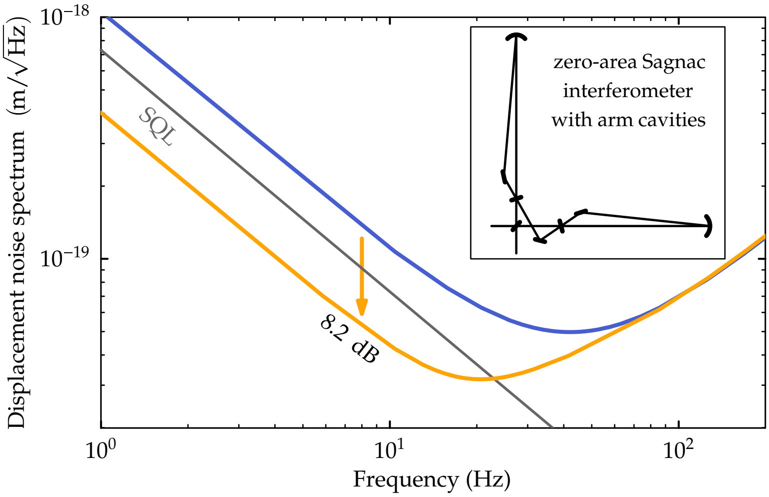

Figure 4.5: Total quantum noise for a displacement measurement of a zero-area Sagnac interferometer with (orange) and without (blue) squeezed-light injection. Our model assumes optical loss to the squeezed light of 9% in total, keeping 8.2 dB of detected squeezing similar to our experiment. The model is further based upon 40 kg test mass mirrors and arm cavities of 10 km length, 80 Hz linewidth, and 10 kW intracavity power. Dividing the linear noise spectral density on the y axis by 10 km yields the noise spectral density for a gravitational wave strain measurement.

Sagnac gravitational wave detector. The traces represent the quantum noise without (blue) and with (orange) squeezed light enhancement. The topology of our simulated Sagnac gravitational wave detector is almost identical to the one in our experiment and is shown in the inset of Fig. 4.5. The only difference is that our simulation used two 10 km-long ring resonators. These arm resonators increase the light's storage time and are oriented perpendicular to each other, and thereby optimize the Sagnac interferometer's sensitivity to the frequency band between 1 Hz and about 40 Hz, which is of high astrophysical interest [PY06]. The squeezing effect at these frequencies is in complete analogy to the one in our experiment. Squeezing down to 1 Hz was demonstrated in [VCD+07]. In Fig. 4.5, the noise spectral density does increase towards lower frequencies not because of remaining back-action noise but due to the decreasing signal transfer function of the Sagnac at lower frequencies. The topology plotted in the inset slightly differs from the one previously proposed in [Che03] in order to keep the effective area of the Sagnac interferometer zero. Note that our topology is still rather simple and does not include a signal recycling resonator. Most importantly, our squeezed-light enhanced zero-area Sagnac interferometer does not require filter cavities in order to gain a broadband sensitivity improvement.

The quantum noise spectra are calculated for 40 kg test mass mirrors and a laser power of 90 W at the central beam splitter. The arm resonators have a linewidth of 80 Hz and store a circulating power of 10 kW. For the squeezed-light generation, injection and detection we assumed optical losses similar to those in our experiment, i.e. 3% loss inside the squeezed light laser, 1% loss due to propagation and non-perfect mode matching, 2% loss per passage through the Faraday rotator, and 1% photo diode inefficiency. We further assumed that the loss inside the interferometer is not significant, which should be achievable with optimized mirror coatings. The total admixture of the vacuum state to the initially pure state therefore is 9%, and the total optical loss to the signal is 3%. In order to achieve the detected squeezing factor of 8.2 dB, we used an initially pure squeezed state of 12.4 dB, which is actually lower than in our experiment. For the interferometer readout we used a balanced homodyne detector as in our experiment. The phase angle between the interferometer signal field and local oscillator was set to 13.7°. For this detection angle a perfect cancellation of back-action noise inside the arm cavity linewidth is achieved. At higher frequencies, back action is overcompensated. However, our interferometer parameters provide an unchanged noise floor. The SQL in Fig. 4.5 is not beaten without the injection of squeezed light because of the high linewidths of the arm cavities and the relatively low laser power applied. A low laser power is important in order to ease the cryogenic operation of the mirrors. We note that the squeezed-light enhanced quantum noise spectrum can be tuned online, i.e. during the operation of the interferometer. By changing the phase angle of the balanced homodyne detector, the overall quantum enhancement can be extended to the frequencies above the half-linewidth of the arm cavities; in this case the quantum enhancement at low frequencies reduces accordingly.

▸ 4.3 *Conclusion*

Here it was experimentally shown that a non-classical reduction of quantum noise in a Sagnac interferometer is possible with squeezed-light injection and balanced homodyne readout. The balanced homodyne readout was an essential part of the experiment since it allowed the optimization of the detected quadrature angle. A theoretical analysis has shown that squeezed-light input and balanced homodyne detection readout is highly compatible with the Sagnac interferometer's intrinsic back-action evading property. Both types of quantum enhancement are essential for future gravitational wave detectors, in particular for the detection of signals in the astrophysically interesting band from 1 Hz to 40 Hz. Therefore, a zero-area Sagnac interferometer with 10 km-long arm cavities targeting this band was considered. It was found that in this signal band a perfect and broadband evasion of back-action noise together with a broadband non-classical shot noise reduction is possible if a certain detection angle is applied. No filter cavities are required. The latter are mandatory in a Michelson interferometer, where not only the back-action noise depends on Fourier frequency, but the anti squeezing of the injected squeezed light also rapidly increases the back-action noise [KLM+01]. The factor by which the standard quantum limit is surpassed only depends on the (frequency independent) squeezing factor achieved. Low-mass mirrors and low laser powers can be used in order to achieve a quantum noise spectral density of about $3 \times 10^{-24}\,\mathrm{Hz}^{-1/2}$. Both low masses and low powers are valuable to reduce thermal noise and enable the cryogenic operation of laser interferometers. A quantum enhanced zero-area Sagnac interferometer is therefore a very suitable candidate for the low frequency part of a future gravitational wave observatory.

References

[Bau13] J. Bauchrowitz. "Messung und graphische Darstellung von Ein-und Zwei-Moden-gequetschten Zuständen des Lichts". PhD thesis. Leibniz Universität Hannover, 2013.

[BBF02] P. T. Beyersdorf, R. L. Byer, and M. M. Fejer. "Results from the Stanford 10 m Sagnac interferometer". *Classical and Quantum Gravity* 19 (2002), 1585–1589. DOI: `10.1088/0264-9381/19/7/348`.

[Bey01] P. T. Beyersdorf. "The polarization sagnac interferometer for gravitational wave detection". PhD thesis. Stanford University, Stanford, California, 2001.

[BK96] V. B. Braginsky and F. Y. Khalili. "Quantum nondemolition measurements: the route from toys to tools". *Review of Modern Physics* 68 (1996), 1–11. DOI: `10.1103/RevModPhys.68.1`.

[BV74] V. Braginsky and Y. Vorontsov. "Quantum-mechanical restrictions in macroscopic measurements and modern experimental devices". *Uspekhi Fizicheskikh Nauk* 114 (1974), 41–53.

[Che03] Y. Chen. "Sagnac interferometer as a speed-meter-type, quantum-nondemolition gravitational-wave detector". *Physical Review D* 67 (2003), 122004. DOI: `10.1103/PhysRevD.67.122004`.

[DK12] S. L. Danilishin and F. Y. Khalili. "Quantum Measurement Theory in Gravitational-Wave Detectors". *Living Reviews in Relativity* 15 (2012), 5. DOI: `10.12942/lrr-2012-5`.

[ESB+10] T. Eberle, S. Steinlechner, J. Bauchrowitz, V. Händchen, H. Vahlbruch, M. Mehmet, H. Müller-Ebhardt, and R. Schnabel. "Quantum enhancement of the zero-area sagnac interferometer topology for gravitational wave detection". *Physical Review Letters* 104 (2010), 251102. DOI: `10.1103/PhysRevLett.104.251102`.

[ET] ET Science Team. *Einstein gravitational wave Telescope conceptual design study*. Tech. rep. ET-0106C-10. 2011.

[KLM+01] H. J. Kimble, Y. Levin, A. B. Matsko, K. S. Thorne, and S. P. Vyatchanin. "Conversion of conventional gravitational-wave interferometers into quantum nondemolition interferometers by modifying their input and/or output optics". *Physical Review D* 65 (2001), 22002. DOI: `10.1103/PhysRevD.65.022002`.

[MRS+97] J. Mizuno, A. Rüdiger, R. Schilling, W. Winkler, and K. Danzmann. "Frequency response of Michelson- and Sagnac-based interferometers". *Optics Communications* 138 (1997), 383–393. DOI: `10.1016/S0030-4018(97)00056-4`.

[PY06] K. A. Postnov and L. R. Yungelson. "The Evolution of Compact Binary Star Systems". *Living Reviews in Relativity* 9 (2006). DOI: `10.12942/lrr-2006-6`.

[Sag13] G. Sagnac. "L'éther lumineux démontré par l'effet du vent relatif d'éther dans un interféromètre en rotation uniforme". *Comptes rendus de l'Académie des sciences* 157 (1913), 708–710.

[SGM98] D. A. Shaddock, M. B. Gray, and D. E. McClelland. "Experimental Demonstration of Resonant Sideband Extraction in a Sagnac Interferometer". *Applied Optics* 37 (1998), 7995. DOI: `10.1364/AO.37.007995`.

[SVR+04] K. U. Schreiber, A. Velikoseltsev, M. Rothacher, T. Klügel, G. E. Stedman, and D. L. Wiltshire. "Direct measurement of diurnal polar motion by ring laser gyroscopes". *Journal of Geophysical Research* 109 (2004), B06405. DOI: `10.1029/2003JB002803`.

[VCD+07] H. Vahlbruch, S. Chelkowski, K. Danzmann, and R. Schnabel. "Quantum engineering of squeezed states for quantum communication and metrology". *New Journal of Physics* 9 (2007), 371. DOI: `10.1088/1367-2630/9/10/371`.

▸ Chapter 5

Quantum-dense metrology

The results presented in this chapter are published in Nature Photonics [SBM+13].

Quantum metrology utilizes entanglement for improving the sensitivity of measurements [GLM04; GLM06; SMM+10]. Up to now the focus has been on the measurement of a single observable. Its orthogonal observable, however, may contain additional information whose knowledge can be used to further improve the measurement result beyond what is possible with state-of-the-art quantum metrology. In this thesis, a laser interferometer is demonstrated which provides information about *two* non-commuting observables, with uncertainties below the meter's quantum ground state. Our experiment is a proof-of-principle of what we call 'quantum-dense metrology', referring to its increased measurement information and its analogy to quantum-dense coding in quantum information science. Our work proposes to use the additional information to distinguish between the actual science signal and parasitic signals originating from scattered and frequency shifted photons. This new approach can be readily applied to improve squeezed-light enhanced gravitational wave detectors at *non*-quantum noise limited detection frequencies by providing a sub shot-noise veto trigger against stray-light induced signals [SBM+13].

▸ 5.1 *Introduction*

The Heisenberg uncertainty principle (HUP) limits the amount of information that can be obtained about non-commuting observables of a physical system. Prominent examples are the position and the momentum of a particle or the amplitude and phase quadratures of an electro-magnetic wave. To optimize the sensitivity of a measurement device under given constraints, such as limited energy, this fact demands a sophisticated design of the 'meter' (or 'probe') system, which couples to the targeted measurement quantity. Moreover, a sophisticated design of the detector that reads out the meter observable, which is an (optimal) estimator of the measurement quantity, is needed [GLM04; KLM$^+$01]. In several proof-of-principle experiments non-classical meter states have been used to 'squeeze' the imprecision in one meter observable to below its zero-point fluctuation, thus entering the regime of *quantum* metrology. The first such experiments were squeezed-light enhanced laser-interferometric phase measurements [SMM$^+$10]. Further examples are phase measurements with entangled photons [RTJ$^+$90; MLS04; AAS10], entangled ions [LBS$^+$04] and nonclassical states of neutral atoms [GZN$^+$10; LSK$^+$11], entanglement assisted nuclear magnetic resonance [CEB$^+$05], and magnetometry with entangled magnetic moments of atomic ensembles [WJK$^+$10]. Recently, quantum metrology was applied to improve an operating gravitational wave detector [AAA$^+$11].

All previous experiments in quantum metrology aimed to improve the signal-to-noise ratio of a single meter observable. In principle, the meter's *orthogonal* observable may contain additional information that has a different physical origin. In this case the two signals are completely independent from each other, i.e. incoherent. So far, a simultaneous quantum measurement of additional incoherent information encoded in the meter's orthogonal observable has not been considered. In general, when using a single, separable and squeezed meter mode, the HUP demands an increased ('anti-squeezed') quantum noise in the orthogonal observable, which prohibits a simultaneous nonclassically improved readout of two non-commuting meter observables.

In this thesis, we propose and implement the concept of *quantum-dense metrology* (QDM), which qualitatively increases the measurement information compared to conventional quantum metrology by simultaneously reading out two conjugate observables. Both observables show a squeezed quantum noise and act as estimators of independent physical quantities. As we will exemplify here, the additional information results in an improved overall measurement process.

▸ 5.2 *Theoretical background*

QDM is based on an Einstein-Podolsky-Rosen (EPR) entangled [EPR35] two-mode system, which has been first proposed for metrology by D'Ariano *et al.* [DLP01]. One mode $\hat{\boldsymbol{m}}$ of the entangled system serves as the new meter state, whereas the other mode $\hat{\boldsymbol{r}}$ is kept as an external reference for the measurement device, see Fig. 5.1. It is in principle possible to exactly measure the distance in phase space between the two modes, since the difference in their canonical positions $\hat{m}_1 - \hat{r}_1$ and the sum of their canonical momenta $\hat{m}_2 + \hat{r}_2$ commute, $[\hat{m}_1 - \hat{r}_1, \hat{m}_2 + \hat{r}_2] = 0$. Thus we overcome the limitation that is set by the Heisenberg uncertainty relation for reading out two orthogonal quadratures of a system by performing all measurements in relation to the reference beam. This situation was recently described as 'quantum-mechanics free' [TC12]. The required (continuous-variable) entangled

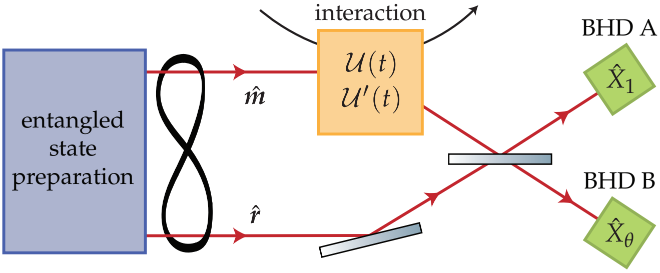

Figure 5.1: Schematic showing the underlying principle of quantum-dense metrology. The measurement uses a bipartite (continuous-variable) entangled state, of which one part $\hat{m}$ (the 'meter') probes two different interactions $\mathcal{U}(t)$ and $\mathcal{U}'(t)$, while the other part is kept as an external reference $\hat{r}$. When leaving the interaction zone, the meter mode carries two informations encoded in two non-commuting observables. Both informations are extracted with squeezed quantum noise by recombining the entangled modes on a beam splitter and by detecting different observables (using two balanced homodyne detectors).

states were first demonstrated by Ou *et al.* [OPK+92] and subsequently by many other groups [FSB+98; SLW+01; BSL03]. They were previously considered for the quantum-informational task of dense coding, which doubles the capacity of quantum communication channels [BW92; BK00]. In contrast to all previously discussed applications of EPR entanglement, QDM benefits from two-mode squeezing of *non*-orthogonal quadratures. Our discussion shows that this opens a way to optimize the science signal-to-noise ratio within QDM.

▸ 5.2.1 *Discussion by Arthurs and Kelly*

The measurement problem of reading out two orthogonal quadratures was first discussed by Arthurs and Kelly (AK) [AK65]. Consider the setup given in Fig. 5.2. An optical field $\hat{m}$ is subjected to two physical interactions $\mathcal{U}(t)$ and $\mathcal{U}'(t)$. They create amplitude and phase modulations on the field, resulting in incoherent, classical amplitude and phase signals $\boldsymbol{s} = (s_1, s_2)$. From the commutation relation (2.5)

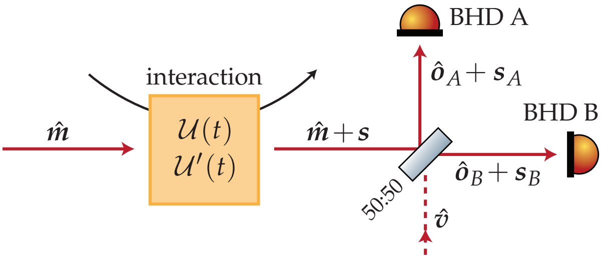

Figure 5.2: Simultaneous read-out of two orthogonal quadratures in an Arthurs-Kelly type setup.

for the amplitude and phase quadrature, one obtains the Heisenberg uncertainty relation

$$\mathrm{Var}\big(\hat{m}_1\big) \times \mathrm{Var}\big(\hat{m}_2\big) \geq 1\,. \tag{5.1}$$

This inequality limits how well the signal $\boldsymbol{s}$ can be extracted from the meter state $\hat{\boldsymbol{m}}$, because the intrinsic quantum noise of the meter state appears in the combined signal-to-noise ratio (SNR) for both quadratures,

$$\frac{\big|s_1\big|^2}{\mathrm{Var}\big(\hat{m}_1\big)} \times \frac{\big|s_2\big|^2}{\mathrm{Var}\big(\hat{m}_2\big)} \leq \frac{\big|s_1\big|^2\big|s_2\big|^2}{1}\,. \tag{5.2}$$

AK theoretically investigated whether the precision of inequality (5.2) can be achieved for a *simultaneous* measurement of both quadratures. As it turns out, an ideal measurement of both quadratures can simply be achieved with a balanced beam splitter and two homodyne detectors. This introduces a vacuum mode $\hat{\boldsymbol{v}}$, which couples into the two beam splitter outputs $\hat{\boldsymbol{o}}_A$ and $\hat{\boldsymbol{o}}_B$ by the transformation

$$\begin{pmatrix}\hat{\boldsymbol{o}}_A\\ \hat{\boldsymbol{o}}_B\end{pmatrix} = \frac{1}{\sqrt{2}}\begin{pmatrix}1 & 1\\ -1 & 1\end{pmatrix}\begin{pmatrix}\hat{\boldsymbol{m}}+\boldsymbol{s}\\ \hat{\boldsymbol{v}}\end{pmatrix} = \frac{1}{\sqrt{2}}\begin{pmatrix}\hat{\boldsymbol{m}}+\boldsymbol{s}+\hat{\boldsymbol{v}}\\ \hat{\boldsymbol{v}}-\hat{\boldsymbol{m}}-\boldsymbol{s}\end{pmatrix}\,. \tag{5.3}$$

The two quadrature components of the signal can be obtained by measuring the $\hat{X}_1$ quadrature of $\hat{\boldsymbol{o}}_A$ and the $\hat{X}_2$ of $\hat{\boldsymbol{o}}_B$. Let us assume that the initial probe state is in an amplitude-squeezed vacuum mode with squeezing parameter r. The quantum noise contribution to the detection is then given by

$$\mathrm{Var}\big(\hat{o}_{A,1}\big) = \frac{1}{2}\big(\mathrm{Var}\big(\hat{m}_1\big)+\mathrm{Var}\big(\hat{v}_1\big)\big) = \frac{1}{2}\big(\exp(-2r)+1\big)\,, \tag{5.4}$$

$$\mathrm{Var}\big(\hat{o}_{B,2}\big) = \frac{1}{2}\big(\mathrm{Var}\big(\hat{m}_2\big)+\mathrm{Var}\big(\hat{v}_2\big)\big) = \frac{1}{2}\big(\exp(+2r)+1\big)\,. \tag{5.5}$$

The signals s_1 and s_2 are also equally divided at the beam splitter, thus we have the following signal strengths at detectors A and B:

$$\big|s_{A,1}\big|^2 = \frac{1}{2}\big|s_1\big|^2\,, \tag{5.6}$$

$$\big|s_{B,2}\big|^2 = \frac{1}{2}\big|s_2\big|^2\,. \tag{5.7}$$

We obtain the following expression for the signal-to-noise ratio [AK65]:

$$\frac{\big|s_{A,1}\big|^2}{\mathrm{Var}\big(\hat{o}_{A,1}\big)} \times \frac{\big|s_{B,2}\big|^2}{\mathrm{Var}\big(\hat{o}_{B,2}\big)} = 4 \times \frac{\big|s_{A,1}\big|^2\big|s_{B,2}\big|^2}{2+2\cosh(2r)} \tag{5.8}$$

$$= \frac{\big|s_1\big|^2\big|s_2\big|^2}{2\times\big(1+\cosh(2r)\big)} \tag{5.9}$$

$$\leq \frac{\big|s_1\big|^2\big|s_2\big|^2}{4}\,. \tag{5.10}$$

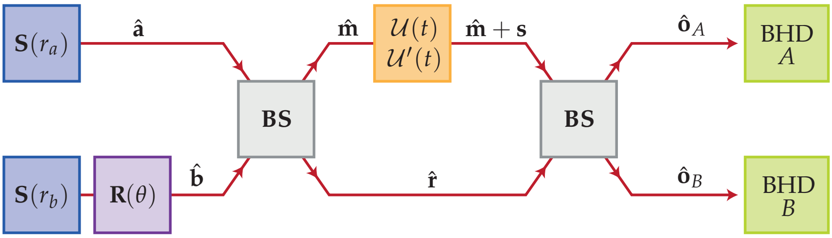

Figure 5.3: Simultaneous, quantum-dense readout of two orthogonal quadratures. This block-diagram visualizes the denominations used in the derivation. $\mathbf{S}(r)$, squeezing; $\mathbf{R}(\theta)$, rotation; **BS**, beam splitter; $\mathcal{U}(t)$, physical interaction; BHD, balanced homodyne detection.

Therefore, a simultaneous measurement of both quadratures leads to a signal-to-noise ratio that is at least four times smaller than indicated by the Heisenberg uncertainty relation (5.2). Squeezing does not help in this measurement scenario, as the best signal-to-noise ratio is obtained for $r = 0$.

▸ 5.2.2 *Quantum-dense readout*

The key concept for an improved readout of two orthogonal quadratures is to encode the signal not in a single meter state, but instead in the difference between two entangled states. Such a difference measurement is not limited by a Heisenberg uncertainty relation. Instead, the achievable sensitivity is directly connected to the squeezing parameters of the initial two-mode squeezed state.

Consider two squeezed vacuum modes with squeezing parameters r_a and r_b, described by the quadrature vectors $\hat{\boldsymbol{a}}$ and $\hat{\boldsymbol{b}}$, see Fig. 5.3. To ease the notation, mode $\hat{\boldsymbol{a}}$ shall be squeezed in the amplitude quadrature $\hat{a}_1$, while mode $\hat{\boldsymbol{b}}$ shall be squeezed in the rotated quadrature $\hat{b}_\theta = \hat{b}_1 \cos\theta + \hat{b}_2 \sin\theta$. After entangling these beams at a 50:50 beam splitter, one mode is used as the meter state $\hat{\boldsymbol{m}} = (\hat{\boldsymbol{a}} + \hat{\boldsymbol{b}})/\sqrt{2}$. After the interaction, it carries the signals s_1 and s_2 as above. The other state $\hat{\boldsymbol{r}} = (\hat{\boldsymbol{a}} - \hat{\boldsymbol{b}})/\sqrt{2}$ is kept as a reference beam. These two modes are then recombined at another beam splitter, whose two output fields $\hat{\boldsymbol{o}}_A$ and $\hat{\boldsymbol{o}}_B$ are sent to balanced homodyne detectors A and B. They detect the quadrature fields

$$\hat{o}_{A,1} = \frac{1}{\sqrt{2}}(\hat{m}_1 + s_1 + \hat{r}_1) \tag{5.11}$$

$$= \hat{a}_1 + \frac{1}{\sqrt{2}} s_1 \tag{5.12}$$

and

$$\hat{o}_{B,\theta} = \frac{1}{\sqrt{2}}(\hat{m}_\theta + s_\theta - \hat{r}_\theta) \tag{5.13}$$

$$= \hat{b}_\theta + \frac{1}{\sqrt{2}} s_\theta \,, \tag{5.14}$$

respectively. Here, the subscript θ denotes again a quadrature rotation, e.g., $\hat{o}_{B,\theta} = \hat{o}_{B,1}\cos\theta + \hat{o}_{B,2}\sin\theta$ and accordingly for $\hat{m}_\theta$, $\hat{r}_\theta$ and s_θ. For this readout, the signal-to-noise ratio is given by

$$\frac{|s_{A,1}|^2}{\mathrm{Var}(\hat{o}_{A,1})}\frac{|s_{B,\theta}|^2}{\mathrm{Var}(\hat{o}_{B,\theta})} = \frac{|s_1|^2}{2\times\mathrm{Var}(\hat{a}_1)}\frac{|s_\theta|^2}{2\times\mathrm{Var}(\hat{b}_\theta)} = \frac{|s_1|^2|s_\theta|^2}{4\times\mathrm{e}^{-2(r_a+r_b)}} \,. \tag{5.15}$$

It is unbounded and for squeezing parameters $r_a + r_b > 0.694$, this quantum-dense readout outperforms the conventional readout scheme based on a single separable mode.

▸ 5.3 *Experimental demonstration of quantum-dense metrology*

In this work we experimentally proved the principle of quantum-dense metrology and its high potential for improving state-of-the-art laser interferometers. Our setup uses quadrature-entangled light to read out two conjugate quadratures of a Michelson interferometer, in direct analogy to Fig. 5.1.

▸ 5.3.1 *Source of quadrature-entangled light*

We generated continuous-variable entangled light as outlined in Sec. 3.2.5 and published in [SBE$^+$13]. Details of the entanglement source are given in [Bau13]. Two squeezed vacuum fields were generated by type I parametric down-conversion in PPKTP in a monolithic (MSQZ) and a hemilithic (HSQZ) optical parametric amplifier (OPA). Sub-milliwatt control beams were employed to lock the OPAs on resonance. Compared to the setup in [SBE$^+$13], the phase modulation frequencies on the control beams were set to lower frequencies of 47.8 MHz (MSQZ) and 32.5 MHz (HSQZ) instead of 68.8 MHz and 47.8 MHz, respectively. This way, the phase modulations were less attenuated by the cavities' linewidths, resulting in larger error signals and more robust locks.

We entangled the two squeezed fields with a variable relative phase θ at a 50:50 beam splitter. To lock the relative phase, we employed a single sideband (SSB) modulation technique similar to [DSH$^+$11], depicted in Fig. 5.4. About 15 mW laser light was frequency-shifted by 80 MHz with an acousto-optic modulator (AOM). It was overlapped with the squeezed field of the HSQZ at the dichroic beam splitter

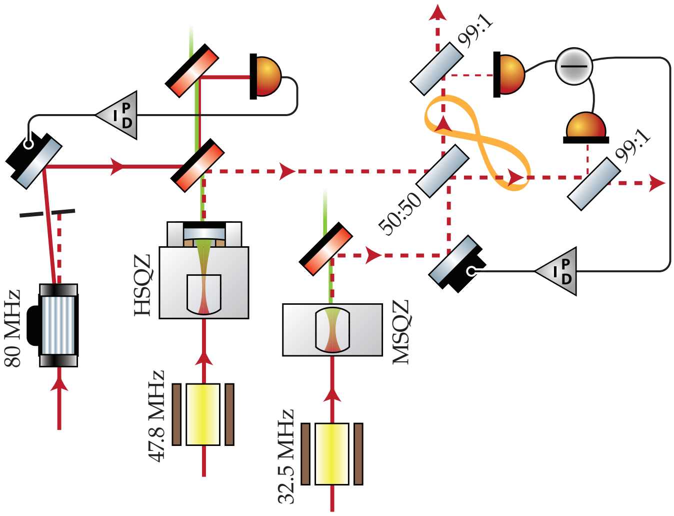

Figure 5.4: Single-sideband control scheme for the entanglement phase lock. The SSB at 80 MHz was generated with an AOM and phase locked to the HSQZ control beam in reflection of the dichroic beam splitter. In both outputs of the entanglement beam splitter, a small pick-off beam was detected. The detector outputs were subtracted and demodulated at the SSB frequency, generating an error signal for the entanglement phase.

(DBS), see Fig. 5.4. The DBS had a transmission of about 500 ppm for s-polarized light. For alignment purposes, we rotated the field into p-polarization, which increased the DBS transmission to a few percent. In both beams after the 50:50 beam splitter, we sent 1% of the light to a photo detector. Subtracting the two detector outputs and demodulating the difference voltage at 80 MHz resulted in an error signal for the entanglement phase. By adjusting the demodulation phase, any entanglement phase could be selected. Unfortunately, parasitic amplitude modulations coming from the AOM led to strong fluctuations of the error signal offset. In principle, the amplitude modulation could be removed by filtering the single sideband with an additional mode cleaner, acting as a frequency filter. There was however insufficient space left in our setup to implement such a cavity.

Similar to Fig. 3.5, an auxiliary mode cleaner was used to optimize the beam overlap between the two squeezed fields at the entanglement beam splitter. It was also used to align the single sideband such that it co-propagated with the HSQZ squeezed field.

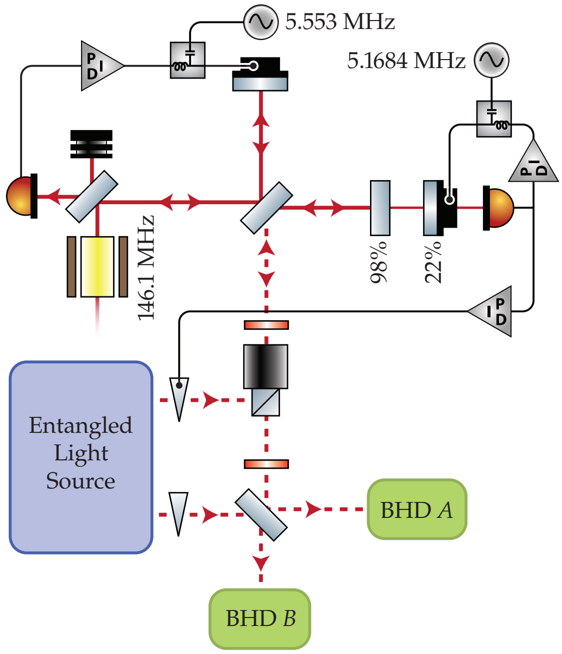

Figure 5.5: Michelson interferometer for the demonstration of quantum-dense metrology. A photo diode in reflection locked the IFO to its dark fringe. The east arm had an end-mirror cavity, which was used to produce a parasitic signal in an arbitrary quadrature. At both PZT mounted mirrors, the high-voltage locking signal was combined with the modulation frequency using bias tees. One part of the entangled state was sent into the IFO via a PBS and Faraday rotator. At the output beam splitter, it was recombined with the second entangled mode and detected at two BHDs.

▸ 5.3.2 *Interferometer with stray-light signal generation*

The Michelson interferometer, displayed in Fig. 5.5, had an arm length of about 7.5 cm for the north arm. The east arm was about 1.5 cm shorter, which allowed us to use the so-called Schnupp modulation technique [Sch88] for locking the interferometer to its dark fringe. For this, the interferometer input beam was phase-modulated at 146.1 MHz. Due to the difference in arm-length, the microscopic detuning needed for destructive interference in the interferometer output was slightly different for the carrier field and the modulation sidebands. A small amount of phase modulation appeared at the interferometer output, giving rise to a beat signal with the carrier whenever the output was not completely dark. This beat signal was used as an error signal for locking the interferometer. Instead of detecting this signal at the interferometer output port, we detected it in reflection of the interferometer behind a $R = 68\%$ beam splitter.

The two end-mirrors were flat and had a power reflectivity of 99.98% (M_N) and 98% (M_{E1}). The north mirror was PZT mounted to create a phase modulation inside the interferometer. A second PZT mounted flat mirror M_{E2} with a reflectivity of $\approx 22\%$ was placed a few millimeters behind M_{E1}, creating a (weakly coupled) Fabry-Pérot cavity. By tuning this cavity, the phase signal created by M_{E2} could be rotated into an arbitrary quadrature, as shown in Fig. 5.6. A small amount of light

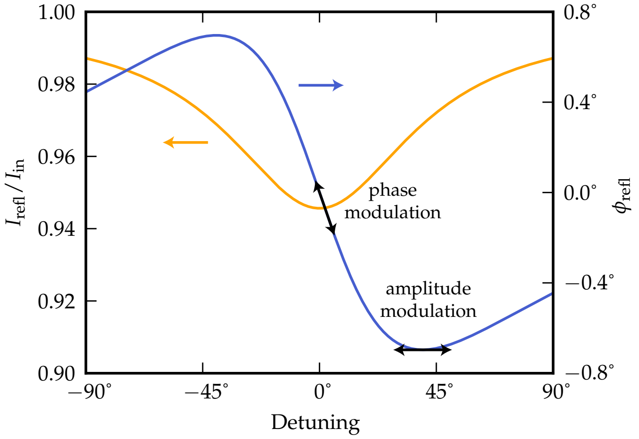

Figure 5.6: Intensity and phase of the light in reflection of a strongly under-coupled cavity. Modulating the cavity at resonance results in a phase modulation signal in reflection of the cavity, while modulating the cavity at a detuning of 40° produces an amplitude modulation.

was transmitted by the cavity. With a DC offset locking scheme, we were able to lock the cavity to any point on the resonance edge, thus setting its operating point. M_N was modulated by a 5.553 MHz sine voltage with an amplitude of 15 mVpp, while M_{E2} was modulated at a frequency of 5.1684 MHz with an amplitude of 300 mVpp. Both frequencies were chosen such that they excited a mechanical resonance of the respective mirror, to obtain sufficiently strong signals in the megahertz regime where the detected squeezing was strongest.

About 10 mW light power was used to operate the interferometer. One mode of the entangled state was mode-matched into the output port via a PBS and Faraday rotator. An error signal for controlling its phase was generated from the beat between the interferometer field and the SSB co-propagating with the entangled mode. The beat was detected in transmission of the end-mirror cavity and demodulated at the SSB frequency. By adjusting the demodulation phase, any orientation of the entangled state could be locked.

With this setup, we were able to simulate a phase signal at 5.553 MHz, as well as a parasitic interference (at 5.1684 MHz) in any quadrature. Such a disturbance naturally occurs in any measurement device due to re-scattering of meter state quanta from moving surfaces [VCD+07].

▸ 5.3.3 *Simultaneous homodyne detection scheme*

The modulations on the transmitted HSQZ and MSQZ control beams were used to lock the homodyne angles of the two balanced homodyne detectors at the interferometer output. Since the squeezed-light sources were operated such that they produced amplitude squeezing, the phase modulation on each control beams was orthogonal to the particular squeezed quadrature. Upon demodulating the homodyne detector output at the modulation frequency, one obtains an error signal

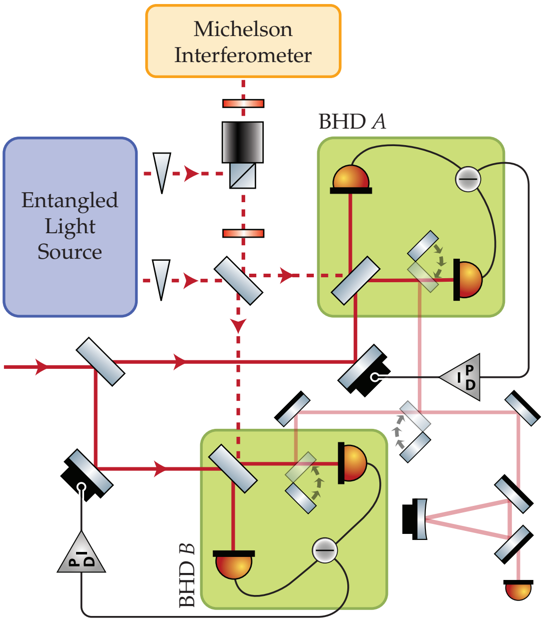

Figure 5.7: Schematic of balanced homodyne interferometer readout. After recombination of the meter and the reference mode, both outputs were detected with balanced homodyne detectors A and B. Their electronic signals were demodulated at the control beam modulation frequencies, creating an error signal for the homodyne detection angles which were adjusted via the PZT-mounted mirrors in the local oscillator paths. An auxiliary mode cleaner served as a spatial mode reference onto which all beams were matched, resulting in a high interference contrast at the beam splitters.

which has a zero crossing exactly when the detector cannot see a phase modulation, i.e. when it measures the squeezed quadrature of the respective squeezed-light source. Thus, by demodulating the output of detector A at 47.8 MHz and the output of detector B at 32.5 MHz, we were able to lock the two detectors to the initial squeezing ellipses.

An additional auxiliary mode cleaner served as a spatial mode reference for all beams arriving at the BHDs. A combination of flip mirrors was used to match each beam to that mode cleaner. In this way, a high interference contrast at the recombination beam splitter, as well as on the homodyne beam splitters was achieved.

The electronic output signals of the homodyne detectors were recorded with two spectrum analyzers *FSU* and *FSP* by Rohde & Schwarz. All spectra, covering the frequency range between 5.0 MHz and 5.7 MHz, were taken with a radio bandwidth of 100 kHz, a video bandwidth of 100 Hz and a sweep-time of 1.4 s.

▸ 5.4 *Results*

The results of our experiment are presented in Fig. 5.8. Each point in the spectra shown corresponds to the noise power of an operator $\hat{X}_i = \hat{X}_i(\Omega, \Delta\Omega)$, where $\Delta\Omega$ is the spectral width defined by the resolution bandwidth set at the spectral analyzer (10 kHz in our case). The nonclassical sensitivity improvement in panel

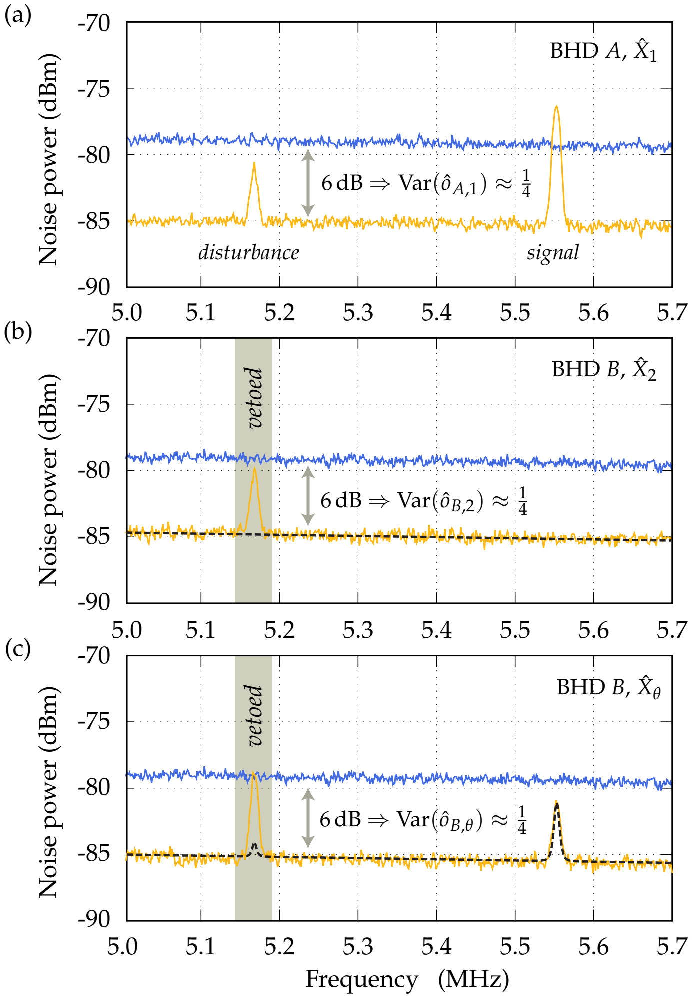

Figure 5.8: Experimental demonstration of quantum-dense metrology. The orange traces show the (unnormalised) simultaneously squeezed quadrature noise-power spectra $\mathrm{Var}(\hat{X}_1)(\Omega)$ (BHD *A*, panel (a)) and $\mathrm{Var}(\hat{X}_2)(\Omega)$ or $\mathrm{Var}(\hat{X}_\theta)(\Omega)$ (BHD *B*, panel (b) and (c), respectively) in comparison with the respective spectra of the meter's zero-point fluctuations (blue). The panels (b) and (c) reveal parasitic signals due to their unexpected scaling. The calculated scalings of science signals are shown in the dashed black curves. In panel (c), the angle θ was tuned so that part of the true science signal was recovered. All traces are slightly sloped due to the decreasing transfer function of the homodyne detectors. They were recorded with a resolution bandwidth of $\Delta\Omega = 10\,\mathrm{kHz}$, a video bandwidth of 100 Hz, and were averaged three times.

(a) is about 6 dB ($r_a \approx 0.69$). *At the same time*, the interferometer's sensitivity in the orthogonal quadrature $\hat{X}_2$, panel (b), is about 6 dB better than the classical case as well ($r_b \approx 0.69$). Panels (a) and (b) clearly surpass the limit set by inequality (5.10), and even outperform inequality (5.2).

QDM uses the simultaneous squeezing in two orthogonal quadratures to improve the overall measurement, in this case by identifying a parasitic (disturbance) signal, as described in the following. BHD A measures the amplitude quadrature (panel (a), orange trace), which generally provides the highest signal-to-noise-ratio for the interferometric science signal (here at 5.55 MHz). BHD A also clearly detects a second (parasitic) signal at 5.17 MHz. Looking at $\hat{X}_2$ with BHD B, panel (b), the phase signal at 5.55 MHz vanishes as expected, while the signal at 5.17 MHz does not vanish but actually increases in size. This information is sufficient to reveal the parasitic nature of the lower frequency signal, which can thus be excluded ('vetoed') from further data analysis.

In Fig. 5.8 (c), we used an improved strategy to reveal the parasitic signal. We detuned the angle θ between the original squeezing ellipses away from 90°. In this way it is possible to retain at least part of the science signal in BHD B, while still having insight into the orthogonal quadrature. As the projection of a phase signal measured at BHD A into the $\hat{X}_\theta$ quadrature can be exactly calculated, any discrepancy reveals a parasitic signal. The dashed black lines in panels (b) and (c) show the projected noise power, assuming that the panel (a) contains only phase signals. While the signal at 5.55 MHz perfectly matches the expectation, the disturbance at 5.17 MHz clearly does not. The advantage of the measurement in panel (c) is that, together with the panel (a), the overall signal-to-noise-ratio of the science signal is improved. Changing θ allows for a smooth tuning between full signal coverage ($\theta = 0$), but no information about the conjugate observable; and maximum information about the disturbances in the full phase space ($\theta = \pi/2$), but loss of half the science signal power.

▸ 5.5 *Discussion*

In the following we discuss the application of QDM in state-of-the-art measurement devices. Generally, to achieve high quantum-noise limited sensitivities, very bright states have to be used. Current laser-interferometric gravitational wave (GW) detectors use light fluxes of about 10^{20} photons per second [AAD+92]. Just a single photon per second and Hertz which is backscattered from a vibrating surface, and in this way frequency shifted into the detection band, produces a significant *parasitic interference* signal. Such disturbances are a well-known problem in high-precision laser interferometry [VBB96; VCD+07; OFW12] and are ultimately a fundamental problem in any measuring device aiming for high quantum noise limited sensitivities. We presume that the sensitivity limitation at lower detection frequencies as observed in the squeezed-light enhanced GW detector GEO 600 [AAA$^+$11] at least partially originates from parasitic interferences. Using QDM in GEO 600, in direct analogy to Fig. 5.5, would allow to clarify which of the (low frequency) signals are parasitic and which occur in the quadrature where GWs are expected.

▸ 5.6 *Conclusion*

In conclusion, we have introduced and experimentally demonstrated the concept of quantum-dense metrology. QDM employs entanglement to achieve a simultaneous nonclassical readout of two conjugate observables, which are estimators for quantities originating from independent physical processes. Our approach uses steady-state entanglement and therefore does not rely on any kind of conditioning or post-selection, which would result in a loss of measurement time. For the first time we propose two-mode squeezing for metrology that is generated with a non-orthogonal relative squeezing angle. Such entangled states allow the optimization of the signal-to-noise ratio when QDM is applied.

We experimentally showed that QDM is superior to conventional quantum metrology. QDM can be used to distinguish between scientific and parasitic signals with a precision beyond the ground state uncertainty. While our application of QDM does not help in the case of parasitic signals that occur solely in the phase quadrature, e.g. caused by thermally excited fluctuations of mirror surfaces and radiation pressure forces, it is a valuable tool against all types of parasitic signals having a phase space orientation different from the phase quadrature. Beyond what we have demonstrated here, it should be even possible to subtract parasitic signals from the measurement data without subtracting science signals. For this, two assumptions have to be made. First, the parasitic signals have a quasi-stationary phase space orientation, second, the science signals have a temporal or spectral shape that is different from the parasitic signal. Then a fitting parameter could be introduced that describes by which magnitude the parasitic signal is projected onto the conventional readout quadrature of the interferometer. Fitting parameters are already used in data analysis based on matched filtering and signal templates [SS09]. In both scenarios, QDM allows for sub shot-noise measurements even if the apparatus without QDM is limited by parasitic interferences, i.e. is not quantum noise limited. Beyond the identification of parasitic signals, QDM might find application in all measurement interactions where different physical processes independently interact with non-commuting observables of the meter system. We envision that QDM will widen the application of quantum metrology in ongoing and future high precision measurements.

References

[AAA$^+$11] J. Abadie, B. P. Abbott, R. Abbott, T. D. Abbott, M. Abernathy, C. Adams, R. Adhikari, C. Affeldt, B. Allen, G. S. Allen, et al. "A gravitational wave observatory operating beyond the quantum shot-noise limit". *Nature Physics* 7 (2011), 962–965. DOI: `10.1038/nphys2083`.

[AAD$^+$92] A. Abramovici, W. E. Althouse, R. W. Drever, Y. Gürsel, S. Kawamura, F. J. Raab, D. Shoemaker, L. Sievers, R. E. Spero, K. S. Thorne, et al. "LIGO: The Laser Interferometer Gravitational-Wave Observatory." *Science* 256 (1992), 325–33. DOI: `10.1126/science.256.5055.325`.

[AAS10] I. Afek, O. Ambar, and Y. Silberberg. "High-NOON states by mixing quantum and classical light." *Science* 328 (2010), 879–81. DOI: `10.1126/science.1188172`.

[AK65] E. Arthurs and J. L. Kelly. "B.S.T.J. Brief: On the simultaneous measurement of a pair of conjugate observables". *Bell System Technical Journal* 44 (1965), 725.

[Bau13] J. Bauchrowitz. "Messung und graphische Darstellung von Ein-und Zwei-Moden-gequetschten Zuständen des Lichts". PhD thesis. Leibniz Universität Hannover, 2013.

[BK00] S. L. Braunstein and H. J. Kimble. "Dense coding for continuous variables". *Physical Review A* 61 (2000), 042302. DOI: `10.1103/PhysRevA.61.042302`.

[BSL03] W. P. Bowen, R. Schnabel, and P. K. Lam. "Experimental Investigation of Criteria for Continuous Variable Entanglement". *Physical Review Letters* 90 (2003), 4–7. DOI: `10.1103/PhysRevLett.90.043601`.

[BW92] C. H. Bennett and S. J. Wiesner. "Communication via one-and two-particle operators on Einstein-Podolsky-Rosen states". *Physical Review Letters* 69 (1992), 2881–2884. DOI: `10.1103/PhysRevLett.69.2881`.

[CEB$^+$05] P. Cappellaro, J. Emerson, N. Boulant, C. Ramanathan, S. Lloyd, and D. Cory. "Entanglement Assisted Metrology". *Physical Review Letters* 94 (2005). DOI: `10.1103/PhysRevLett.94.020502`.

[DLP01] G. M. D'Ariano, P. Lo Presti, and M. G. a. Paris. "Using Entanglement Improves the Precision of Quantum Measurements". *Physical Review Letters* 87 (2001), 270404. DOI: `10.1103/PhysRevLett.87.270404`.

[DSH$^+$11] J. DiGuglielmo, A. Samblowski, B. Hage, C. Pineda, J. Eisert, and R. Schnabel. "Experimental Unconditional Preparation and Detection of a Continuous Bound Entangled State of Light". *Physical Review Letters* 107 (2011), 1–5. DOI: `10.1103/PhysRevLett.107.240503`.

[EPR35] A. Einstein, B. Podolsky, and N. Rosen. “Can quantum-mechanical description of physical reality be considered complete?” *Physical Review* 47 (1935), 777. DOI: `10.1103/PhysRev.47.777`.

[FSB⁺98] A. Furusawa, J. L. Sørensen, S. L. Braunstein, C. A. Fuchs, H. J. Kimble, and E. S. Polzik. “Unconditional Quantum Teleportation”. *Science* 282 (1998), 706–709.

[GLM04] V. Giovannetti, S. Lloyd, and L. Maccone. “Quantum-enhanced measurements: beating the standard quantum limit.” *Science* 306 (2004), 1330–6. DOI: `10.1126/science.1104149`.

[GLM06] V. Giovannetti, S. Lloyd, and L. Maccone. “Quantum Metrology”. *Physical Review Letters* 96 (2006), 010401. DOI: `10.1103/PhysRevLett.96.010401`.

[GZN⁺10] C. Gross, T. Zibold, E. Nicklas, J. Estève, and M. K. Oberthaler. “Nonlinear atom interferometer surpasses classical precision limit.” *Nature* 464 (2010), 1165–9. DOI: `10.1038/nature08919`.

[KLM⁺01] H. J. Kimble, Y. Levin, A. B. Matsko, K. S. Thorne, and S. P. Vyatchanin. “Conversion of conventional gravitational-wave interferometers into quantum nondemolition interferometers by modifying their input and/or output optics”. *Physical Review D* 65 (2001), 22002. DOI: `10.1103/PhysRevD.65.022002`.

[LBS⁺04] D. Leibfried, M. D. Barrett, T. Schaetz, J. Britton, J. Chiaverini, W. M. Itano, J. D. Jost, C. Langer, and D. J. Wineland. “Toward Heisenberg-limited spectroscopy with multiparticle entangled states.” *Science* 304 (2004), 1476–8. DOI: `10.1126/science.1097576`.

[LSK⁺11] B. Lücke, M. Scherer, J. Kruse, L. Pezzé, F. Deuretzbacher, P. Hyllus, O. Topic, J. Peise, W. Ertmer, J. Arlt, et al. “Twin matter waves for interferometry beyond the classical limit.” *Science* 334 (2011), 773–6. DOI: `10.1126/science.1208798`.

[MLS04] M. Mitchell, J. Lundeen, and A. Steinberg. “Super-resolving phase measurements with a multiphoton entangled state”. *Nature* 429 (2004), 161–164. DOI: `10.1038/nature02493`.

[OFW12] D. J. Ottaway, P. Fritschel, and S. J. Waldman. “Impact of upconverted scattered light on advanced interferometric gravitational wave detectors”. *Optics Express* 20 (2012), 8329. DOI: `10.1364/OE.20.008329`.

[OPK⁺92] Z. Y. Ou, S. F. Pereira, H. J. Kimble, and K. C. Peng. “Realization of the Einstein-Podolsky-Rosen Paradox for Continuous Variables”. *Physical Review Letters* 68 (1992), 3663–3666. DOI: `10.1103/PhysRevLett.68.3663`.

[RTJ+90] J. Rarity, P. Tapster, E. Jakeman, T. Larchuk, R. Campos, M. Teich, and B. Saleh. "Two-photon interference in a Mach-Zehnder interferometer." *Physical review letters* 65 (1990), 1348–1351. DOI: `10.1103/PhysRevLett.65.1348`.

[SBE+13] S. Steinlechner, J. Bauchrowitz, T. Eberle, and R. Schnabel. "Strong Einstein-Podolsky-Rosen steering with unconditional entangled states". *Physical Review A* 87 (2013), 022104. DOI: `10.1103/PhysRevA.87.022104`.

[SBM+13] S. Steinlechner, J. Bauchrowitz, M. Meinders, H. Müller-Ebhardt, K. Danzmann, and R. Schnabel. "Quantum-Dense Metrology". *Nature Photonics* (2013). DOI: `10.1038/nphoton.2013.150`.

[Sch88] L. Schnupp. *Presentation at European Collaboration Meeting on Interferometric Detection of Gravitational Waves (Sorrent, Italy).* Sorrent, Italy, 1988.

[SLW+01] C. Silberhorn, P. Lam, O. Weiss, F. König, N. Korolkova, and G. Leuchs. "Generation of continuous variable Einstein-Podolsky-Rosen entanglement via the Kerr nonlinearity in an optical fiber". *Physical Review Letters* 86 (2001), 4267–4270. DOI: `10.1103/PhysRevLett.86.4267`.

[SMM+10] R. Schnabel, N. Mavalvala, D. E. McClelland, and P. K. Lam. "Quantum metrology for gravitational wave astronomy". *Nature Communications* 1 (2010), 121. DOI: `10.1038/ncomms1122`.

[SS09] B. Sathyaprakash and B. Schutz. "Physics, astrophysics and cosmology with gravitational waves". *Living Rev. Relativity* 12 (2009). DOI: `10.12942/lrr-2009-2`.

[TC12] M. Tsang and C. Caves. "Evading Quantum Mechanics: Engineering a Classical Subsystem within a Quantum Environment". *Physical Review X* 2 (2012), 031016. DOI: `10.1103/PhysRevX.2.031016`.

[VBB96] J.-Y. Vinet, V. Brisson, and S. Braccini. "Scattered light noise in gravitational wave interferometric detectors: Coherent effects". *Physical Review D* 54 (1996), 1276–1286. DOI: `10.1103/PhysRevD.54.1276`.

[VCD+07] H. Vahlbruch, S. Chelkowski, K. Danzmann, and R. Schnabel. "Quantum engineering of squeezed states for quantum communication and metrology". *New Journal of Physics* 9 (2007), 371. DOI: `10.1088/1367-2630/9/10/371`.

[WJK+10] W. Wasilewski, K. Jensen, H. Krauter, J. J. Renema, M. V. Balabas, and E. S. Polzik. "Quantum Noise Limited and Entanglement-Assisted Magnetometry". *Physical Review Letters* 104 (2010), 1–4. DOI: `10.1103/PhysRevLett.104.133601`.

▸ Chapter 6

Entangled-light enhanced detuned signal recycling

▸ 6.1 *Motivation*

In a perfect interferometer stabilized to a dark output port, all laser light is reflected back towards the laser input. Seen from the input port, the interferometer thus acts as a highly reflecting mirror. It is therefore possible to form a cavity from a *power-recycling* mirror in the input path and the interferometer itself. This cavity then resonantly enhances the circulating laser light inside the interferometer, resulting in several kilowatts of light power at the interferometer beam splitter, with only a few watts of input power.

The same can be done at the output port, which for a perfect interferometer contains only the signal sidebands which were produced from differential arm-length changes; implementing a *signal-recycling* (SR) mirror at the output resonantly enhances the signal sidebands inside the cavity's linewidth [Mee88]. Two modes of operation are usually distinguished: a *tuned* mode, where the signal-recycling resonance coincides with the laser frequency (zero signal frequency), and a *detuned* mode, where the resonance is offset by a few hundred hertz. In tuned mode, the interferometer's sensitivity is enhanced at low frequencies, while the detuned mode shows a strong peak sensitivity at the detuning frequency. The detuning frequency can, in principle, be changed on the fly by actuating the signal-recycling mirror. This can be used to follow gravitational wave events – such as an inspiral or merger – with a high peak sensitivity. In addition, the signal-recycling cavity imposes a *mode-healing* effect on the output field, reducing loss due to imperfect mode matching [HSM+98]. GEO600 was the first gravitational wave detector to adopt signal recycling [WAA+02], and it is now an essential ingredient of the second generation baseline designs [Har10; AVirgo].

Squeezed light input has significant implications for operating an interferometer with detuned signal recycling [CDR+98; HCC+03]. The squeezed light is reflected at the signal-recycling cavity and acquires a frequency-dependent phase shift around

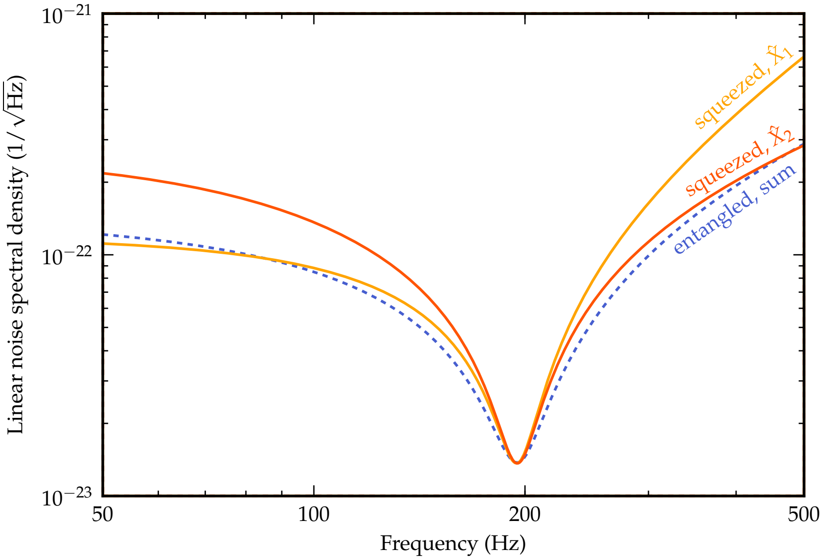

Figure 6.1: Simulation of a GEO600-like interferometer with detuned signal-recycling and 10 dB squeezed light readout. The sensitivity shows a pronounced resonance at the detuning frequency and differs between a detection of the $\hat{X}_1$ and the $\hat{X}_2$ quadrature. Here, the input squeezing angle was chosen in each case such that maximum squeezing occurs on resonance. Entangled light allows for a simultaneous readout of both quadratures, which – when added coherently – results in the blue sensitivity curve.

the resonance. Since the resonance is detuned from the laser carrier frequency, the phase shift is different for the upper and lower sidebands of the squeezed field. This results in a frequency-dependent rotation of the squeezing ellipse around the signal-recycling resonance. Consequently, the resonance feature is strongly enhanced: the sensitivity at resonance is increased by the squeezing strength, while the off-resonance sensitivity is deteriorated by anti-squeezed noise. It has been shown both theoretically [KLM+01; HCC+03; SHS+04] and experimentally [VCH+05] that the squeezing rotation can be cancelled by reflecting the squeezed light at a *filter cavity* before injection into the interferometer. This would be in addition to a filter cavity which is already required to provide a broadband squeezed sensitivity in the radiation-pressure noise as well as the shot-noise limited regime (cf. Sec. 2.7.2). Since the filter cavity resonance structure would have to closely match the signal-recycling cavity resonance, similar optical and geometric properties are required. To attain the required linewidth, the filter cavity would have to be about as long as the interferometer arms, or it would have to possess a very high finesse – albeit with very low optical loss [EBH+13]. In either case, one faces significant technical challenges, making it well worth to think about different approaches. For example, both signal sidebands could be equally enhanced, such that a rotation of the squeezing ellipse does not occur. It has been proposed and demonstrated that this behaviour can be achieved with a second signal-recycling mirror (*twin-signal recycling*), which creates a resonance doublet centered on the carrier frequency [TSL+07; TGV+09].

Detuned signal recycling partly converts the interferometer output signal from a phase modulation into a single-sideband modulation, because it enhances one signal sideband, while the other sideband is suppressed. This gives rise to an additional, opto-mechanical resonance [BC01], but also distributes the signal into both field quadratures at the interferometer output. As can be seen in Fig. 6.1, the achievable sensitivity by detecting the $\hat{X}_1$ and $\hat{X}_2$ quadrature at the output is, however, not identical. In both cases, the input squeezing ellipse was oriented such that maximum squeezing occurred at the cavity resonance. Towards low frequencies, the $\hat{X}_1$ quadrature provides the best signal-to-noise ratio (SNR), while above the resonance, the situation changes in favor of the $\hat{X}_2$ quadrature. Unfortunately, only one of the two sensitivity curves can be detected at a time: along with selecting a different output quadrature, the input squeezing ellipse has to be rotated by $\pi/2$. Thus, the corresponding orthogonal output quadrature will be buried in anti-squeezed noise.

Here, a readout scheme similar to quantum-dense metrology (Sec. 5) comes into play. It allows to read out two orthogonal quadratures at the same time, with sub shot-noise performance. The two quadrature outputs can then be coherently added to obtain the final detector sensitivity curve. In this thesis, a simulation for an entangled-light enhanced readout of an interferometer with detuned signal recycling was developed and the results are presented in the following.

▸ 6.2 *Theoretical description*

The simulation of entangled-light enhanced readout for detuned signal recycling is based on a quantum-noise model of GEO600 [Har02; HCC+03]. It uses the quantum-optical modulation picture, as reviewed in Sec. 2, to describe the input-output relation of the interferometer. The output state $\hat{\boldsymbol{o}}$ is composed of a noise contribution from the dark-port input state $\hat{\boldsymbol{\imath}}$ and a potential gravitational wave signal h,

$$\hat{\boldsymbol{o}} = \frac{1}{M}\left(\mathbf{T}\hat{\boldsymbol{\imath}} + \hat{\boldsymbol{s}}h\right). \tag{6.1}$$

Here, $\mathbf{T}$ is the noise transfer function mapping the vacuum input state $\hat{\boldsymbol{\imath}}$ onto the output state $\hat{\boldsymbol{o}}$. The gravitational wave signal is shaped by the signal transfer function $\hat{\boldsymbol{s}}$. Both $\mathbf{T}$ and $\hat{\boldsymbol{s}}$, as well as the common factor M are frequency dependent.

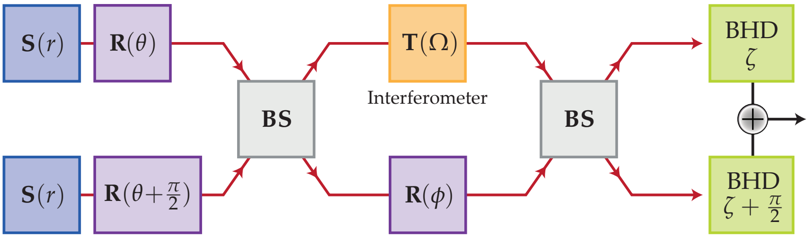

Figure 6.2: Block diagram representing the simulation for the entangled readout of a detuned signal-recycled interferometer (see text for details). $\mathbf{S}(r)$, squeezing; $\mathbf{R}(\theta)$, rotation; **BS**, beam splitter; $\mathbf{T}(\Omega)$, interferometer transfer matrix; BHD, balanced homodyne detection.

Their exact representation is lengthy, see e.g. [HCC+03], but is also of little interest here.

The sensitivity of an interferometer at a given frequency is generally given as a (single-sided) noise spectral density $S_h(\Omega)$. It can be calculated by normalizing the noise at the detection frequency by the signal at that frequency. Since the noise is characterized by $\mathbf{T}$ and the signal is characterized by $\hat{\mathbf{s}}$, the expression (2.26) can be used to obtain [HCC+03]

$$S_h(\Omega) = \frac{\langle\zeta|\mathbf{T}\mathbf{T}^\dagger|\zeta\rangle}{\langle\zeta|\hat{\mathbf{s}}\hat{\mathbf{s}}^\dagger|\zeta\rangle}\,. \tag{6.2}$$

Here, ζ is the detection angle of a balanced homodyne detector (BHD) which detects the output quadrature $\hat{o}_\zeta = \hat{o}_1 \cos\zeta + \hat{o}_2 \sin\zeta$, and $|\zeta\rangle = (\cos\zeta, \sin\zeta)^T$.

The matrix transformations which are necessary to implement the entangled readout scheme are summarized in the block diagram of Fig. 6.2. It starts with the creation of a bipartite entangled state from two squeezed beams. The initial squeezed states with squeezing parameter r are rotated by θ and $\theta + \pi/2$, respectively, before they are overlapped at a 50:50 beam splitter. One mode of the entangled state, the meter mode, is then sent into the interferometer, where it is subjected to the interferometer's noise transfer function $\mathbf{T}$. The reference beam is rotated by a frequency-independent angle of ϕ to partly compensate for the (frequency-dependent) rotation of the meter state. After recombining both beams at the final 50:50 beam splitter, two BHDs detect each of the two output modes. Their local oscillator phases are set to ζ and $\zeta + \frac{\pi}{2}$, respectively, such that they observe two orthogonal quadratures. Both BHD outputs are combined electronically, whereby the signal adds coherently, while the noise adds incoherently.

We obtain a new noise transfer function $\mathbf{T}'$ and signal transfer function $\hat{\mathbf{s}}'$, which are related to the initial functions by

$$\hat{s}' = \frac{1}{\sqrt{2}}\hat{s}\,, \tag{6.3}$$

$$\mathbf{T}' = \mathbf{BS} \times \left(\mathbf{T} \oplus \mathbf{R}(\phi)\mathrm{e}^{-\mathrm{i}\phi}\right) \times \mathbf{BS} \times \mathbf{SQZ}\,. \tag{6.4}$$

The interferometer's signal stays unaffected except for a factor of $1/\sqrt{2}$, which is due to the last beam splitter that divides the signal between the two BHDs. The new transfer matrix $\mathbf{T}'$ is obtained via the block transformations from Fig. 6.2. **SQZ** represents the initial squeezing preparation,

$$\mathbf{SQZ} = \left(\mathbf{R}(\theta)\mathbf{S}(-r)\right) \oplus \left(\mathbf{R}(\theta + \tfrac{\pi}{2})\mathbf{S}(+r)\right). \tag{6.5}$$

To calculate the noise spectral density, Eq. (6.2) has to be modified slightly to account for the now four-dimensional transfer matrix $\mathbf{T}'$. Let us first treat the nominator and denominator separately for the two homodyne detectors A and B:

$$N_A(\Omega) = \left(\langle\zeta| \otimes \langle 0|\right)\mathbf{T}'\mathbf{T}'^{\dagger}\left(|\zeta\rangle \otimes |0\rangle\right), \tag{6.6}$$

$$N_B(\Omega) = \left(\langle 0| \otimes \langle\zeta + \tfrac{\pi}{2}|\right)\mathbf{T}'\mathbf{T}'^{\dagger}\left(|0\rangle \otimes |\zeta + \tfrac{\pi}{2}\rangle\right), \tag{6.7}$$

$$D_A(\Omega) = \langle\zeta|\hat{s}'\hat{s}'^{\dagger}|\zeta\rangle\,, \tag{6.8}$$

$$D_B(\Omega) = \langle\zeta + \tfrac{\pi}{2}|\hat{s}'\hat{s}'^{\dagger}|\zeta + \tfrac{\pi}{2}\rangle\,. \tag{6.9}$$

From these expressions we can obtain the linear noise spectral density (LSD) of the combined homodyne detector output,

$$\mathrm{LSD}(\Omega) = \frac{\sqrt{N_A(\Omega) + N_B(\Omega)}}{\sqrt{D_A(\Omega)} + \sqrt{D_B(\Omega)}}\,. \tag{6.10}$$

▸ 6.3 *Simulation results*

Using the above theoretical description, the performance of an interferometer with detuned signal-recycling and entangled light enhanced readout was simulated with a Python script (see Sec. A.4.4).

Let us first look at the behaviour of quantum noise reflected at a detuned cavity, shown in Fig. 6.3. In this case, a cavity length of 1 m was assumed and the cavity was detuned from the laser carrier frequency by 5.5 MHz. The dashed black line shows the vacuum noise level, normalized to unity, which is independent of the sideband frequency. Reflecting a (pure) single-mode squeezed state with 10 dB noise suppression off this cavity results in the blue curve. Here, the initial rotation of the squeezing ellipse was chosen such that on resonance a squeezed variance of 1/10 is achieved. Off-resonance, the squeezing ellipse is rotated by 90°, resulting in full anti-squeezed noise with a variance of ≈ 10. The orange curve results from

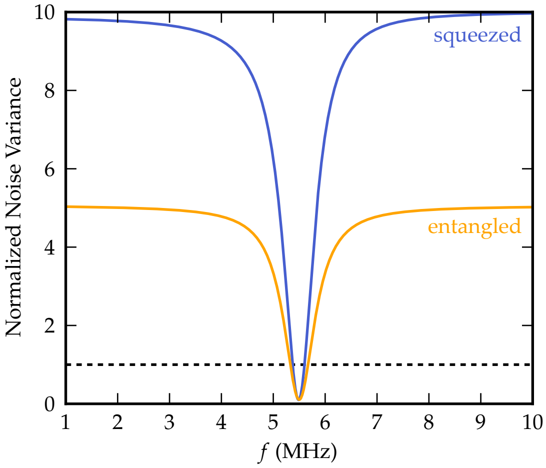

Figure 6.3: Squeezed and entangled quantum noise reflected at a detuned cavity. The noise variance is normalized to the vacuum noise (black dashed line). Both curves provide the same minimum noise variance at the cavity resonance. However, the entangled readout has only about half the off-resonance noise, compared to full anti-squeezed noise in squeezed light readout.

entangled light enhanced readout using a single detector and a 10 dB two-mode squeezed state. Here, the rotation of the entangled meter mode was chosen as in the squeezed light case. The reference mode was then rotated and phase-shifted such that perfect recombination occurred on resonance. Thus, a noise variance of a factor of 10 below the vacuum noise is obtained for entangled readout as well. Far off resonance, the meter state is rotated by 90°, compared to the reference mode. A recombination of the two modes thus results in uncorrelated noise, which is only about half the anti-squeezed noise: the noise of a thermal state with a variance of $(10 + 0.1)/2 = 5.05$. Thus, while the on-resonance quantum-noise is the same for squeezed and entangled light enhanced readout, roughly 3 dB SNR can be gained for entangled light enhanced readout at off-resonance frequencies.

The resulting sensitivity of entangled light enhanced readout for an ideal, GEO600-style interferometer is shown in Fig. 6.4. To be able to compare the results with the simulations in [HCC$^+$03], their interferometer and signal-recycling parameters were adopted, although they do not represent the current GEO600 (GEO-HF) configuration. Tab. 6.1 summarizes these parameters.

Individually, the sensitivities at the two output homodyne detectors are given by the dashed green curves. Compared to the squeezed-light readout curves from Fig. 6.1, the curves show a similar off-resonance sensitivity in both quadratures. This is due to only half the quantum noise in the entangled readout case, which in turn is approximately cancelled by the division of the signal towards the two detectors. At the resonance, the quantum noise is the same for entangled and squeezed readout. Thus, the split signal reduces the entangled readout sensitivity at each detector. Coherently combining the output of the two detectors then leads to the blue curve. Again it achieves the squeezed readout sensitivity at resonance,

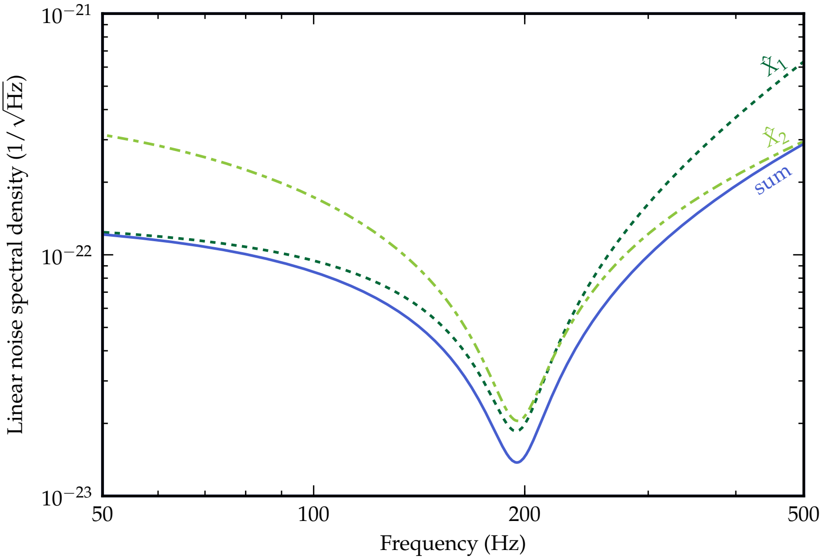

Figure 6.4: Simulation of an entangled-light enhanced readout of two orthogonal quadratures in a GEO 600-like interferometer with detuned signal recycling. The initial squeezing ellipses were oriented such that maximum sensitivity occurred on the signal recycling resonance. While each detector sees only half the signal, a coherent recombination (solid line) yields again the same sensitivity at resonance as in the squeezed-input case.

Table 6.1: Simulation parameters for the entangled readout of a GEO600-type interferometer with detuned signal recycling. The interferometer and signal-recycling parameters are taken from [HCC+03].

Symbol	Physical meaning	Numerical value
m	Mirror mass	$\infty^\dagger$
L	Effective arm length	1200 m
P	Circulating light power	10 kW
λ	Laser wavelength	1064 nm
R_{SR}	SR mirror power reflectivity	99%
ϕ_{SR}	SR cavity detuning	0.0055 rad
ζ	BHD detection angle	−0.11 rad
ϕ	Recombination angle	2.03 rad
r	Squeezing parameter	$1.15 \mathrel{\hat{=}} 10\,\mathrm{dB}$

† radiation pressure noise is neglected and shows an overall superior performance in the off-resonance regime, compared to either of the two squeezed curves in Fig. 6.1.

In conclusion, it was shown in this thesis that the (frequency independent) entangled light enhanced readout of detuned signal-recycled gravitational wave detectors achieves a peak sensitivity that is comparable to frequency-independent squeezed-light enhanced readout, but at the same time provides a better broadband noise performance. No filter cavity is assumed in this scheme to cancel the frequency-dependent sideband rotation due to the detuned signal-recycling cavity. Using a single filter cavity would also be possible with entangled light enhanced readout. In this case, the different signal transfer function for the $\hat{X}_1$ and $\hat{X}_2$ quadrature could again be exploited, for example, to optimize the high-frequency response. In a fully optimized, squeezed-variational readout scheme [KLM$^+$01], the best squeezing and readout quadrature is already chosen at each sideband frequency and the entangled-light enhanced scheme proposed provides no advantage. Instead, the entangled-light resources are then again available, e.g. for stray-light detection in the context of quantum-dense metrology, see Sec. 5.

References

[AVirgo] The Virgo Collaboration. *Advanced Virgo Baseline Design*. Tech. rep. VIR-027A-09. 2009.

[BC01] A. Buonanno and Y. Chen. "Quantum noise in second generation, signal-recycled laser interferometric gravitational-wave detectors". *Physical Review D* 64 (2001), 042006. DOI: `10.1103/PhysRevD.64.042006`.

[CDR+98] V. Chickarmane, S. Dhurandhar, T. Ralph, M. Gray, H.-A. Bachor, and D. McClelland. "Squeezed light in a frontal-phase-modulated signal-recycled interferometer". *Physical Review A* 57 (1998), 3898–3912. DOI: `10.1103/PhysRevA.57.3898`.

[EBH+13] M. Evans, L. Barsotti, J. Harms, P. Kwee, and H. Miao. "Realistic Filter Cavities for Advanced Gravitational Wave Detectors". LIGO-P1300054-v3. 2013.

[Har02] J. Harms. "Quantum Noise in the Laser-Interferometer Gravitational-Wave Detector GEO600". Diplomarbeit. Universität Hannover, 2002.

[Har10] G. M. Harry. "Advanced LIGO: the next generation of gravitational wave detectors". *Classical and Quantum Gravity* 27 (2010), 084006. DOI: `10.1088/0264-9381/27/8/084006`.

[HCC+03] J. Harms, Y. Chen, S. Chelkowski, A. Franzen, H. Vahlbruch, K. Danzmann, and R. Schnabel. "Squeezed-input, optical-spring, signal-recycled gravitational-wave detectors". *Physical Review D* 68 (2003), 42001. DOI: `10.1103/PhysRevD.68.042001`.

[HSM+98] G. Heinzel, K. Strain, J. Mizuno, K. Skeldon, B. Willke, W. Winkler, R. Schilling, A. Rüdiger, and K. Danzmann. "Experimental Demonstration of a Suspended Dual Recycling Interferometer for Gravitational Wave Detection". *Physical Review Letters* 81 (1998), 5493–5496. DOI: `10.1103/PhysRevLett.81.5493`.

[KLM+01] H. J. Kimble, Y. Levin, A. B. Matsko, K. S. Thorne, and S. P. Vyatchanin. "Conversion of conventional gravitational-wave interferometers into quantum nondemolition interferometers by modifying their input and/or output optics". *Physical Review D* 65 (2001), 22002. DOI: `10.1103/PhysRevD.65.022002`.

[Mee88] B. J. Meers. "Recycling in laser-interferometric gravitational-wave detectors". *Physical Review D* 38 (1988), 2317–2326. DOI: `10.1103/PhysRevD.38.2317`.

[SHS+04] R. Schnabel, J. Harms, K. a. Strain, and K. Danzmann. “Squeezed light for the interferometric detection of high-frequency gravitational waves”. *Classical and Quantum Gravity* 21 (2004), S1045–S1051. DOI: `10.1088/0264-9381/21/5/099`.

[TGV+09] A. Thüring, C. Gräf, H. Vahlbruch, M. Mehmet, K. Danzmann, and R. Schnabel. “Broadband squeezing of quantum noise in a Michelson interferometer with Twin-Signal-Recycling”. *Optics Letters* 34 (2009), 824–826. DOI: `10.1364/OL.34.000824`.

[TSL+07] A. Thüring, R. Schnabel, H. Lück, and K. Danzmann. “Detuned Twin-Signal-Recycling for ultrahigh-precision interferometers”. *Optics Letters* 32 (2007), 985–987. DOI: `10.1364/OL.32.000985`.

[VCH+05] H. Vahlbruch, S. Chelkowski, B. Hage, A. Franzen, K. Danzmann, and R. Schnabel. “Demonstration of a squeezed-light-enhanced power- and signal-recycled Michelson interferometer”. *Physical Review Letters* 95 (2005), 1–4. DOI: `10.1103/PhysRevLett.95.211102`.

[WAA+02] B. Willke, P. Aufmuth, C. Aulbert, S. Babak, R. Balasubramanian, B. W. Barr, S. Berukoff, S. Bose, G. Cagnoli, M. M. Casey, et al. “The GEO 600 gravitational wave detector”. *Classical and Quantum Gravity* 19 (2002), 1377–1387. DOI: `10.1088/0264-9381/19/7/321`.

▶ Chapter 7

Summary and conclusion

Quantum metrology has become a vital ingredient for the design of interferometric gravitational wave detectors, as they are limited by quantum noise over almost the complete detection band. Previously, classical noise sources such as suspension and mirror thermal noise covered most of the frequency range, leaving only the high-frequency quantum noise, i.e. shot noise. Starting with the next generation of gravitational wave detectors, radiation pressure noise will become visible. Thus, the full dynamics of quantum back-action will become important, finally putting to test a lot of theoretical work which goes back as long as to the 60s of the last century. Already today, the continuously running squeezed light source in GEO 600 shows that the tools for shaping the quantum noise are ready for the challenge. In this thesis, I introduced and demonstrated new applications of quantum metrology for gravitational wave detectors.

In a table-top setup, a squeezed-light enhanced, zero area Sagnac interferometer was demonstrated. The Sagnac interferometer topology has recently attracted a lot of attention, since it has been shown to be a quantum non-demolition device. Measuring the speed of the test masses instead of their position makes the Sagnac interferometer virtually unaffected by quantum back-action noise. To remove the rotational sensitivity of this topology, a zero-area configuration has to be adopted. Here I showed that squeezed light readout is compatible with the Sagnac topology, and a noise reduction by more than 8 dB was measured. As of today, it remains the strongest nonclassical sensitivity improvement of an interferometer with continuous-wave squeezed light.

Furthermore, this thesis introduced the first application of two-mode squeezed, entangled states for improving the sensitivity of gravitational wave detectors. It is embedded into the concept of quantum-dense metrology (QDM), a novel technique for reading out two independent physical quantities which are encoded in two non-commuting observables of the meter state. In the course of this thesis, the concept of QDM has been brought to a solid theoretical foundation and a first demonstration. Stray light in gravitational wave detectors leads to the well-known problem of parasitic interferences, wherein scattered and frequency-shifted photons introduce additional disturbance signals in the detection band. These parasitic interferences appear in the output field with an arbitrary quadrature orientation. This orientation can be determined with QDM, which allows for a simultaneous, squeezed readout of both quadratures at the output. Thus, parasitic interferences can be identified and excluded from further data analysis. In a table-top interferometer, I was able to simulate such interferences with the help of an end-mirror cavity. I demonstrated a simultaneous readout of two output quadratures with 6 dB nonclassical noise suppression in both quadratures. A science signal and a parasitic signal were clearly distinguished, showing that QDM can nonclassically improve the sensitivity of gravitational wave detectors even when the limiting noise sources are not of quantum nature. Applying this readout scheme to large scale gravitational wave detectors is relatively straight forward, since the required low-frequency squeezed states and control techniques are already routinely employed, e.g. in the GEO 600 squeezed light source.

This thesis shows how two-mode squeezing can also be used for the readout of gravitational wave detectors with detuned signal recycling. Injecting squeezed states of light into an interferometer with detuned signal recycling leads to a frequency-dependent rotation of the squeezing ellipse around the signal-recycling resonance. This rotation in turn leads to a significant loss of sensitivity at off-resonance frequencies and can only be cancelled via a sophisticated filter cavity. I performed several simulations which showed that an entangled, simultaneous readout of two orthogonal quadratures yields a significantly better sensitivity than squeezed light readout, when no filter cavity is used.

The scientific results from this thesis contribute to the great variety of experiments which probe the ultimate limits on measurement sensitivity at the frontier of quantum-mechanical interactions between light and matter. Interferometric gravitational wave detectors will be at the very center of this effort, hopefully culminating in the first direct detection of gravitational waves, one century after Einstein predicted them.

▸ Chapter A

Appendix

▸ A.1 *Matrix formalism for the reflectivity of cavities and multi-layer stacks*

The ray-transfer matrix formalism provides a very handy tool to calculate the reflectivity of a series of reflecting boundaries. This of course includes reflection on a single boundary between media of different refractive indices, such as Fresnel reflection on a piece of glass. However, it is also very simple to calculate the reflection of two such interfaces, i.e. a Fabry-Perot resonator, or even dichroic mirror stacks with a multitude of layers having different thicknesses, indices of refraction and angles of incidence.

The following formulas mainly follow the treatment in the lectures of B. Sernelius [Ser13], especially lecture 13. Let us look at a boundary between two media, labelled N and $N+1$, with refractive indices n_N and n_{N+1}, see Fig. A.1. Snell's law tells us the relationship between the angles of incidence,

$$n_N \sin \alpha_N = n_{N+1} \sin \alpha_{N+1} \,. \tag{A.1}$$

The amplitude reflection of such a boundary for p-polarized and s-polarized light,

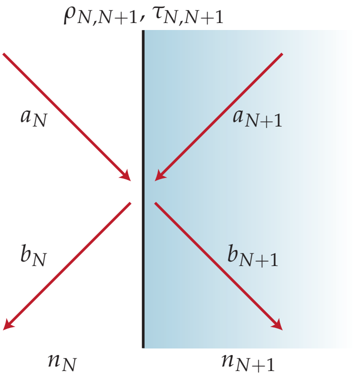

Figure A.1: Reflection at a boundary between two media with different refractive indices.

ρ^p and ρ^s, is given by Fresnel's formulas,

$$\rho^p_{N,N+1} = \frac{n_{N+1}\cos\alpha_N - n_N\cos\alpha_{N+1}}{n_{N+1}\cos\alpha_N + n_N\cos\alpha_{N+1}}\,, \tag{A.2}$$

$$\rho^s_{N,N+1} = \frac{n_N\cos\alpha_N - n_{N+1}\cos\alpha_{N+1}}{n_N\cos\alpha_N + n_{N+1}\cos\alpha_{N+1}}\,. \tag{A.3}$$

For normal incidence, $\alpha = 0$, the difference in reflection for p- and s-polarized light vanishes (except for the sign) and the formulas are reduced to

$$\rho^p = -\rho^s = \frac{n_{N+1} - n_N}{n_{N+1} + n_N}\,. \tag{A.4}$$

Introducing the amplitude transmission $\tau = \sqrt{1-\rho^2}$, we can immediately deduce from Fig. A.1 that the incoming and outgoing beams are related by

$$\begin{pmatrix} b_N \\ b_{N+1} \end{pmatrix} = \begin{pmatrix} \rho_{N,N+1} & \tau_{N,N+1} \\ \tau_{N,N+1} & -\rho_{N,N+1} \end{pmatrix} \begin{pmatrix} a_N \\ a_{N+1} \end{pmatrix}\,, \tag{A.5}$$

where we introduced a minus sign as usual because of energy conservation [Bur10]. However, we would like to have an equation which relates the beams inside medium N to the beams inside medium $N+1$. We thus rearrange the equation to get

$$\begin{pmatrix} a_N \\ b_N \end{pmatrix} = \frac{1}{\tau_{N,N+1}} \begin{pmatrix} 1 & \rho_{N,N+1} \\ \rho_{N,N+1} & 1 \end{pmatrix} \begin{pmatrix} a_{N+1} \\ b_{N+1} \end{pmatrix} = \mathbf{M}_{N,N+1} \begin{pmatrix} a_{N+1} \\ b_{N+1} \end{pmatrix}\,. \tag{A.6}$$

Travelling through a layer with index of refraction n at an angle α adds an additional phase shift of e^{ikd}, where d is the thickness of the layer, and k is the component of the wave vector orthogonal to the layer surfaces, $k = 2\pi n\cos(\alpha)/\lambda$. This phase shift can be implemented with the matrix relation

$$\begin{pmatrix} a'_N \\ b'_N \end{pmatrix} = \begin{pmatrix} \mathrm{e}^{-ikd} & 1 \\ 1 & \mathrm{e}^{+ikd} \end{pmatrix} \begin{pmatrix} a_N \\ b_N \end{pmatrix} = \mathbf{D}_N \begin{pmatrix} a_N \\ b_N \end{pmatrix}\,. \tag{A.7}$$

We finally arrive at the complete ray-transfer matrix for a stack of N layers,

$$\begin{pmatrix} a_0 \\ b_0 \end{pmatrix} = \mathbf{M}_{0,1}\mathbf{D}_1 \times \mathbf{M}_{1,2}\mathbf{D}_2 \times \cdots \times \mathbf{M}_{N-1,N}\mathbf{D}_N \times M_{N+1} \begin{pmatrix} a_{N+1} \\ b_{N+1} \end{pmatrix} \tag{A.8}$$

$$= \mathbf{T} \begin{pmatrix} a_{N+1} \\ b_{N+1} \end{pmatrix}\,. \tag{A.9}$$

Here the first matrix $\mathbf{M}_{0,1}$ describes the boundary between air and the first layer, and layer $N+1$ is either the substrate or again air, both of which can be treated as semi-infinite and thus there is no associated phase-shift matrix. Looking again at the definition of the matrix $\mathbf{M}$, we see that the reflectivity of a transfer matrix can simply be obtained from the quotient of the entries $(2,1)$ and $(1,1)$, thus $\rho = T_{21}/T_{11}$.

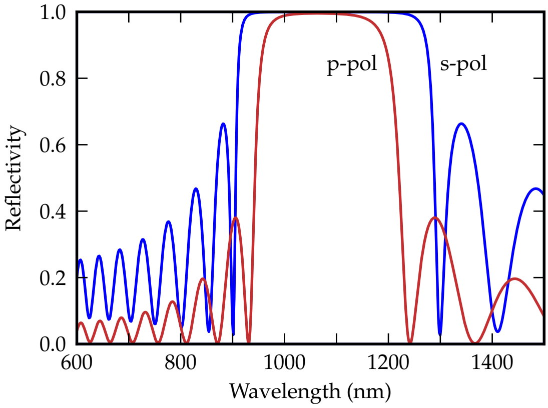

Figure A.2: Simulation of the wavelength-dependent reflectivity of a dichroic HR mirror coating for a design wavelength of 1064 nm at an angle of incidence of 45°.

As an example, let us look at a basic Fabry-Perot resonator in air, consisting of a coated substrate with reflectivities ρ_1 and ρ_2 on the two sides. The corresponding transmissivities, in the lossless case, are given by $\tau_{1,2} = \left(1 - \rho_{1,2}^2\right)^{1/2}$. Then we have

$$\mathbf{T}^{\mathrm{FP}} = \frac{1}{\tau_1 \tau_2} \begin{pmatrix} 1 & \rho_1 \\ \rho_1 & 1 \end{pmatrix} \begin{pmatrix} \mathrm{e}^{-\mathrm{i}\delta} & 0 \\ 0 & \mathrm{e}^{\mathrm{i}\delta} \end{pmatrix} \begin{pmatrix} 1 & \rho_2 \\ \rho_2 & 1 \end{pmatrix}, \tag{A.10}$$

where δ is related to the thickness of the substrate, as above, and can be thought of as a small detuning from resonance. The amplitude reflection of the Fabry-Perot then reads

$$\rho = T_{21}^{\mathrm{FP}} / T_{11}^{\mathrm{FP}} = \frac{\rho_1 + \rho_2 \mathrm{e}^{2\mathrm{i}\delta}}{1 + \rho_1 \rho_2 \mathrm{e}^{2\mathrm{i}\delta}}, \tag{A.11}$$

which is the well-known textbook formula for such a resonator.

Calculating the reflectivity of a multi-layer dichroic mirror stack is equally straight forward. Given the refractive indices of the used coating materials, e.g. SiO_2 and Ta_2O_5, Eq. (A.1) determines the angles of incidence at each layer boundary. The reflectivities at the layer boundaries can then be obtained from Equations (A.2) and (A.3). Fig. A.2 shows the simulated intensity reflectivity of a simple HR coating design for 1064 nm at an angle of incidence of 45°, and for s- and p-polarized light. It consists of ten SiO_2-Ta_2O_5 double-layers on a fused silica substrate. The wavelength is varied from 600 nm to 1500 nm, clearly showing an oscillatory reflectivity. For s-polarized light, the wavelength range with a high reflectivity is significantly broader than for p-polarized light. This also leads to generally higher reflectivities for s-polarized light at the design wavelength.

▸ A.2 *Practical impedance-matching*

Just as a mismatch in refractive index leads to reflection of a light field at a boundary between different media, an electro-magnetic wave travelling inside a cable or electric circuit also experiences reflection when the impedance Z is mismatched. The (complex) reflection coefficient is obtained analogous to the calculation for optics, compare Eq. (A.4),

$$\Gamma = \frac{Z_L - Z_S}{Z_L + Z_S} = |\Gamma| \mathrm{e}^{\mathrm{i}\phi} \,, \tag{A.12}$$

where Z_L and Z_S are usually called the source and load impedance. Closely connected is the *voltage standing-wave ratio*, VSWR,

$$\mathrm{VSWR} = \frac{1 + |\Gamma|}{1 - |\Gamma|} \geq 1 \,, \tag{A.13}$$

which also already gives a hint at what happens when there is impedance mismatch in a given circuit. A standing wave develops, whose ratio between the maximum and minimum intensity is given by the VSWR. Standing waves are considered a *bad thing* in electronic circuitries, especially inside cables, since these cables then turn into antennas and radiate at the standing-wave frequency. In addition, even the slightest bending and twisting of a cable changes the phase of the standing wave, immediately leading to problems with pick-up signals and offset fluctuations. Thus, the VSWR should always be kept as close to unity as possible, at least when radio-frequency signals are transmitted over a length of cable that is in the order of magnitude of the signal's wavelength. In such applications, the source impedance is usually known and is commonly set to 50 Ω (at least in radio-frequency and microwave engineering; video transmissions use 75 Ω). The question now is, how to find out the load impedance and how to match the two?

Let us introduce a useful tool for displaying and working with impedances, the Smith chart. The Smith chart provides a direct mapping between a polar representation of the reflection coefficient Γ and the accompanying load impedance Z_L. Fig. A.3 shows this connection. Three points are of special significance. For $Z_L = Z_S$, $\Gamma = 0$, which is the central point of the diagram. A short circuit, $Z_L = 0$ leads to $\Gamma = -1$, all power is reflected back to the source. For $Z_L = \infty$, we again obtain total reflection, but with opposite sign, $\Gamma = 1$. These three cases, usually called *load*, *short*, and *open*, are also used to calibrate a reflection coefficient measurement. The impedance can be written as a combination of real and imaginary part, $Z_L = R_L + \mathrm{i}X_L$, which are also called the resistance and reactance. A Smith chart displays lines of constant resistance, as well as lines of constant reactance, on top of a polar plot of the reflection coefficient. It is, as we will see below, helpful to do the same for the admittance, which is the inverse impedance, and its real and

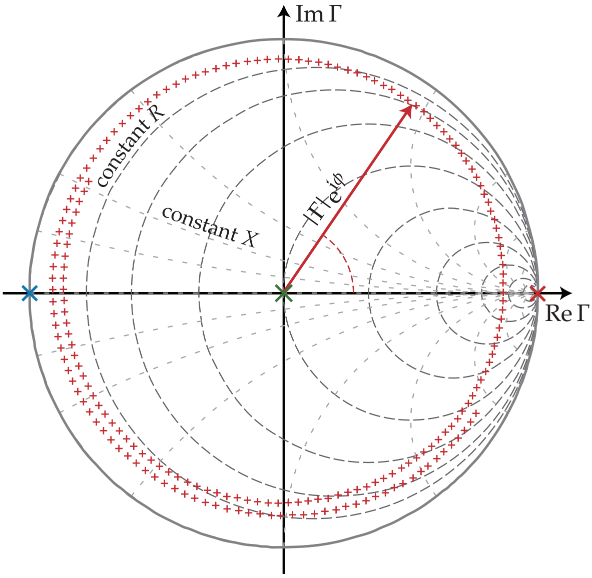

Figure A.3: Smith chart showing the connection between a polar representation of the reflection coefficient Γ and the load impedance. The reflection coefficient can assume all values within the unit circle. For a known source impedance, each of these points is associated with a specific load impedance, given by the resistance R and the reactance X. Shown in red is an actual measurement of an unmatched cable, for a range of frequencies. The points used for calibration are marked in green (matched impedance), red (open circuit) and blue (short circuit).

imaginary parts, $Y_L = 1/Z_L = G_L + \mathrm{i}B_L$. G and B go by the names of conductance and susceptance.

Common network analyzers are capable of measuring the reflection of a *device under test* (DUT), usually with some kind of toolkit which actually measures the full S parameters. An example setup from the AEI's electronics workshop is shown in Fig. A.4. DUTs with two ports can be described by a 2×2 S parameter matrix with frequency-dependent, complex entries that relate the ingoing to the outgoing fields, see Fig. A.5,

$$\begin{pmatrix} \mathrm{Out}_1 \\ \mathrm{Out}_2 \end{pmatrix} = \begin{pmatrix} S_{11} & S_{12} \\ S_{21} & S_{22} \end{pmatrix} \begin{pmatrix} \mathrm{In}_1 \\ \mathrm{In}_2 \end{pmatrix} . \tag{A.14}$$

In this representation, S_{11} is the sought-after reflection coefficient, while S_{21} is the transfer function of the device from input 1 to output 2. Usually, network analyzers can automatically convert the measured reflection coefficient into impedance or admittance values. As can be seen in Fig. A.4, some analyzers even support a Smith chart representation on their displays. For a correct conversion, the analyzers need to be calibrated before each measurement, which is done by three impedance calibration standards for the short, open and load ($50\,\Omega$) conditions.

Now that we can measure the load impedance, we need to match it to the source impedance. For this, we can connect various passive components in parallel or series to the load. In a series circuit, impedances add up, such that we obtain a new impedance $Z_s = Z_L + Z_c$, where Z_c is the impedance of the added component.

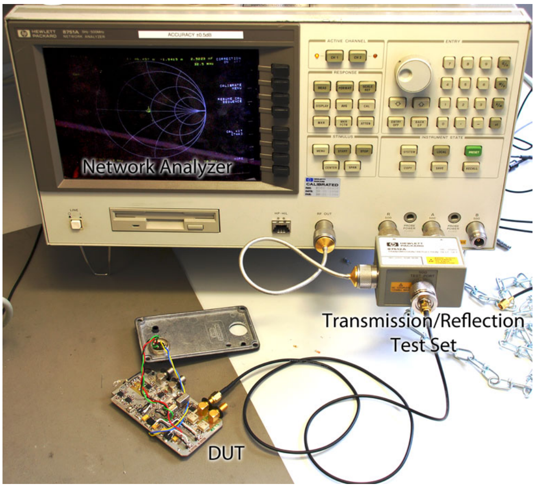

Figure A.4: Example setup for the measurement of the reflection coefficient, using a Hewlett Packard HP8751A network analyzer, together with an HP87512A transmission/reflection test set.

For a parallel circuit, however, the admittances add, $Y_p = Y_L + Y_1$. The three basic passive components with which we can modify the load impedance are the resistor, the capacitor, and the inductor. For ideal components they possess the impedances

$$Z_R = R\,, \tag{A.15}$$

$$Z_C = -\frac{\mathrm{i}}{\omega C}\,, \tag{A.16}$$

$$Z_L = \mathrm{i}\omega L\,, \tag{A.17}$$

where R, C and L are the resistance, capacity and inductance, respectively. Thus, resistors change the real part of the impedance or admittance, while capacitors and inductors act on the imaginary part only. Fig. A.6 shows the effect of adding each component in series in the Smith impedance chart representation, and in parallel in the admittance chart representation. Generally, resistors should be avoided for matching purposes as they introduce loss to the signal. In the 10 MHz to 200 MHz regime, a combination of a capacitor and an inductor, both stock SMD components, solved all impedance matching problems that I have encountered so far. Depending on the starting point in the Smith chart related to the origin, the components have

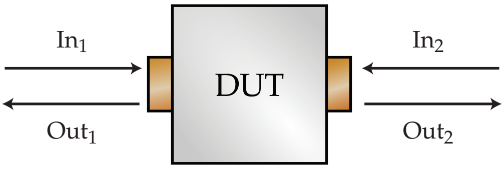

Figure A.5: Definition of the input- and output fields for a two-port device.

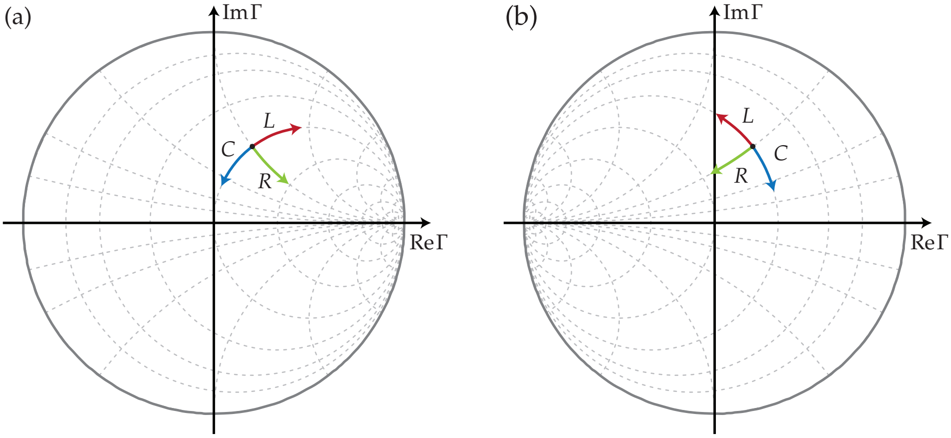

Figure A.6: Effect of adding passive components to the load. (a) shows the Smith chart for adding a series impedance. A series *R* increases the total resistance, moving the point closer to the open-load case, on a line of constant reactance. Adding a series *L* or *C* moves on a line of constant resistance, away from or towards the real axis. (b) shows the admittance chart for adding a parallel impedance. In this case, a parallel *R* reduces the total resistance, moving closer to the short-circuit point, on a line of constant susceptance. A parallel *L* or *C* move along a line of constant conductance. With a combination of transformations (a) and (b), any point in the Smith chart can be brought to the origin, i.e. to the impedance-matched case.

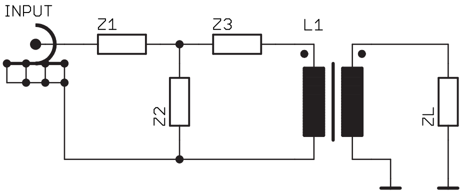

Figure A.7: Schematic for an impedance matching circuit in a local oscillator input section. `ZL` is the load impedance of the actual circuit, which is galvanically isolated from the input by transformer `L1`. `Z1`–`Z3` are populated with a combination of capacitors and inductors to match `ZL` to the 50 Ω input (see text).

to be added in a different combination of series and parallel, in addition to inductor first or capacitor first. To make room for all options, a circuit design as shown in Fig. A.7 can be used, where either Z_1 and Z_2 or Z_2 and Z_3 are populated, with the remaining position bridged with a jumper. For finding the right component values and arrangement, several computer programs exist (e.g. SMITH by F. Dellsperger [Del13]) which take the measured load impedance and then visualize the effect of adding series and parallel components. Note that there are generally two solutions for transforming a given load impedance to the origin of the Smith chart, i.e. to the impedance-matched case. They differ in the components order, e.g. parallel inductor followed by series capacitor, vs. parallel capacitor followed by series inductor. Both solutions can be used, often a choice being made by available components. However, the solution with series capacitor has a high impedance towards DC, which might or might not be beneficial.

Since the impedance of capacitors and inductors depends on frequency, a simple matching network can usually only be found for a single frequency. This is however sufficient for pretty much all circuits in our labs, since high-frequency circuitry is either contained on a single board or deals with the transmission of local oscillators. In the first case, the traces are too short to necessitate impedance matching for this frequency range, while the second case is single frequency anyways and the above method applies. One should also keep in mind that there is a fourth component which can be helpful for impedance matching, a transformer. For an ideal transformer, the winding ratio determines the ratio between the impedances on the primary and secondary side. Especially in the low-MHz range, a transformer can help in cases where otherwise rather large inductances would be required.

▸ A.3 *Electronics*

During the experimental work leading to this thesis, several electronic circuits have been developed or modified. This section presents a selection of the most important or interesting designs, including the schematic drawings.

▸ A.3.1 *Mephisto temperature lock*

For locking the *Mephisto* laser to the monolithic squeezed light source, a wide-range temperature actuation was required. The circuit `tempservo_mephisto`, Fig. A.8, attaches to the low-frequency output of a Servo 4 controller and conditions the signal such that it can be fed into the temperature control input of the *Mephisto* laser. Protection diodes at the output confine the temperature range, such that the laser does not undergo excessive heating or cooling, should the control loop fall out of lock. The circuit schematic is given in Fig. A.13.

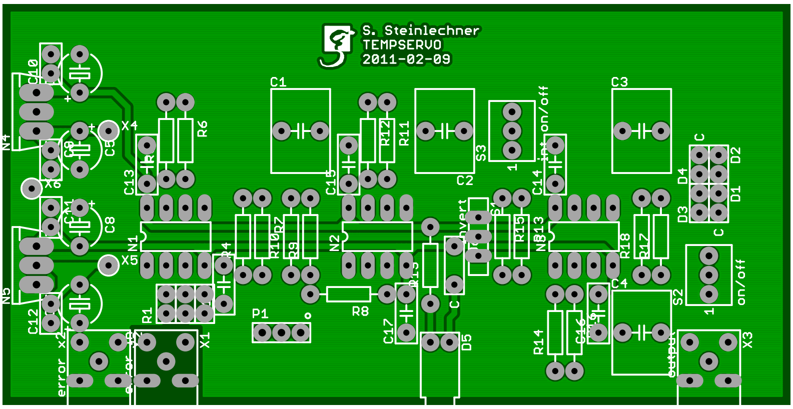

S. Steinlechner
TEMPSERVO
2011-02-09
C1
C2
C3
C4
C5
C6
C7
C8
C9
C10
C11
C12
C13
C14
C15
C16
C17
R1
R4
R6
R7
R8
R9
R10
R11
R12
R13
R14
R15
R17
R18
N1
N2
N3
N4
N5
S2
S3
P1
D1
D2
D3
D4
D5
X1
X2
X3
X4
X5
X6
on/off
int on/off
invert
error
output

Figure A.8: *Mephisto* laser temperature actuator for the MSQZ control beam lock

▸ A.3.2 *OPA-lock photo-detector*

Locking both the control beam and the pump phase at a squeezed light resonator requires a demodulation of the detected photo current with two different local oscillators, having a relative phase difference of 90°. The circuit `SqzLockPD_v1.2`, Fig. A.9, accomplishes this by a 90° power splitter in the local oscillator input, followed by two separate demodulation paths. The circuit schematic is given in Figs. A.14 – A.16.

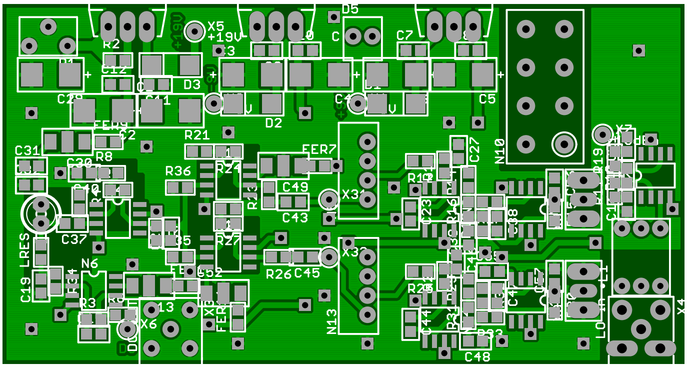
X5
+19V
R2
C12
D3
C29
C11
D5
C7
C5
D2
R21
FER7
C31
R8
C30
R36
R24
C49
X31
C43
R16
C23
C27
N10
C37
N6
LRES
C19
R3
X6
C35
C52
R27
R26
C45
X32
N13
C44
C48
X4

Figure A.9: SqzLockPD v1.2, used for locking the control beam and pump phase of the squeezed light resonators

▸ A.3.3 *AD9959 four-channel digital function generator*

This circuit, together with the `AD9959` evaluation board by Analog Devices, provides a four-channel digital frequency generator that can provide sine waveforms up to about 200 MHz. All settings are controlled via USB and will be remembered even if the power is lost. For each channel, frequency and phase can be set separately. Also, output power can be adjusted in 4 steps. An additional output amplifier circuit is available for each channel. The schematics for the USB interface are shown in Fig. A.17.

▸ A.3.4 *Small monitoring photo-detector*

`TinyPD`, Fig. A.10, is a DC monitoring photo-detector design with simplicity and quick assembly in mind. The housing is made from a rectangular aluminum profile, requiring little work from the mechanics workshop. The circuit can be easily removed from the housing with the mount still screwed to the optical table. After changes to the electronics, only minimal realignment of the optical beam is needed. The schematics are given in Fig. A.18.

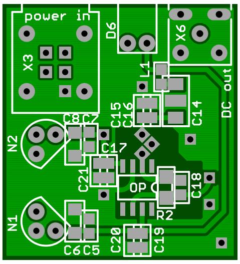
power in
X3
D6
X6
L1
C15
C16
C14
DC out
N2
C8
C7
C17
C21
OP
C18
R2
N1
C6
C5
C20
C19

Figure A.10: TinyPD, a small DC monitoring photo detector

▸ A.3.5 *Homodyne detector*

The homodyne detector circuits used in our experiments are originally designed by Henning Vahlbruch and were modified by Tobias Eberle and myself to provide additional locking signals. This version, `HomoV1.4` shown in Fig. A.11, can demodulate the detected signal at two different frequencies. Additionally, it provides a low-frequency, DC sum output. Note that the circuit schematic in Figs. A.19 – A.20 has a design flaw: the differential amplifiers `N16`, `N17` should be powered from a higher, ±9 V power supply, as they cannot operate with input voltages close to the rails.

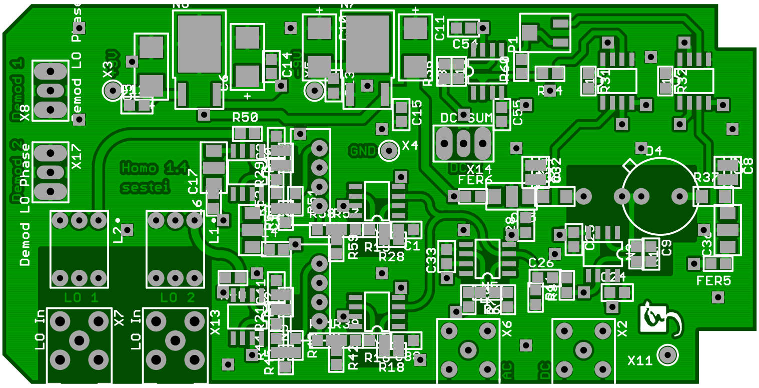
Demod 1
X8
Demod LO Phase
Demod 2
X17
Demod LO Phase
X3
R50
Homo 1.4
sestei
C17
L2
L1
LO 1
LO 2
LO In
X7
LO In
X13
C14
C15
GND
X4
DC SUM
C55
C11
C54
R40
R31
R32
X14
FER6
D4
R37
C8
C33
C26
C9
FER5
R28
R18
X6
X2
AC
DC
X11

Figure A.11: Homo V1.4, the circuit board for the balanced homodyne detectors

▸ A.3.6 *Servo*

In virtually all control loops of our experiments, a PID (proportional/ differentiating/integrating) controller, known as *Servo* in our lab jargon, is used. The original design and implementation of this controller was done by Henning Vahlbruch, and it was redesigned and improved by Tobias Eberle and myself. In its current iteration, Fig. A.12, the Servo now has most front panel controls and outputs directly mounted on the board, drastically reducing the amount of wiring that is required during assembly.

The Servo has a differential input stage with an optional offset. A linear gain stage follows, providing attenuation of up to $\times 1/50$ and amplification of up to $\times 50$. Two tunable-Q notch filters can be used to suppress resonances. Three universal integrator/differentiator blocks then shape the error signal as needed. A final second-order low-pass limits the control bandwidth. A low frequency stage provides a control signal for slow, wide-range thermal control via Peltier elements.

The integrated ramp generator produces a triangular waveform with an adjustable amplitude and frequency. The schematics are shown in Fig. A.21–A.24.

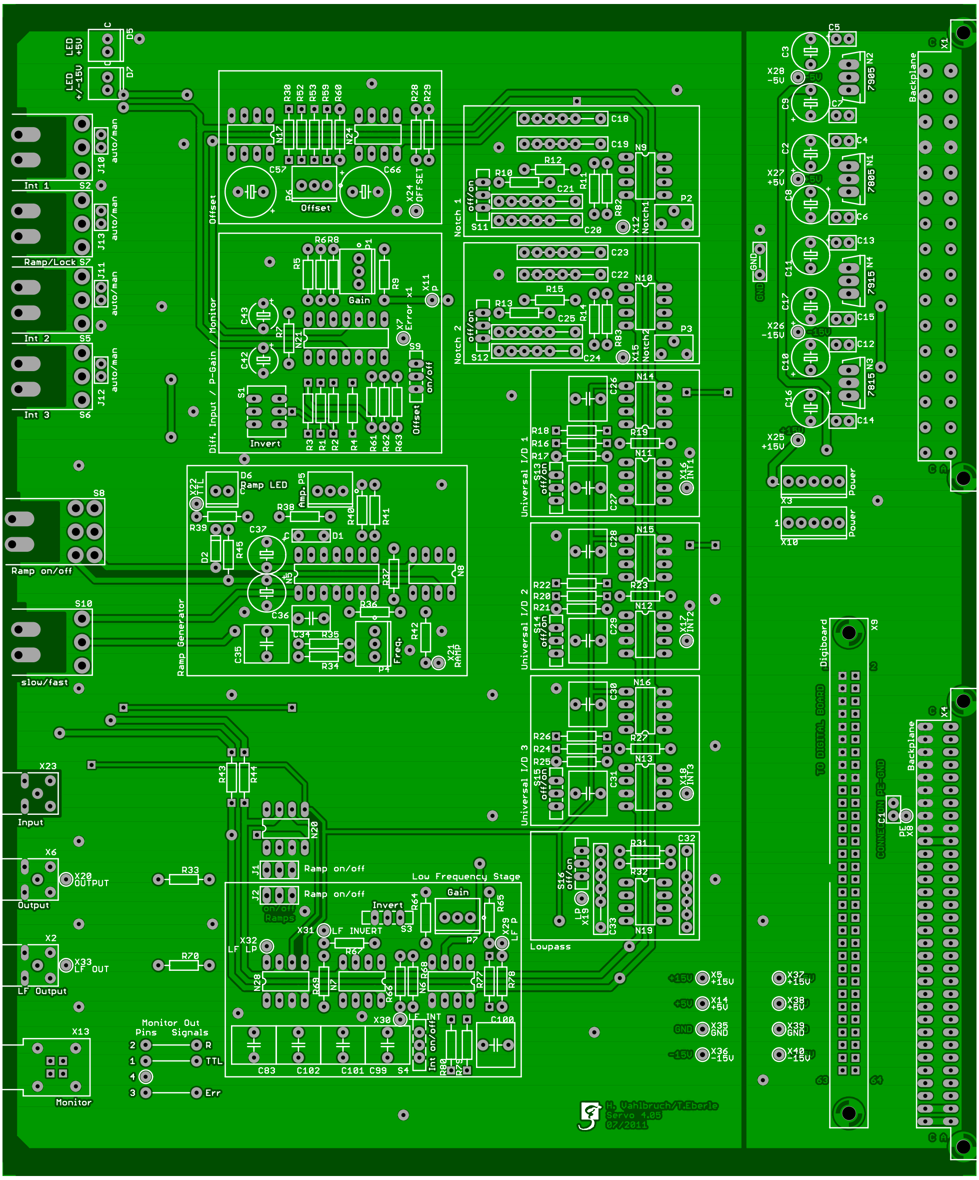
LED +5V
LED +/-15V
Int 1
Ramp/Lock
Int 2
Int 3
auto/man
Offset
Diff. Input / P-Gain / Monitor
Gain
Invert
Error
Notch 1
Notch 2
Universal I/O 1
Universal I/O 2
Universal I/O 3
Ramp Generator
Ramp LED
Freq.
Ramp on/off
slow/fast
Input
Output
LF Output
Monitor
Monitor Out
Pins Signals
Low Frequency Stage
Lowpass
Power
Backplane
Digiboard
TO DIGITAL BOARD
7905 N2
7805 N1
7915 N4
7815 N3
H. Vahlbruch/T.Eberle
Servo 4.05
07/2011

Figure A.12: Servo 4.04/4.05 circuit board preview, top layer

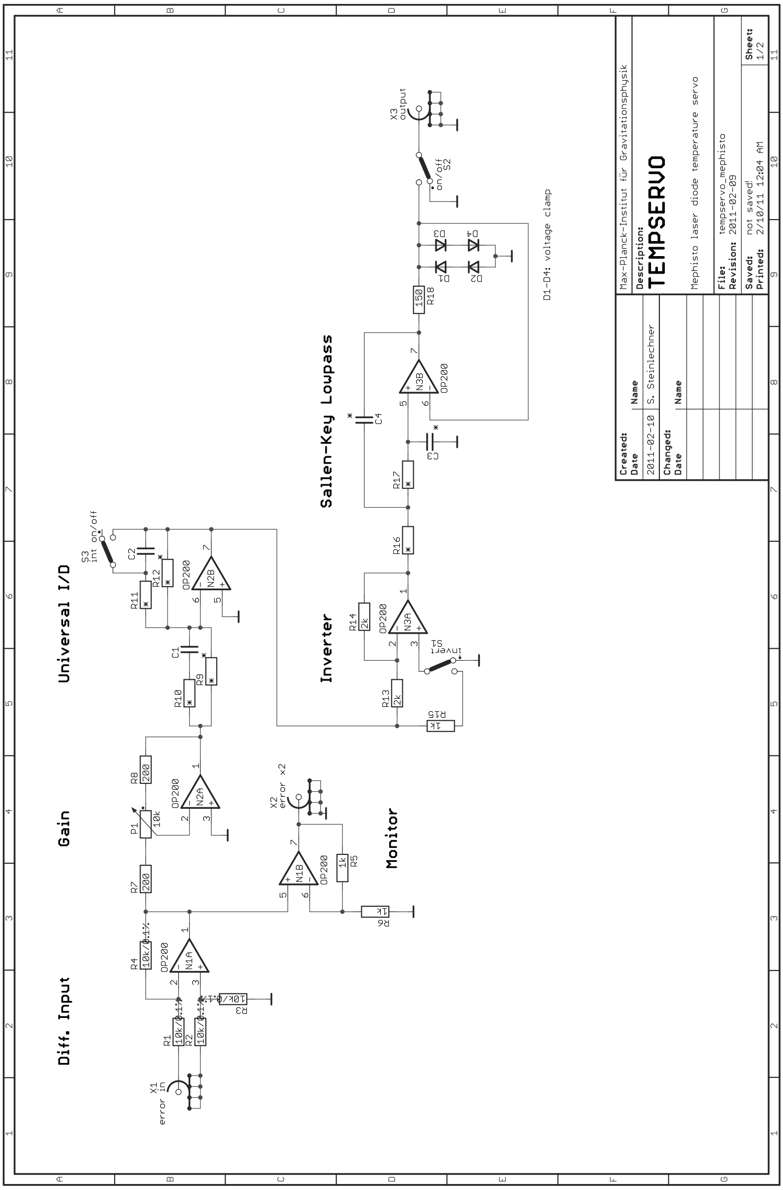
Diff. Input
Gain
Universal I/D
Inverter
Sallen-Key Lowpass
Monitor
X1 error in
R1 10k/0.1%
R2 10k/0.1%
R3 10k/0.1%
R4 10k/0.1%
N1A OP200
N1B OP200
R5 1k
R6 1k
X2 error x2
R7 200
P1 10k
R8 200
N2A OP200
R9
R10
C1
R11
R12
C2
S3 int on/off
N2B OP200
R13 2k
R14 2k
N3A OP200
S1 invert
R15 1k
R16
R17
C3
C4
N3B OP200
R18 150
D1
D2
D3
D4
D1-D4: voltage clamp
S2 on/off
X3 output
Max-Planck-Institut für Gravitationsphysik
Description:
TEMPSERVO
Mephisto laser diode temperature servo
Created:
Date
2011-02-10
Name
S. Steinlechner
Changed:
Date
Name
File: tempservo_mephisto
Revision: 2011-02-09
Saved: not saved!
Printed: 2/10/11 12:04 AM
Sheet: 1/2

Figure A.13: *Mephisto* laser temperature actuator, circuit schematic

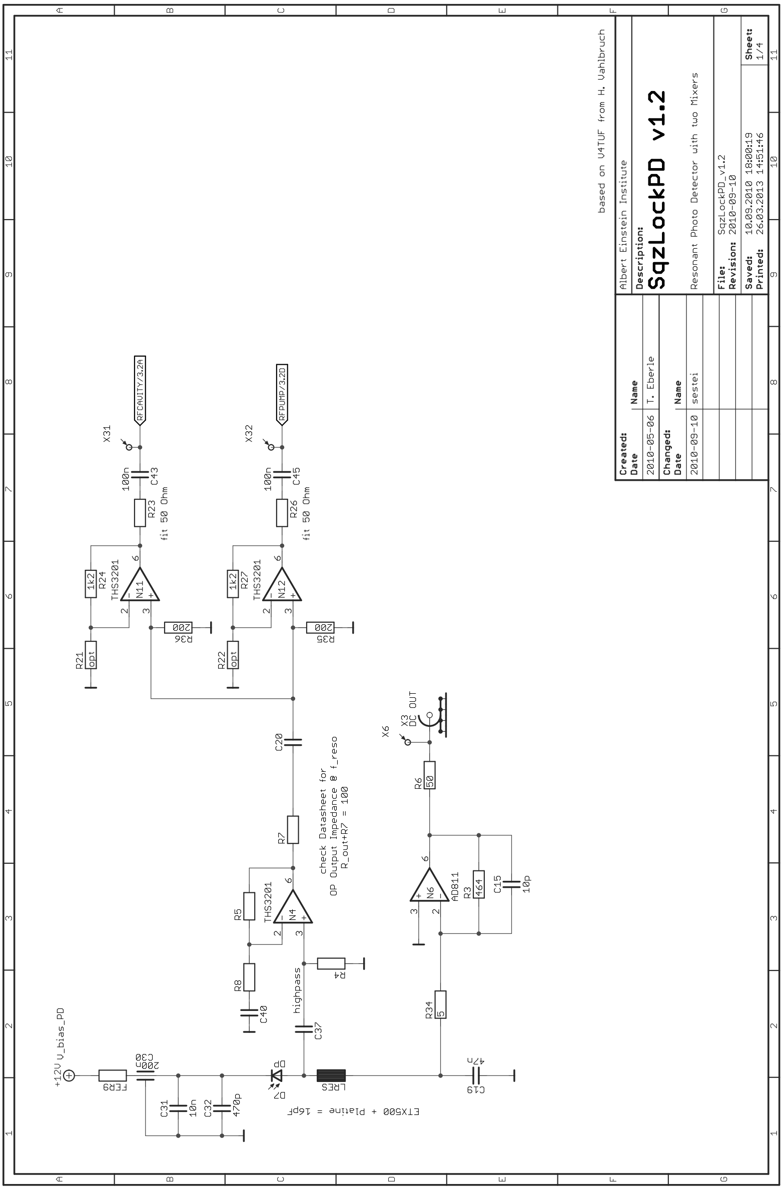
based on V4TUF from H. Vahlbruch
Albert Einstein Institute
Description:
SqzLockPD v1.2
Resonant Photo Detector with two Mixers
File: SqzLockPD_v1.2
Revision: 2010-09-10
Saved: 10.09.2010 18:00:19
Printed: 26.03.2013 14:51:46
Sheet: 1/4
Created:
Date
Name
2010-05-06
T. Eberle
Changed:
Date
Name
2010-09-10
sestei
+12V
V_bias_PD
FER9
C30
200n
C31
10n
C32
470p
D7
DP
LRES
ETX500 + Platine = 16pF
C19
47n
C37
highpass
R4
R8
C40
R5
THS3201
N4
R7
check Datasheet for
OP Output Impedance @ f_reso
R_out+R7 = 100
C20
R34
5
N6
AD811
R3
464
C15
10p
R6
50
X6
X3
DC OUT
R21
opt
R24
1k2
N11
R36
200
R23
fit 50 Ohm
100n
C43
X31
RFCAVITY/3.2A
R22
opt
R27
1k2
N12
R35
200
R26
fit 50 Ohm
100n
C45
X32
RFPUMP/3.2D
A
B
C
D
E
F
G
1
2
3
4
5
6
7
8
9
10
11

Figure A.14: SqzLockPD v1.2 schematic: resonant photo detection

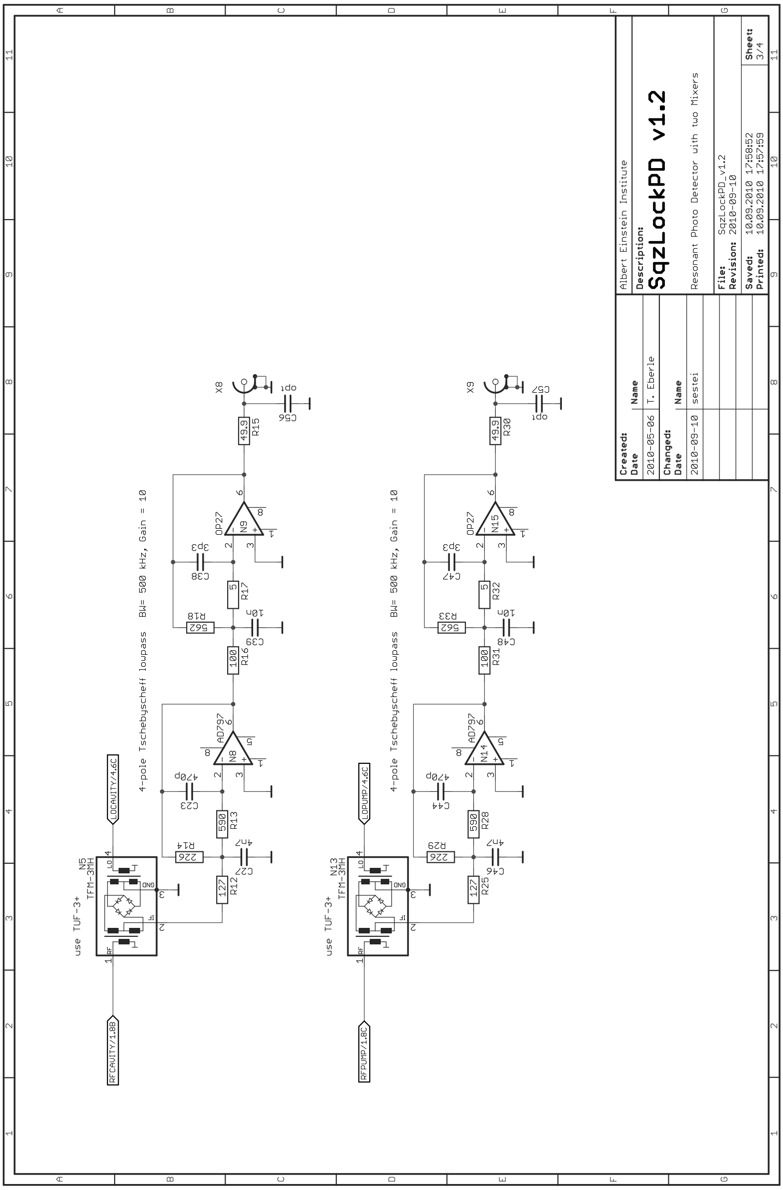
Albert Einstein Institute
Description:
SqzLockPD v1.2
Resonant Photo Detector with two Mixers
File: SqzLockPD_v1.2
Revision: 2010-09-10
Saved: 10.09.2010 17:58:52
Printed: 10.09.2010 17:57:59
Sheet: 3/4
Created: Date 2010-05-06 Name T. Eberle
Changed: Date 2010-09-10 Name sestei
RFCAVITY/1.8B
LOCAVITY/4.6C
use TUF-3+
N5
TFM-3MH
4-pole Tschebyscheff lowpass BW= 500 kHz, Gain = 10
R12 127
R14 226
R13 590
C22 4n7
C23 470p
N8 AD797
R16 100
R18 562
C39 10n
R17 5
C38 3p3
N9 OP27
R15 49.9
C56 10p
X8
RFPUMP/1.8C
LOPUMP/4.6C
use TUF-3+
N13
TFM-3MH
4-pole Tschebyscheff lowpass BW= 500 kHz, Gain = 10
R25 127
R29 226
R28 590
C46 4n7
C44 470p
N14 AD797
R31 100
R33 562
C48 10n
R32 5
C47 3p3
N15 OP27
R30 49.9
C57 10p
X9

Figure A.15: SqzLockPD v1.2 schematic: demodulation path

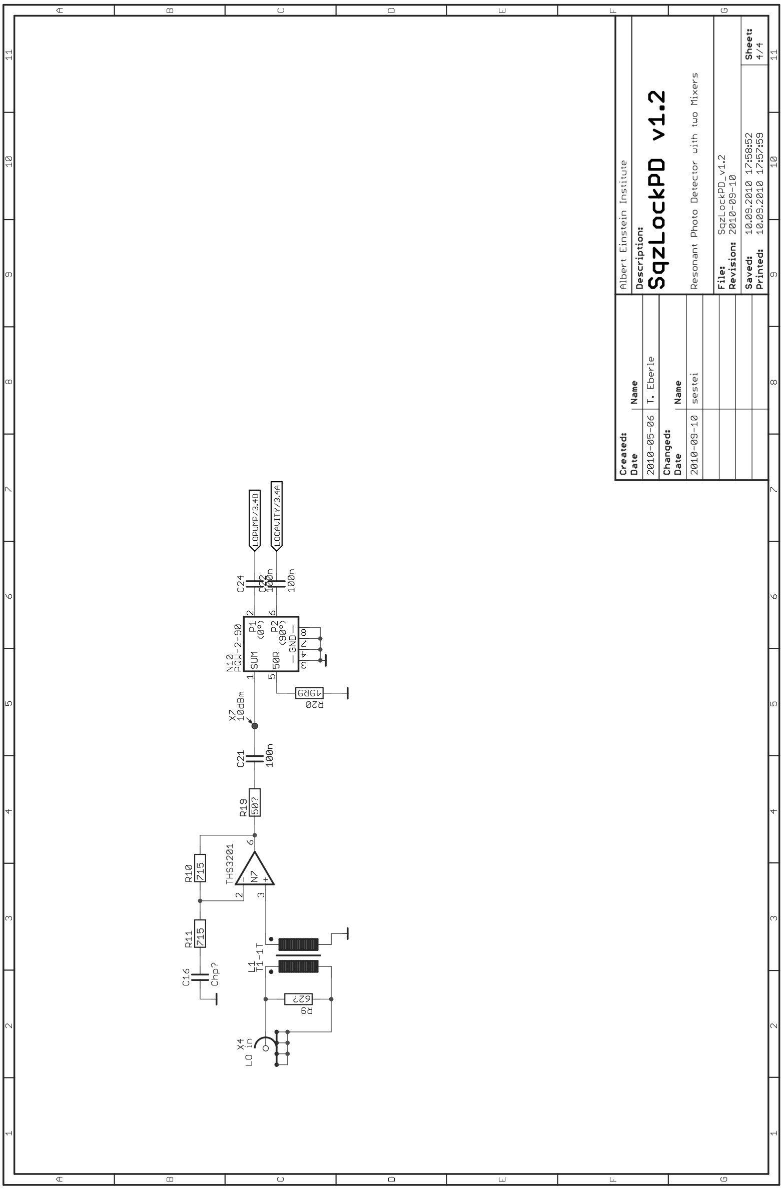
Albert Einstein Institute
Description:
SqzLockPD v1.2
Resonant Photo Detector with two Mixers
File: SqzLockPD_v1.2
Revision: 2010-09-10
Saved: 10.09.2010 17:50:52
Printed: 10.09.2010 17:57:59
Sheet: 4/4
Created:
Date
Name
2010-05-06
T. Eberle
Changed:
Date
Name
2010-09-10
sestei
X4
LO in
R9
62?
L1
T1-1T
C16
Chp?
R11
715
R10
715
THS3201
N7
R19
50?
C21
100n
X7
10dBm
N10
PQW-2-90
SUM
50R
GND
P1 (0°)
P2 (90°)
R20
49R9
C24
100n
C22
100n
OPUMP/3.4D
LOCAVITY/3.4A

Figure A.16: SqzLockPD v1.2 schematic: local oscillator path with 90° power splitter

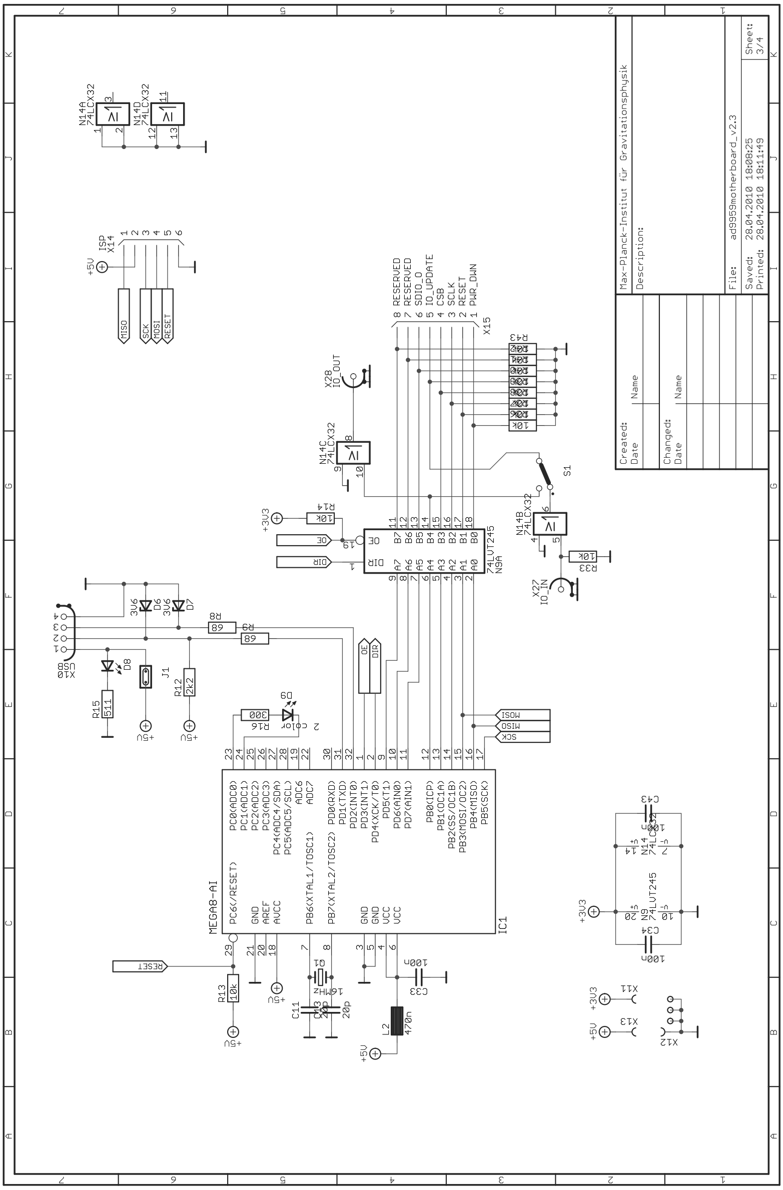
Max-Planck-Institut für Gravitationsphysik
Description:
File: ad9959motherboard_v2.3
Saved: 28.04.2010 18:08:25
Printed: 28.04.2010 18:11:49
Sheet: 3/4
Created: Date Name
Changed: Date Name
MEGA8-AI
IC1
74LVT245
N9A
74LCX32
X15
X10 USB
X14 ISP
X27 IO_IN
X28 IO_OUT
S1
RESERVED
SDIO_0
IO_UPDATE
CSB
SCLK
RESET
PWR_DWN
MISO
MOSI
SCK
OE
DIR
16MHz
470n
+5U
+3U3

Figure A.17: AD9959 4-channel frequency generator: circuit schematic of the USB interface

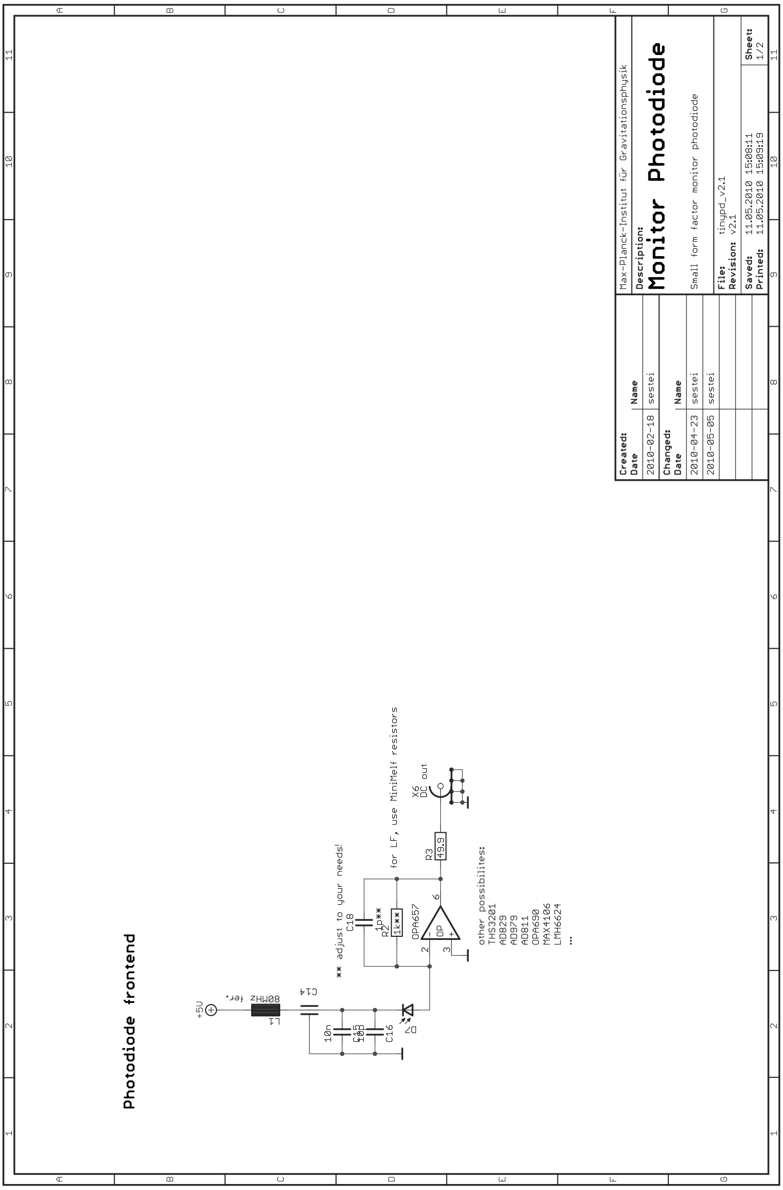
Photodiode frontend
+5V
L1
80MHz fer.
C14
10n
C15
10p
C16
D7
** adjust to your needs!
C18
1p**
R2
1k**
for LF, use MiniMelf resistors
OPA657
OP
2
3
6
R3
49.9
X6
DC out
other possibilites:
THS3201
AD829
AD979
AD811
OPA690
MAX4106
LMH6624
...
Created:
Date
Name
2010-02-18
sestei
Changed:
Date
Name
2010-04-23
sestei
2010-05-05
sestei
Max-Planck-Institut für Gravitationsphysik
Description:
Monitor Photodiode
Small form factor monitor photodiode
File: tinypd_v2.1
Revision: v2.1
Saved: 11.05.2010 15:08:11
Printed: 11.05.2010 15:09:19
Sheet: 1/2
A
B
C
D
E
F
G
1
2
3
4
5
6
7
8
9
10
11

Figure A.18: TinyPD v2.1 monitoring photo-detector: circuit schematics

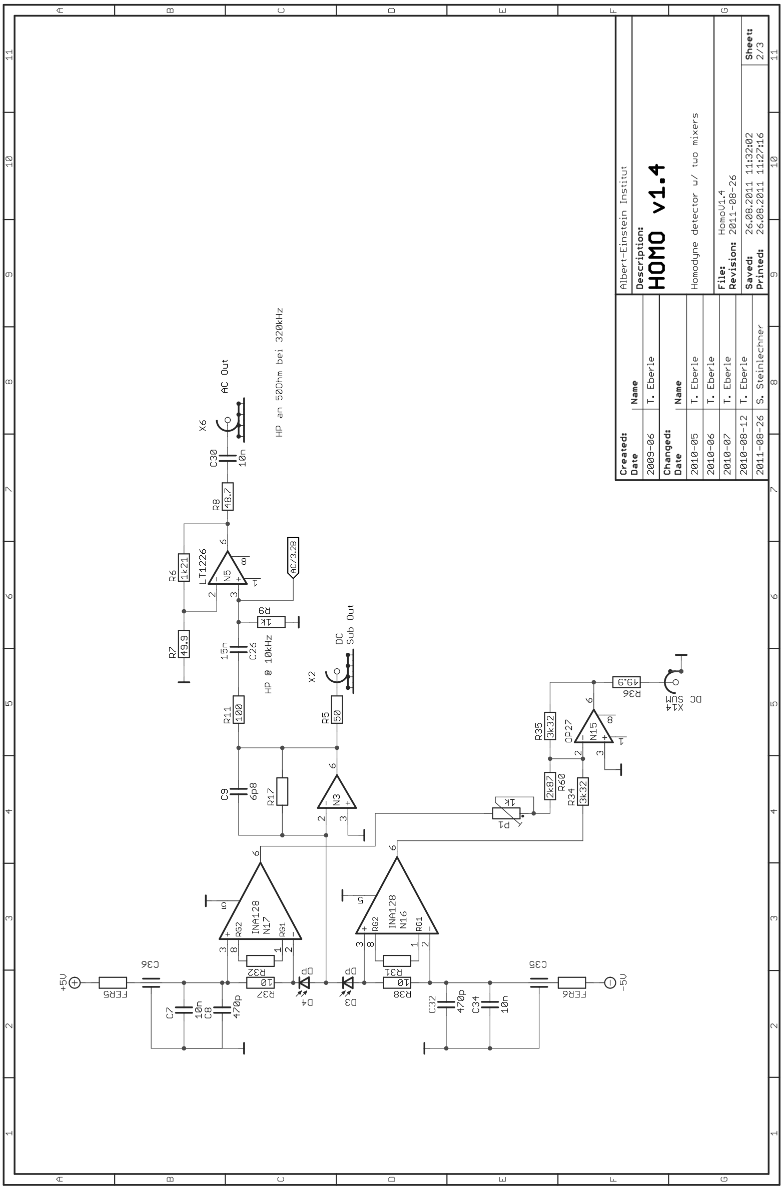
Albert-Einstein Institut
Description:
HOMO v1.4
Homodyne detector w/ two mixers
File: HomoV1.4
Revision: 2011-08-26
Saved: 26.08.2011 11:32:02
Printed: 26.08.2011 11:27:16
Sheet: 2/3
Created: Date Name
2009-06 T. Eberle
Changed: Date Name
2010-05 T. Eberle
2010-06 T. Eberle
2010-07 T. Eberle
2010-08-12 T. Eberle
2011-08-26 S. Steinlechner
INA128
N17
N16
LT1226
N5
N3
OP27
N15
HP an 50Ohm bei 320kHz
HP @ 10kHz
AC Out
DC Sub Out
DC SUM
AC/3.28
X6
X2
X14
+5V
-5V
FER5
FER6
C36
C35
C7 10n
C8 470p
C32 470p
C34 10n
R32
R31
R37 10
R38 10
D4
D3
DP
C9 6p8
R17
R11 100
R5 50
C26 15n
R9 1k
R7 49.9
R6 1k21
R8 48.7
C30 10n
P1 1k
R60 2k87
R34 3k32
R35 3k32
R36 49.9

Figure A.19: HomoV1.4 balanced homodyne detector: detection stage

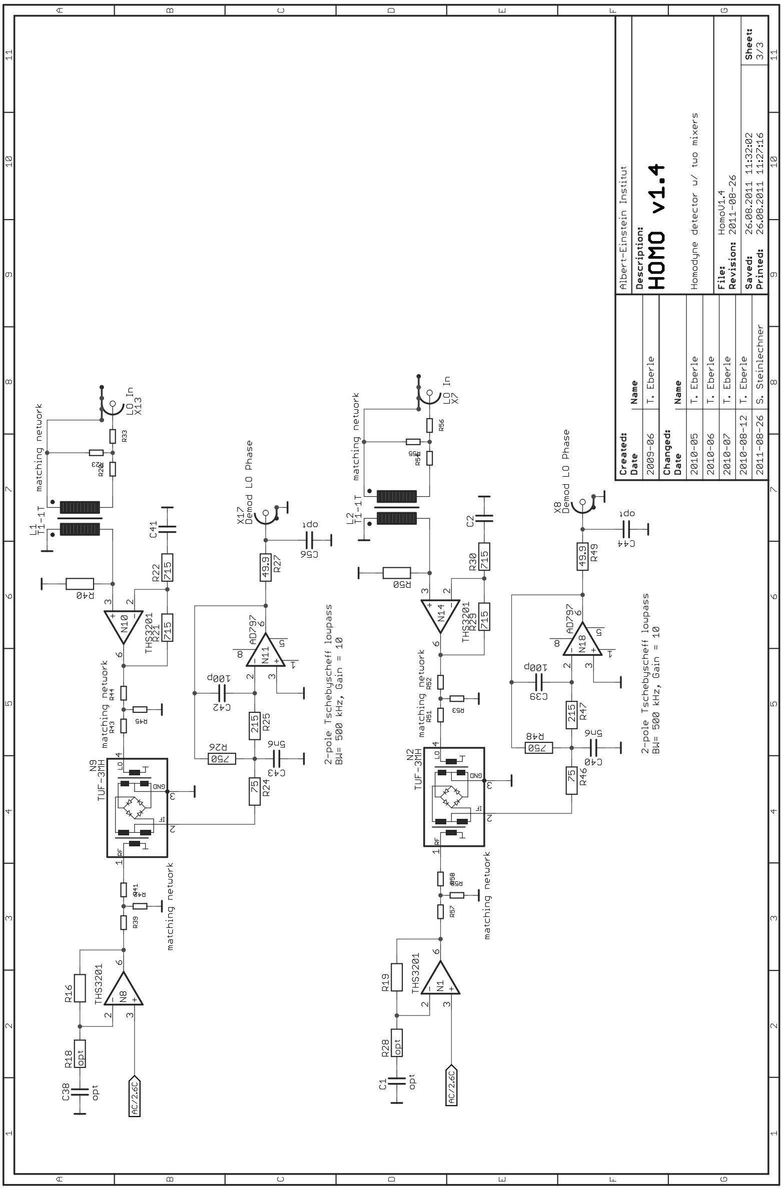
Albert-Einstein Institut
Description:
HOMO v1.4
Homodyne detector u/ two mixers
File: HomoV1.4
Revision: 2011-08-26
Saved: 26.08.2011 11:32:02
Printed: 26.08.2011 11:27:16
Sheet: 3/3
Created: Date Name
2009-06 T. Eberle
Changed: Date Name
2010-05 T. Eberle
2010-06 T. Eberle
2010-07 T. Eberle
2010-08-12 T. Eberle
2011-08-26 S. Steinlechner
LO In
X13
X7
matching network
Demod LO Phase
X17
X8
THS3201
AD797
TUF-3MH
2-pole Tschebyscheff lowpass
BW= 500 kHz, Gain = 10
AC/2.6C

Figure A.20: HomoV1.4 balanced homodyne detector: demodulation stage

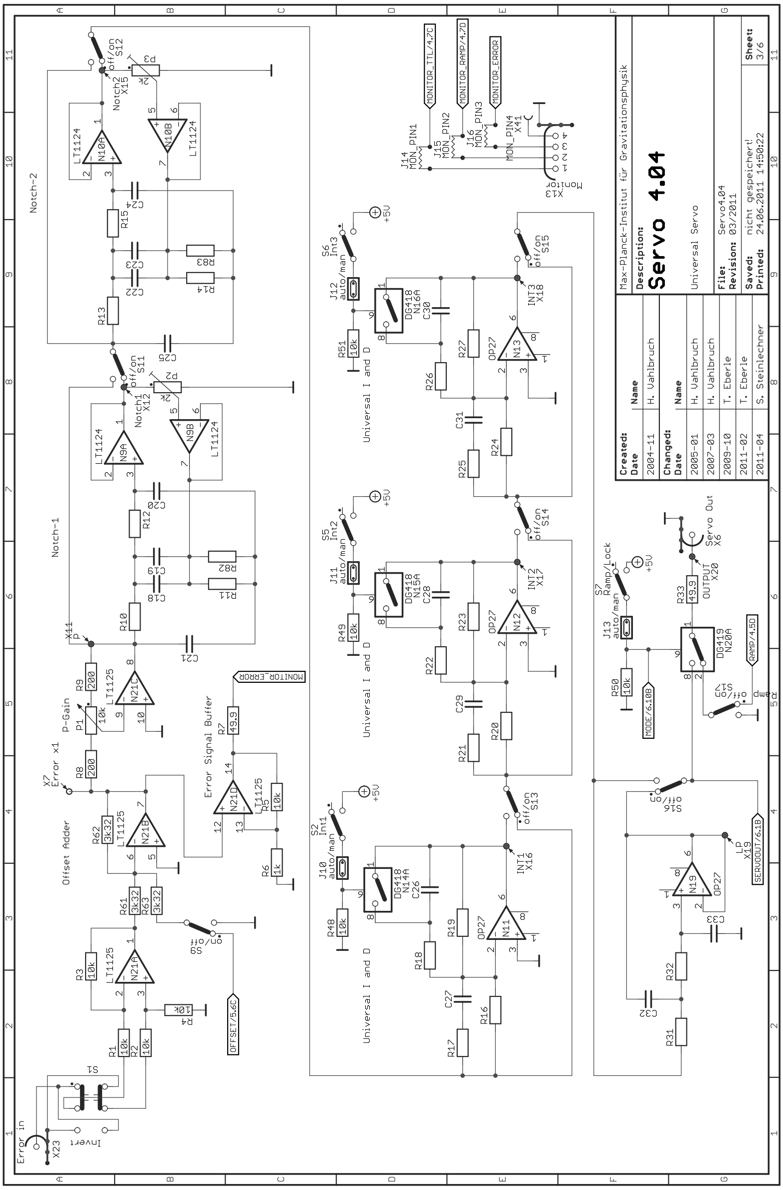
Max-Planck-Institut für Gravitationsphysik
Description:
Servo 4.04
Universal Servo
File: Servo4.04
Revision: 03/2011
Saved: nicht gespeichert!
Printed: 24.06.2011 14:50:22
Sheet: 3/6
Created: Date Name
2004-11 H. Vahlbruch
Changed: Date Name
2005-01 H. Vahlbruch
2007-03 H. Vahlbruch
2009-10 T. Eberle
2011-02 T. Eberle
2011-04 S. Steinlechner
Error in
X23
Invert
S1
Offset Adder
Error x1
X7
P-Gain
P1
Error Signal Buffer
MONITOR_ERROR
OFFSET/5.6C
on/off
S9
Notch-1
Notch-2
Notch1
X12
Notch2
X15
off/on
S11
S12
LT1124
LT1125
Universal I and D
auto/man
Int1
Int2
Int3
INT1
X16
INT2
X17
INT3
X18
DG418
OP27
+5V
MONITOR_TTL/4.2C
MONITOR_RAMP/4.7D
MON_PIN1
MON_PIN2
MON_PIN3
MON_PIN4
Monitor
X13
Ramp/Lock
S7
MODE/6.10B
RAMP/4.5D
DG419
N20A
OUTPUT
X20
Servo Out
X6
LP
X19
SERVOOUT/6.1B

Figure A.21: Servo 4.04/4.05 schematic: transfer function shaping elements

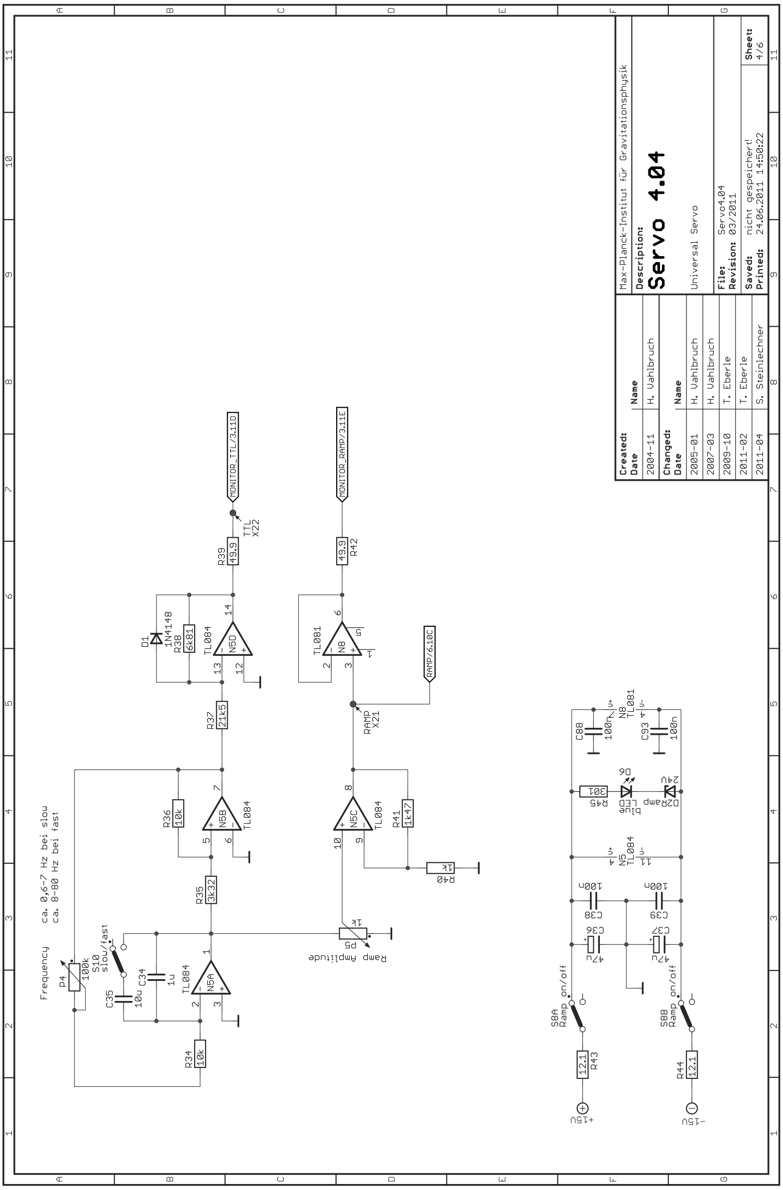
Max-Planck-Institut für Gravitationsphysik
Description:
Servo 4.04
Universal Servo
File: Servo4.04
Revision: 03/2011
Saved: nicht gespeichert!
Printed: 24.06.2011 14:50:22
Sheet: 4/6
Created: Date Name
2004-11 H. Vahlbruch
Changed: Date Name
2005-01 H. Vahlbruch
2007-03 H. Vahlbruch
2009-10 T. Eberle
2011-02 T. Eberle
2011-04 S. Steinlechner
Frequency
P4 100k
S10 slow/fast
ca. 0,6-7 Hz bei slow
ca. 8-80 Hz bei fast
C35 10u
C34 1u
R34 10k
N5A TL084
R35 3k32
R36 10k
N5B TL084
R37 21k5
D1 1N4148
R38 6k81
N5D TL084
R39 49.9
TTL X22
MONITOR_TTL/3.11D
P5 1k Ramp Amplitude
N5C TL084
R41 1k47
R40 1k
RAMP X21
RAMP/6.10C
N8 TL081
R42 49.9
MONITOR_RAMP/3.11E
S8A Ramp on/off
S8B Ramp on/off
R43 12.1
R44 12.1
+15V
-15V
C36 47u
C37 47u
C38 100n
C39 100n
N5 TL084
R45 301
D6 blue LED
D2 Ramp 24V
C88 100n
C93 100n
N8 TL081

Figure A.22: Servo 4.04/4.05 schematic: ramp generator section

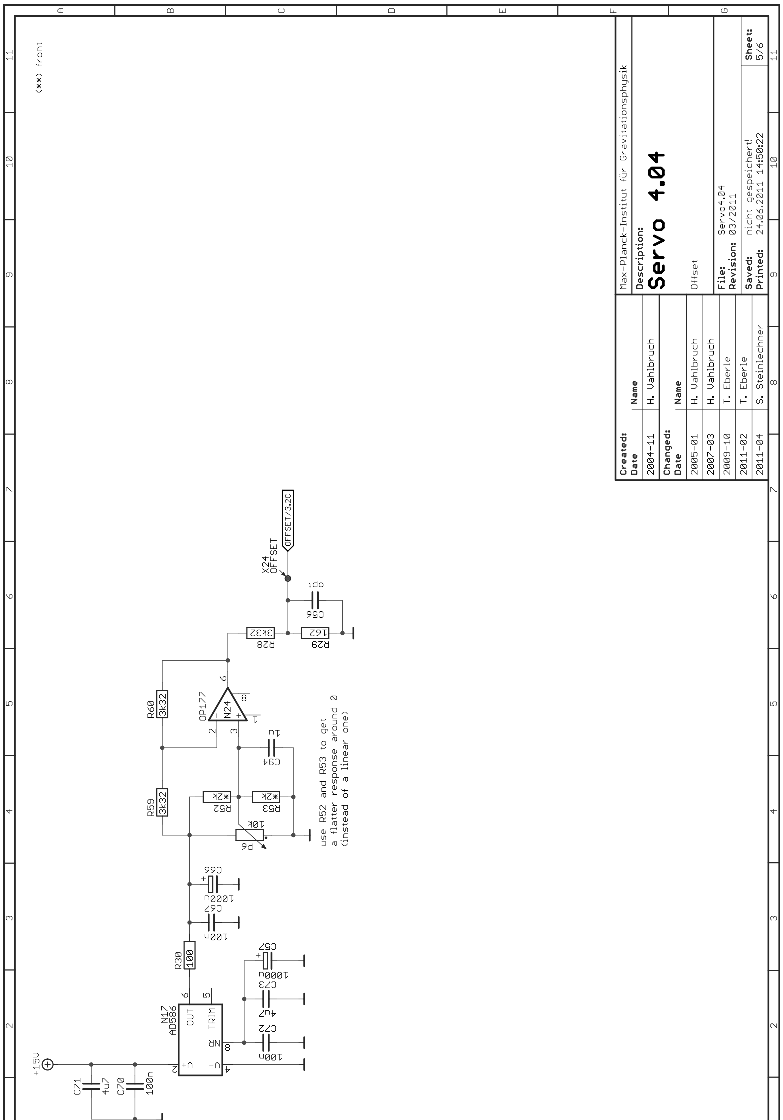
(**) front
+15V
C71
4u7
C70
100n
N17
AD586
OUT
TRIM
NR
R30
100
C57
1000u
C73
4u7
C72
100n
C67
100n
C66
1000u
R59
3k32
R60
3k32
P6
10k
R52
*2k
R53
*2k
C94
1u
OP177
N24
R28
3k32
R29
162
C56
10p
X24
OFFSET
OFFSET/3.2C
use R52 and R53 to get
a flatter response around 0
(instead of a linear one)
Created:
Date
Name
2004-11
H. Vahlbruch
Changed:
2005-01
H. Vahlbruch
2007-03
H. Vahlbruch
2009-10
T. Eberle
2011-02
T. Eberle
2011-04
S. Steinlechner
Max-Planck-Institut für Gravitationsphysik
Description:
Servo 4.04
Offset
File:
Servo4.04
Revision:
03/2011
Saved:
nicht gespeichert!
Printed:
24.06.2011 14:50:22
Sheet:
5/6

Figure A.23: Servo 4.04/4.05 schematic: offset voltage generation

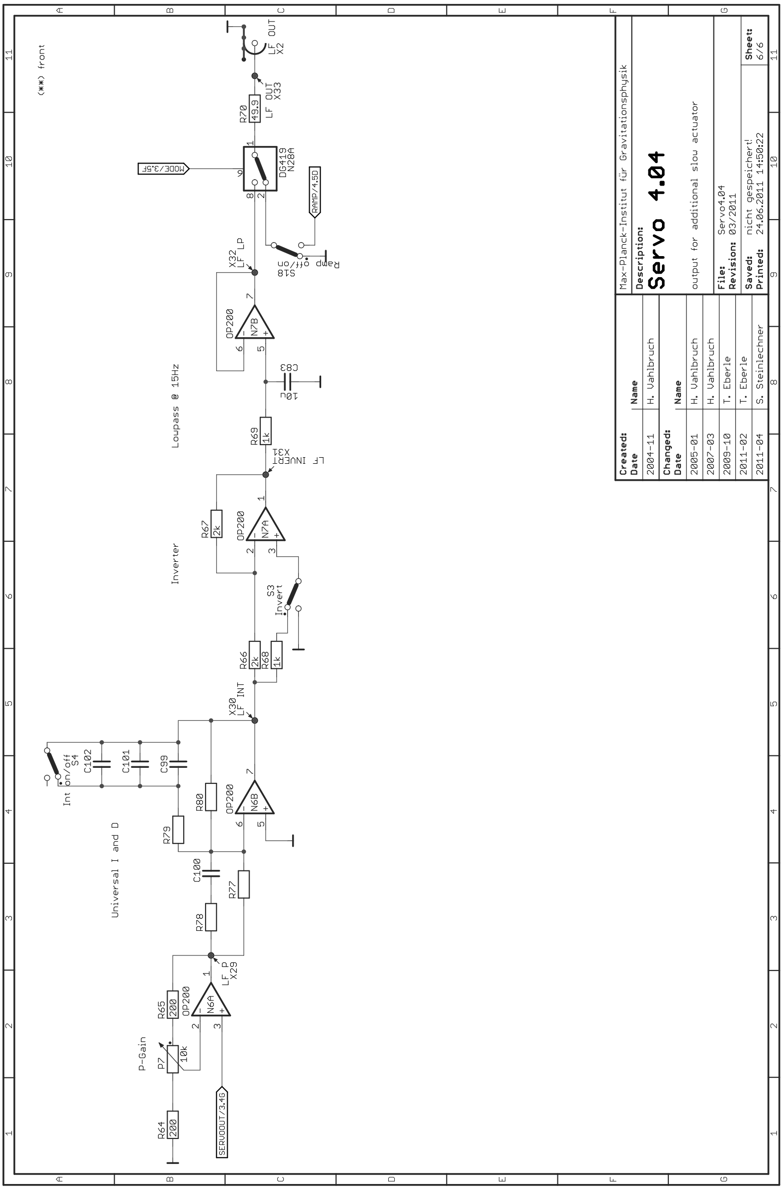
(**) front
R64
200
P7
10k
P-Gain
R65
200
OP200
N6A
LF P
X29
SERVOOUT/3.4G
Universal I and D
R78
C100
R77
R79
R80
OP200
N6B
C99
C101
C102
S4
Int on/off
X30
LF INT
R66
2k
R68
1k
S3
Invert
Inverter
R67
2k
OP200
N7A
X31
LF INVERT
R69
1k
Lowpass @ 15Hz
C83
10u
OP200
N7B
X32
LF LP
S18
Ramp off/on
RAMP/4.5D
DG419
N28A
MODE/3.5F
R70
49,9
LF OUT
X33
LF OUT
X2
Max-Planck-Institut für Gravitationsphysik
Description:
Servo 4.04
output for additional slow actuator
File: Servo4.04
Revision: 03/2011
Saved: nicht gespeichert!
Printed: 24.06.2011 14:50:22
Sheet: 6/6
Created:
Date
Name
2004-11
H. Vahlbruch
Changed:
Date
Name
2005-01
H. Vahlbruch
2007-03
H. Vahlbruch
2009-10
T. Eberle
2011-02
T. Eberle
2011-04
S. Steinlechner

Figure A.24: Servo 4.04/4.05 schematic: low frequency stage

▸ A.4 *Software*

During my stay at the AEI, I have developed several pieces of software. While they are not directly connected to this thesis, the following list shall serve as an inventory such that anyone who is interested in the software can find and use it.

▸ A.4.1 *TkSim*

`tksim` is a numerical simulation and analysis program for measuring absorption with the photo-thermal self-phase modulation effect [LSS+10]. The simulation itself has been written by Nico Lastzka [Las10], while the experimental work has been performed by Jessica Steinlechner [Ste13]. I have written several PYTHON scripts around the simulation to allow a semi-automatic analysis of the experimental results. The complete `tksim` software package can be found in the AEI's `git` repository at `https://gitmaster.atlas.aei.uni-hannover.de/tksim`.

tksim_gui

This script provides a *graphical user interface* (GUI) for processing the raw measurement data. It reads several oscilloscope file formats:

- Tektronix CSV (comma separated, columns *TIME*, *CH1*, *CH2*, ...)
- Agilent binary (if the first two bytes are `AG`)
- LeCroy WaveJet314 CSV *and* binary

Each measurement channel can be assigned to one of *Reflection*, *Transmission*, *PDH Error Signal* (optional), *Ramp*. The script then tries to automatically find a full ramp and extract an Airy peak on each ramp side. Optionally it looks for sidebands in the PDH error signal, from which it estimates NFSR parameters for each scan direction.

The script produces an output data file containing the peaks for both scan directions, using the format that `tksim` expects. The filename is automatically constructed in the format `{X}mW_{Y}Hz.dat`, where `{X}` is replaced by the laser power in milliwatts, and `{Y}` is replaced by the scan frequency. It optionally creates `.ini` and `.par` files, based on values from template files.

Opened measurement data files can be exported to a tab separated ASCII file. This makes it possible to easily convert the oscilloscope files to a format that is understandable by **gnuplot** and the like.

tksim_nm

This script finds the global optimum of parameters that minimizes the variance between simulated and experimental data.

It uses the Nelder-Mead algorithm for finding the minimum. For optimization with N parameters, a simplex with $N+1$ vertices is created (e.g. a tetrahedron for $N=3$). The variance at all vertices is evaluated. Then a certain set of rules is applied which fold, expand and shrink the simplex until at the end of the day it contracts around the point of minimum variance.

▸ A.4.2 *AD9959*

The USB controlled, 4-channel function generator AD9959 described in Sec. A.3.3 is accompanied by firmware for the micro controller (µC) and a GUI software for setting the values from a PC. The firmware is written in C and needs to be compiled using the **avr-gcc** compiler suite, which is available for all relevant operating systems. To write the firmware onto the Atmel µC, I used an USB programmer built after the design from Thomas Fischl, `http://www.fischl.de/usbasp/`, together with the **avrdude** programming software. A cross-platform software written in C++ allows to control the output of all four channels with an easy to use graphical user interface. The software was extended and rewritten by Tobias Eberle in Python to be able to address multiple function generators at the same time. The complete source code can be found in the AEI's `git` repository at `https://gitmaster.atlas.aei.uni-hannover.de/ad9959`.

▸ A.4.3 *lab*

I contributed a few minor functions to the `lab` analysis package written and maintained by Tobias Eberle. It is a Python framework for numerical calculations with covariance matrices, as well as an analysis tool for experimental entanglement and squeezing data. The software package can be obtained as a `mercurial` repository in the folder `crypticefos/software/python/lab` on the group's file server.

▸ A.4.4 *Entangled readout simulation*

For the simulation of a gravitational wave detector with detuned signal recycling and entangled light readout, I wrote a Python script which calculates the quantum noise and the resulting noise spectral density. It is based on earlier, but largely unpublished Matlab files by Jan Harms and Helge Müller-Ebhardt. The auxiliary modules `ifo` and `geo600` contain the transfer functions for the interferometer itself. These modules are not reproduced here, but have been integrated in the `lab` package.

```
#!/usr/bin/python
# Signal-recycled Michelson interferometer

from pylab import *
import geo600
import ifo
from scipy.linalg import block_diag

def blkdiag(*args):
    return matrix(block_diag(*args))

def R(theta):
    return matrix([[cos(theta), sin(theta)],
                   [-sin(theta), cos(theta)]])

def BS():
    return 1/sqrt(2) * matrix([[1,  0,  1,  0],
                               [0,  1,  0,  1],
                               [1,  0, -1,  0],
                               [0,  1,  0, -1]])

def detect(O, port, angle):
    d = zeros((O.shape[0],1))
    d[port*2] = cos(angle)
    d[port*2+1] = sin(angle)
    OOT = ifo.symProduct(O)
    return real(d.T * OOT * d)

if __name__ == "__main__":
    geo = geo600.GEO600(m=100000)
    # simulation parameters
    fstart = 1
    fend = 3
    Npoints = 1000

    x = logspace(fstart, fend, Npoints)

    Omega = 2*pi*x

    figure(1)

    geo.setDetectionAngle(0)
    class_noise_x = geo.noiseTransfer(Omega)
    geo.setDarkportInput(ifo.squeeze_db(-10,pi/2))
    signal_transfer_x = geo.signalTransfer(Omega)
    squeeze_x_noise_x = geo.signalTransfer(Omega)

    geo.setDetectionAngle(pi/2)
    geo.setDarkportInput(ifo.squeeze_db(-10,pi/2))
    signal_transfer_p = geo.signalTransfer(Omega)
    squeeze_x_noise_p = geo.noiseTransfer(Omega)

    # classical sensitivity, x quadrature
    loglog(x, sqrt(class_noise_x / signal_transfer_x))
    hold(’on’)
    # classical sensitivity, p quadrature
    # class. noise is the same for p and x anyway
    loglog(x, sqrt(class_noise_x / signal_transfer_p))
    # squeezed sensitivity, squeezing at SR resonance, detection in X and P
    loglog(x, sqrt(squeeze_x_noise_x / signal_transfer_x))
    loglog(x, sqrt(squeeze_x_noise_p / signal_transfer_p))

    # entanglement: signal is unaffected except for division at output
        beam-splitter
    # east output: p
    # south output: x
    signal_transfer_x *= 0.5
    signal_transfer_p *= 0.5

    # detection and recombination angles/phases
    angle_east = -0.11
    angle_south = angle_east + pi/2
    angle_recombine = 2.03

    Sin = blkdiag(ifo.squeeze_db(-10,angle_south), ifo.squeeze_db(-10,
        angle_east))
    BSent = BS()
    BSout = BS()
    Rout = R(angle_recombine) * exp(-1j*angle_recombine)
    ent_noise_east = zeros_like(Omega)
    ent_noise_south = zeros_like(Omega)
    ent_signal_east = zeros_like(Omega)
    ent_signal_south = zeros_like(Omega)
    for ii in range(Npoints):
        T = geo.T(Omega[ii]) # noise transfer function
        S = geo.S(Omega[ii]) # signal transfer function
        S /= sqrt(2)         # signal is divided into two ports
        O = BSout * blkdiag(T, Rout) * BSent * Sin # entangled readout
        ent_noise_east[ii] = abs(detect(O, 0, angle_east)[0,0])   # the
             [0,0] converts
        ent_noise_south[ii] = abs(detect(O, 1, angle_south)[0,0]) # the
             matrix to a float
        ent_signal_east[ii] = abs(detect(S, 0, angle_east)[0,0])
        ent_signal_south[ii] = abs(detect(S, 0, angle_south)[0,0])

    # calculate SNR at both detectors and coherent sum
    snr_east = sqrt(ent_noise_east / ent_signal_east)
    snr_south = sqrt(ent_noise_south / ent_signal_south)
    sum_noise = sqrt(ent_noise_east + ent_noise_south) / (sqrt(
        signal_transfer_p) + sqrt(signal_transfer_x))
    loglog(x, snr_east)
    loglog(x, snr_south)
    loglog(x, sum_noise)

    legend(['class X', 'class P', 'sqz X', 'sqz P', 'ent E', 'ent S', '
        sumnoise'], loc='lower left')
    xlabel('Frequency (Hz)')
    ylabel('Linear noise spectral density ($1/\sqrt{\\rm Hz}$)')
    hold('off')
    xlim(50,500)
    ylim(1e-23,1e-21)
    xticks((50, 100, 200, 500),(50,100,200,500))

    show()
```

References

[Bur10] O. Burmeister. "Optical properties of 3-port-grating coupled cavities". PhD thesis. Leibniz Universität Hannover, 2010. URN: `urn:nbn:de:gbv:089-6179299719`.

[Del13] F. Dellsperger. *Smith V3.10*. 2013. URL: `http://www.fritz.dellsperger.net/`.

[Las10] N. Lastzka. "Numerical modelling of classical and quantum effects in non-linear optical systems". PhD thesis. Leibniz Universität Hannover, 2010. URN: `urn:nbn:de:gbv:089-6433683534`.

[LSS$^+$10] N. Lastzka, J. Steinlechner, S. Steinlechner, and R. Schnabel. "Measuring small absorptions by exploiting photothermal self-phase modulation". *Applied Optics* 49 (2010), 5391. DOI: `10.1364/AO.49.005391`.

[Ser13] B. Sernelius. *Lecture notes: TFYY67, Electrodynamics*. 2013. URL: `http://www.ifm.liu.se/courses/TFYY67/`.

[Ste13] J. Steinlechner. "Optical absorption measurements for third generation gravitational wave detectors". PhD thesis. Leibniz Universität Hannover, 2013.

Acknowledgements

This thesis would not have been possible without the support of many people whom I would like to thank here.

First and foremost, I would like to thank my supervisor, Prof. Roman Schnabel, for providing me with the opportunity to work on such a fascinating topic in a nice and friendly atmosphere.

I am thankful to Prof. Karsten Danzmann for making the Albert Einstein institute a wonderful place for fruitful scientific work and discussions.

None of the experiments could have been performed without the expertise of our mechanics and electronics workshops. Thus I would like to thank all the workshop guys, especially Andreas Weidner and Philipp Schauzu, for their comments and their beautiful work, and I would like to take this opportunity to apologize for all the horrible drawings and schematics I sent them.

Melanie and Jöran have been my fellow co-workers at the optical table, where they contributed a lot to the experiments in my thesis and to the lab's atmosphere.

Many experimental challenges were solved in discussions with Aiko, Hank, Moritz, and Tobias. Valuable comments and corrections to this thesis have been provided by Christina, Jessica, Melanie, Moritz, Roman, Sascha, Tobias and Vitus – thank you very much!

Last but not least, I would like to thank my beloved family, Jessica, Jan and Ben, for reminding me of the important things in life.

Curriculum vitae

▸ *Personal details*

Sebastian Stephan Steinlechner

Schaufelder Str. 27
30167 Hannover
Germany

born August 11th, 1983
in Marburg/Lahn, Germany

▸ *Education*

since 05/2010	PhD student, Leibniz Unversität Hannover
11/2008 – 05/2010	PhD student, stipend “IMPRS on Gravitational Wave Astronomy”
10/2003 – 10/2008	Physics studies, Leibniz Universität Hannover, Diploma
1996 – 2003	Gymnasium Sarstedt, Abitur
1994 – 1996	Orientierungsstufe, Sarstedt
1993 – 1994	Grundschule II, Sarstedt
1990 – 1993	Grundschule Frohnhausen

Publications

▸ 2013

1. **S. Steinlechner**, J. Bauchrowitz, M. Meinders, H. Müller-Ebhardt, K. Danzmann, R. Schnabel:
   Quantum-Dense Metrology
   Nature Photonics, accepted
2. J. Steinlechner, C. Krüger, N. Lastzka, **S. Steinlechner**, A. Khalaidovski, R. Schnabel:
   Optical absorption measurements on crystalline silicon test masses at 1550 nm
   Classical and Quantum Gravity **30**, 095007
3. **S. Steinlechner**, J. Bauchrowitz, T. Eberle, R. Schnabel:
   Strong Einstein-Podolsky-Rosen steering with unconditional entangled states
   Physical Review A **87**, 022104
4. J. Aasi, J. Abadie, . . . , **S. Steinlechner**, . . . , J. Zweizig:
   Search for gravitational waves from binary black hole inspiral, merger, and ringdown in LIGO-Virgo data from 2009–2010
   Physical Review D **87**, 022002
5. J. Aasi, J. Abadie, . . . , **S. Steinlechner**, . . . , D. P. Anderson:
   Einstein@Home all-sky search for periodic gravitational waves in LIGO S5 data
   Physical Review D **87**, 042001
6. J. Aasi, J. Abadie, . . . , **S. Steinlechner**, . . . , J. Zweizig:
   Prospects for Localization of Gravitational Wave Transients by the Advanced LIGO and Advanced Virgo Observatories
   arXiv:1304.0670 [gr-qc]

▸ 2012

7. J. Abadie, BP. Abbott, . . . , **S. Steinlechner**, . . . , J. Zweizig:
   Search for gravitational waves from low mass compact binary coalescence in LIGO's sixth science run and Virgo's science runs 2 and 3
   Physical Review D **85**, 082002
8. J. Abadie, BP. Abbott, . . . , **S. Steinlechner**, . . . , J. Zweizig:

All-sky search for periodic gravitational waves in the full S5 LIGO data
Physical Review D **85**, 022001

9. J. Abadie, BP. Abbott, . . . , **S. Steinlechner**, . . . , J. Zweizig:
   Implementation and testing of the first prompt search for gravitational wave transients with electromagnetic counterparts
   Astronomy & Astrophysics **539**, A124
10. V. Händchen, T. Eberle, **S. Steinlechner**, A. Samblowski, T. Franz, R. Werner, R. Schnabel:
    Observation of one-way Einstein-Podolsky-Rosen steering
    Nature Photonics **6**, 598-601
11. J. Abadie, BP. Abbott, . . . , **S. Steinlechner**, . . . , J. Zweizig:
    First low-latency LIGO+ Virgo search for binary inspirals and their electromagnetic counterparts
    Astronomy & Astrophysics **541**, A155
12. J. Abadie, BP. Abbott, . . . , **S. Steinlechner**, . . . , J. Zweizig:
    Upper limits on a stochastic gravitational-wave background using LIGO and Virgo interferometers at 600–1000 Hz
    Physical Review D **85**, 122001
13. J. Abadie, BP. Abbott, . . . , **S. Steinlechner**, . . . , J. Zweizig:
    All-sky search for gravitational-wave bursts in the second joint LIGO-Virgo run
    Physical Review D **85**, 122007
14. J. Abadie, BP. Abbott, . . . , **S. Steinlechner**, . . . , X.-L. Zhang:
    Search for gravitational waves associated with gamma-ray bursts during LIGO science run 6 and Virgo science runs 2 and 3
    The Astrophysical Journal **760**, 12
15. J. Abadie, BP. Abbott, . . . , **S. Steinlechner**, . . . , J. Zweizig:
    Search for gravitational waves from intermediate mass binary black holes
    Physical Review D **85**, 102004
16. J. Aasi, J. Abadie, . . . , **S. Steinlechner**, . . . , J. Zweizig:
    The characterization of Virgo data and its impact on gravitational-wave searches
    Classical and Quantum Gravity **29**, 155002
17. J. Steinlechner, L. Jensen, C. Krüger, N. Lastzka, **S. Steinlechner**, R. Schnabel:
    Photothermal self-phase-modulation technique for absorption measurements on high-reflective coatings
    Applied optics **51**, 1156-1161
18. J. Abadie, BP. Abbott, . . . , **S. Steinlechner**, . . . , M. Was:
    Implications for the Origin of GRB 051103 from LIGO Observations
    The Astrophysical Journal **755**, 2

19. S. Ast, A. Samblowski, M. Mehmet, **S. Steinlechner**, T. Eberle, R. Schnabel:
    Continuous-wave nonclassical light with gigahertz squeezing bandwidth
    Optics Letters **37**, 2367-2369
20. PA. Evans, JK. Fridriksson, . . . , **S. Steinlechner**, . . . , J. Zweizig:
    Swift follow-up observations of candidate gravitational-wave transient events
    The Astrophysical Journal Supplement Series **203**, 28

▸ 2011

21. J. Abadie, BP. Abbott, . . . , **S. Steinlechner**, . . . , J. Zweizig:
    A gravitational wave observatory operating beyond the quantum shot-noise limit
    Nature Physics **7**, 962-965
22. J. Abadie, BP. Abbott, . . . , **S. Steinlechner**, . . . , J. Zweizig:
    Search for gravitational waves from binary black hole inspiral, merger, and ringdown
    Physical Review D **83**, 122005
23. J. Abadie, BP. Abbott, . . . , **S. Steinlechner**, . . . , K. Yamaoka:
    Search for gravitational wave bursts from six magnetars
    The Astrophysical Journal Letters **734**, L35
24. J. Abadie, BP. Abbott, . . . , **S. Steinlechner**, . . . , J. Palfreyman:
    Beating the spin-down limit on gravitational wave emission from the Vela pulsar
    The Astrophysical Journal **737**, 93
25. M. Mehmet, S. Ast, T. Eberle, **S. Steinlechner**, H. Vahlbruch, R. Schnabel:
    Squeezed light at 1550 nm with a quantum noise reduction of 12.3 dB
    Optics Express **19**, 25763-25772
26. S. Ast, R. Nia, A. Schönbeck, N. Lastzka, J. Steinlechner, T. Eberle, M. Mehmet, **S. Steinlechner**, R. Schnabel:
    High-efficiency frequency doubling of continuous-wave laser light
    Optics letters **36**, 3467-3469
27. J. Abadie, BP. Abbott, . . . , **S. Steinlechner**, . . . , J. Zweizig:
    Directional limits on persistent gravitational waves using LIGO S5 science data
    Physical Review Letters **107**, 271102

▸ 2010

28. J. Abadie, BP. Abbott, . . . , **S. Steinlechner**, . . . , K. Belczynski:
    Predictions for the rates of compact binary coalescences observable by ground-based gravitational-wave detectors
    Classical and Quantum Gravity **27**, 173001
29. J. Abadie, BP. Abbott, . . . , **S. Steinlechner**, . . . , J. Zweizig:
    Search for gravitational waves from compact binary coalescence in LIGO and Virgo data from S5 and VSR1
    Physical Review D **82**, 102001

30. J. Abadie, BP. Abbott, . . . , **S. Steinlechner**, . . . , J. Zweizig:
    Calibration of the LIGO gravitational wave detectors in the fifth science run
    Nuclear Instruments and Methods in Physics Research Section A: Accelerators, Spectrometers, Detectors and Associated Equipment **624**, 223-240
31. T. Eberle, **S. Steinlechner**, J. Bauchrowitz, V. Händchen, H. Vahlbruch, M. Mehmet, H. Müller-Ebhardt, R. Schnabel:
    Quantum enhancement of the zero-area Sagnac interferometer topology for gravitational wave detection
    Physical Review Letters **104**, 251102
32. J. Abadie, BP. Abbott, . . . , **S. Steinlechner**, . . . , J. Zweizig:
    First search for gravitational waves from the youngest known neutron star
    The Astrophysical Journal **722**, 1504
33. M. Mehmet, T. Eberle, **S. Steinlechner**, H. Vahlbruch, R. Schnabel:
    Demonstration of a quantum-enhanced fiber Sagnac interferometer
    Optics Letters **35**, 1665-1667
34. R. Schnabel, M. Britzger, F. Brückner, O. Burmeister, K. Danzmann, J. Dück, T. Eberle, D. Friedrich, H. Lück, M. Mehmet, R. Nawrodt, **S. Steinlechner**, B. Willke:
    Building blocks for future detectors: Silicon test masses and 1550 nm laser light
    Journal of Physics: Conference Series **228**, 012029
35. N. Lastzka, J. Steinlechner, **S. Steinlechner**, R. Schnabel:
    Measuring small absorptions by exploiting photothermal self-phase modulation
    Applied Optics **49**, 5391-5398

▸ 2009

36. M. Mehmet, **S. Steinlechner**, T. Eberle, H. Vahlbruch, A. Thüring, K. Danzmann, R. Schnabel:
    Observation of cw squeezed light at 1550 nm
    Optics Letters **34**, 1060-1062

▸ 2008

37. **S. Steinlechner**, S. Barke, J. Dück, L. Hoppe, R. Lorbeer, M. Otto, A. Samblowski, T. Westphal:
    Der Lifter – Ein Flugobjekt mit Ionenantrieb
    PhyDid A – Physik und Didaktik in Schule und Hochschule **2**, 20-26
38. **S. Steinlechner**:
    Gequetschtes Licht bei 1550 nm
    Diplomarbeit